# Rough-Terrain Mobile Robot Planning and Control with Application to Planetary Exploration

by

**Karl David Iagnemma**

Bachelor of Science in Mechanical Engineering
University of Michigan, 1994

Master of Science in Mechanical Engineering
Massachusetts Institute of Technology, 1997

Submitted to the Department of Mechanical Engineering in Partial Fulfillment of the
Requirements for the Degree of

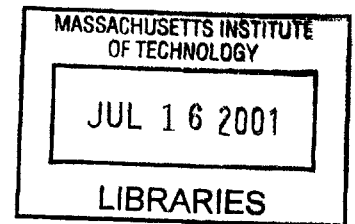**Doctor of Philosophy in Mechanical Engineering**

at the

**Massachusetts Institute of Technology**

February 2001

©2001 Karl David Iagnemma
All rights reserved

The author hereby grants to MIT permission to reproduce and to distribute publicly paper
and electronic copies of this thesis document in whole or in part.

Signature of Author: _____

Department of Mechanical Engineering
December 5, 2000

Certified by: _____

Steven Dubowsky
Professor of Mechanical Engineering
Thesis Supervisor

Accepted by: _____

Ain A. Sonin
Professor of Mechanical Engineering
Chairman, Departmental Graduate Committee

# Rough-Terrain Mobile Robot Planning and Control with Application to Planetary Exploration

by

Karl David Iagnemma

Submitted to the Department of Mechanical Engineering
on December 5, 2000, in partial fulfillment of the requirements for the degree of
Doctor of Philosophy in Mechanical Engineering

## Abstract

Future planetary exploration missions will require mobile robots to perform difficult tasks in highly challenging terrain, with limited human supervision. Current motion planning and control algorithms are not well suited to rough-terrain mobility, since they generally do not consider the physical characteristics of the rover and its environment. Failure to understand these characteristics could lead to rover entrapment and mission failure. In this thesis, methods are presented for improved rough-terrain mobile robot mobility, which exploit fundamental physical models of the rover and terrain.

Wheel-terrain interaction has been shown to be critical to rough terrain mobility. A wheel-terrain interaction model is presented, and a method for on-line estimation of important model parameters is proposed. The local terrain profile also strongly influences robot mobility. A method for on-line estimation of wheel-terrain contact angles is presented. Simulation and experimental results show that wheel-terrain model parameters and contact angles can be estimated on-line with good accuracy.

Two rough-terrain planning algorithms are introduced. First, a motion planning algorithm is presented that is computationally efficient and considers uncertainty in rover sensing and localization. Next, an algorithm for geometrically reconfiguring the rover kinematic structure to optimize tipover stability margin is presented. Both methods utilize models developed earlier in the thesis. Simulation and experimental results on the Jet Propulsion Laboratory Sample Return Rover show that the algorithms allow highly stable, semi-autonomous mobility in rough terrain.

Finally, a rough-terrain control algorithm is presented that exploits the actuator redundancy found in multi-wheeled mobile robots to improve ground traction and reduce power consumption. The algorithm uses models developed earlier in the thesis. Simulation and experimental results show that the algorithm leads to improved wheel thrust and thus increased mobility in rough terrain.

Thesis Supervisor:     Steven Dubowsky
                       Professor of Mechanical Engineering

# Acknowledgments

I would like to thank Professor Steven Dubowsky for his guidance and advice during the research and writing of this thesis. I would also like to thank Eric Baumgartner of the Jet Propulsion Laboratory and Hassan Shibly of Birzeit University for their technical contributions to this work. Thanks also to my colleagues (past and present) of the FSRL for their daily assistance and encouragement.

Last and most importantly, I would like to thank my family, for everything.

# Table of Contents

# List of Figures

*List of Figures*                                                                      10

# List of Tables

# Chapter

# 1

# Introduction

## 1.1 Problem Statement and Motivation

Mobile robots are increasingly being used in high-risk, rough terrain situations, such as planetary exploration. One notable example was the NASA / Jet Propulsion Laboratory (JPL) Sojourner rover on Mars (see Figure 1.1) (Golombek, 1998). However, the scope of the Pathfinder mission was limited to short traverses in relatively benign terrain, under constant human supervision. This can be observed from an overhead polar view of Sojourner's daily traversal map and from mission data (see Figure 1.2) (Golombek, 1998):

- Total distance traveled: ≈ 52 meters

- Total mission duration: 83 days

- Maximum radial distance traveled from lander: ≈ 10 meters

- Rock density: ≈ 1.5% by area, for rocks greater than 0.5 meters high

- Average local terrain slope: ≤ 5° inclination

- Degree of autonomy: none (Sojourner was teleoperated)

**Figure 1.1**: Sojourner rover operating in Martian terrain (Mars Pathfinder web site: http://mars.jpl.nasa.gov/MPF/index1.html)
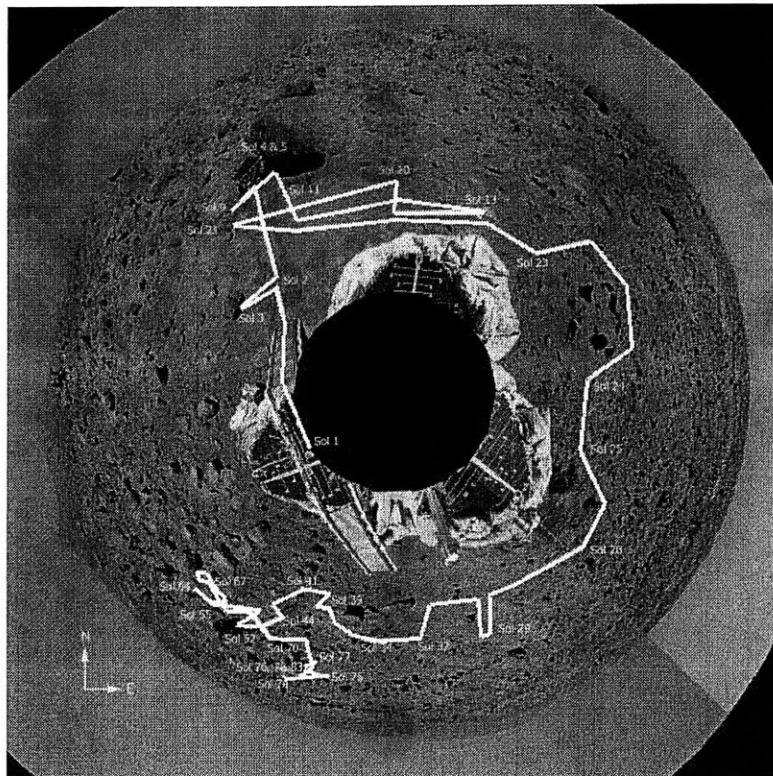


**Figure 1.2**: Overhead polar view of Sojourner traversal route (white) (Mars Pathfinder web site: http://mars.jpl.nasa.gov/MPF/index1.html)

Future planetary exploration missions will require rovers to perform more difficult tasks in increasingly challenging terrain, with limited human supervision (Hayati, 1996; Matijevic, 1997(c); Schenker, 1997). To accomplish this, future rover designs may evolve from traditional "fixed configuration" designs to designs with actively reconfigurable suspensions (Schenker *et al.*, 2000). Projected future mission requirements include:

- Travel distance: 1000s of meters

- Mission duration: 100s of days

- Rock density: 10-20% by area

- Average local terrain slope: $\leq 25°$ inclination

- Required degree of autonomy: local motion planning capability (i.e. the ability

    to plan a route to a scientific goal 5-10 rover lengths distant)

Current motion planning and control algorithms are not well suited to rough-terrain, since they generally do not consider the physical capabilities of the rover and its environment. Failure to understand these capabilities could lead to endangerment of the rover. For example, failure to understand whether or not a large rock can be safely traversed could lead to rover entrapment and mission failure. Alternatively, failure to understand the system's capabilities could cause unnecessarily conservative behavior. This could limit the ability of the rover to reach valuable science targets.

In summary, to accomplish planned future missions, rovers will need to understand their physical properties, and the properties of the terrain they are traversing. They must also be able to accomplish planned tasks with some degree of autonomy, while ensuring rover safety.

## 1.2 Purpose of this Thesis

The purpose of this thesis is to develop methods for improving mobile robot mobility in high-risk, rough-terrain environments, through the use of physical models of the rover and terrain. Rough terrain is defined here as terrain that includes natural features that could cause robot entrapment or loss of stability. This thesis will address three basic questions related to rough-terrain rover mobility: "What can a rover do?," "What should a rover do?," and "How should a rover do it?"

To address the question, "What can a rover do?," models of an articulated mobile robot operating in rough terrain will be presented. A model of the rover-terrain interaction mechanics will also be presented. Methods for estimating local terrain properties, including wheel-terrain contact angles and terrain physical properties, will also be presented. The purpose of this work is to allow a rover to accurately assess whether or not a proposed terrain region can be safely traversed.

To address the question, "What should a rover do?," a rough-terrain motion planning algorithm will be presented. An algorithm for geometrically reconfiguring the rover kinematic structure will also be presented. Both of these methods utilize models developed earlier in the thesis. The purpose of this work is to allow a rover to autonomously determine a safe, rapid path through a proposed terrain region, while continuously optimizing its kinematic structure to guard against tipover instability.

To address the question, "How should a rover do it?," a rough terrain control algorithm will be presented. The algorithm uses models developed earlier in the thesis to minimize wheel slip and improve traction. The purpose of this work is to allow a rover to successfully traverse a highly challenging terrain region.

## 1.3   Background and Literature Review

In this section a summary of literature related to this thesis is presented. This review is divided into sections that address the questions, "What can a rover do?," "What should a rover do?," and "How should a rover do it?"


### 1.3.1   Rough-Terrain Modeling: What Can a Rover Do?

Modeling of articulated mobile robots has been studied by numerous researchers. General kinematic analysis has been studied in (Milesi-Beller et al., 1993; Sreenivasan and Nanua, 1996; Sreenivasan and Waldron, 1996). Kinematic studies of six-wheeled rocker-bogie rovers such as the JPL Sojourner rover have been presented in (Chottiner, 1992; Linderman and Eisen, 1992; Hacot, 1998; Tarokh et al., 1999). Force analyses of mobile robots have also been performed. The mobile robot force analysis problem is similar to the force distribution problem in closed kinematic chains and walking machines, which have been studied in (Kumar and Gardner, 1990; Kumar and Waldron, 1990). Active coordination of forces in multi-wheeled systems was first proposed in (Kumar and Waldron, 1989), and was later addressed in (Sreenivasan, 1994; Sreenivasan and Nanua, 1996). This thesis does not attempt to make a fundamental contribution to modeling of articulated mobile robots. However, these models will form a basis for further analysis and are included for completeness.

Wheel-terrain contact angles are important elements of a rover model (see Figure 1.3). These angles greatly influence rover force application properties. For example, a rover traversing flat, even terrain has very different mobility characteristics than one traversing steep, uneven terrain. Previous researchers have proposed installing multi-axis

force sensors at each wheel hub to measure the contact force direction (Sreenivasan and Wilcox, 1994). Wheel-terrain contact angles could be inferred from the contact force direction. However, installing multi-axis force sensors at each wheel is costly and mechanically complex. A method for contact angle estimation has been proposed that is based on knowledge of the terrain map (Balaram, 2000). However, the terrain map is usually not well known. This method is also computationally intensive. In this thesis a method is presented for wheel-terrain contact angle estimation that utilizes simple on-board sensors and is computationally efficient (Iagnemma and Dubowsky, 2000(a)).
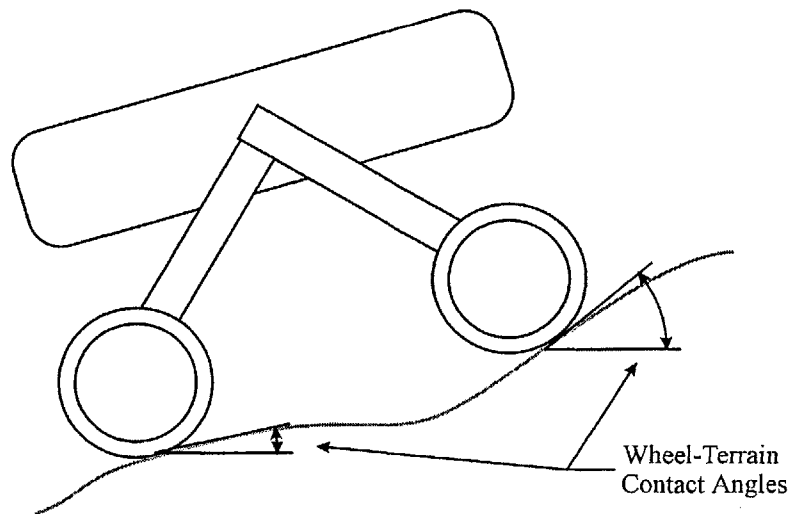


**Figure 1.3**: Wheel-terrain contact angles

Another important and often neglected aspect of rover system modeling is wheel-terrain interaction modeling. Wheel-terrain interaction has been shown to play a critical role in rough-terrain mobility (Bekker, 1956). Fundamental research into wheel-terrain interaction mechanics was pioneered by Bekker (Bekker, 1956; Bekker, 1969). Many researchers have studied methods for identifying key wheel-terrain interaction model parameters (Nohse et al., 1991; Shmulevich et al., 1996). In general these methods involve off-line estimation using costly, dedicated testing equipment.

For planetary rovers, it is desirable to estimate terrain parameters on-line (i.e. during rover motion). This would allow a rover to adapt its planning and control strategies to a given terrain. For example, a rover travelling over loose, sandy soil should behave much differently than a rover travelling over firm clay.

Wheel-terrain parameter estimation for a legged system has been documented in (Caurin and Tschichold-Gurman, 1994). This approach uses an embedded three-axis force sensor, which most rovers are not equipped with. Wheel-terrain parameter estimation for tracked vehicles has been proposed in (Le et al., 1997). This approach requires knowledge of the vehicle forward velocity, which is generally unknown. It also assumes a highly simplified "force coefficient" model of track-terrain interaction, which is not valid in rough terrain. Parameter estimation of Martian soil has been performed by the Sojourner rover (Matijevic et al., 1997(a)). This approach utilizes visual cues and off-line analysis. In this thesis, a method for on-line estimation of terrain the rover is currently traversing is presented. This allows accurate assessment of traversability, and can be used to improve motion planning and control.

### 1.3.2  Rough-Terrain Planning: What Should a Rover Do?

Future missions will require rovers to autonomously determine a safe traversal route to a distant science target. This is referred to as a motion planning problem. Numerous planning methods have been proposed using techniques such as quadtrees, graph-search methods, potential fields, and fuzzy logic (Warren, 1993; Haddad et al., 1998; Yahja et al., 1998; Seraji, 1999). A survey of many "traditional" planning methods can be found in (Latombe, 1991).

Many traditional motion planning methods cannot be successfully applied in rough-terrain, since they ignore vehicle and terrain mechanics, assume perfect knowledge of the environment, and represent obstacles and free space in a binary format (Latombe, 1991). Additionally, many traditional planning methods are computationally inefficient. These factors are critical to rough-terrain planning for several reasons. First, in rough terrain the concept of an obstacle is not clearly defined, as it depends on an understanding of the terrain and the mobility characteristics of the rover. Second, terrain data cannot be assumed to be perfectly known, due to errors in range sensing techniques (Hebert and Krotkov, 1992; Matthies and Grandjean, 1994). Third, the planned path may not be accurately followed by the rover due to path-following errors (Volpe, 1999). Finally, planetary exploration systems will generally have limited computational resources to devote to path planning.

Some researchers have begun addressing the rough-terrain planning problem. First works were dedicated to computing dynamic, time-optimal paths through rough terrain (Schiller and Chen, 1990). Other researchers have utilized dynamic vehicle models to ensure that proposed paths do not cause vehicle tipover (Olin and Tseng, 1991; Kelly and Stentz, 1998). Employing a kinematic model to evaluate traversability at a large number of points in the configuration space of the rover's position and heading has been proposed in (Siméon and Dacre-Wright, 1993; Cherif and Laugier, 1994; Farritor et al., 1998(a); Farritor, 1998(b); Cherif, 1999). Model-based slip-free motion planning for an articulated vehicle has been proposed (Choi and Sreenivasan, 1998). All of these methods recognize the importance of model-based analysis to ensure path traversability. However, they utilize simplified terrain models and do not consider uncertainty.

Another class of algorithms are based largely on determining the smoothest path through a given terrain region. One approach uses fractals to model terrain, and searches for a path with a consistently low fractal dimension (Pai and Reissel, 1998). Another method models obstacles with potential fields, and searches for a path with low potential (Chanclou and Luciani, 1996). A fuzzy logic-based method has been proposed that uses gross knowledge of terrain slope and roughness to avoid hazardous regions (Seraji, 1999). A sensor-based method has been implemented that classifies obstacles in a binary manner and determines an obstacle-free path (Laubach *et al.*, 1998; Laubach and Burdick, 1999). These methods do not consider vehicle mechanics, or allow for uncertainty. They attempt to avoid highly rough terrain, and implicitly assume that the planned path is free of hazards. Thus, they may be effective in flat terrain with "discrete" obstacles, such as large boulders, but may not be well suited to truly rough, uneven terrain.

In summary, with the exception of (Ben Amar and Bidaud, 1995) most proposed planning methods do not employ a realistic terrain model. This is critical to an accurate assessment of terrain traversability. Additionally, with the exception of (Gifford and Murphy, 1996; Hait and Siméon, 1996), most proposed planning methods do not consider uncertainty in the terrain data or rover path-following accuracy. In rough terrain, failure to account for uncertainty can lead to mission failure, an unacceptable result. A strong argument can be made that for rough-terrain rover planning, it is better to plan a safe path than an "optimal" one (i.e. one that optimizes a criteria, such as path length, but causes the rover undue risk). In this thesis a planning method is presented that utilizes model-based analysis of rover-terrain interaction, and considers terrain data and path-following

uncertainty (Iagnemma *et al.*, 1999(a)). It is also computationally efficient enough for on-board implementation.

Another important aspect of future missions is that rovers may evolve from traditional "fixed configuration" designs to designs with actively reconfigurable suspensions (Schenker *et al.*, 2000). Actively reconfigurable robots can reposition their center of mass to improve tipover stability in rough terrain. For example, when traversing an incline, an actively reconfigurable robot can adjust its suspension to increase its stability margin (see Figure 1.4).
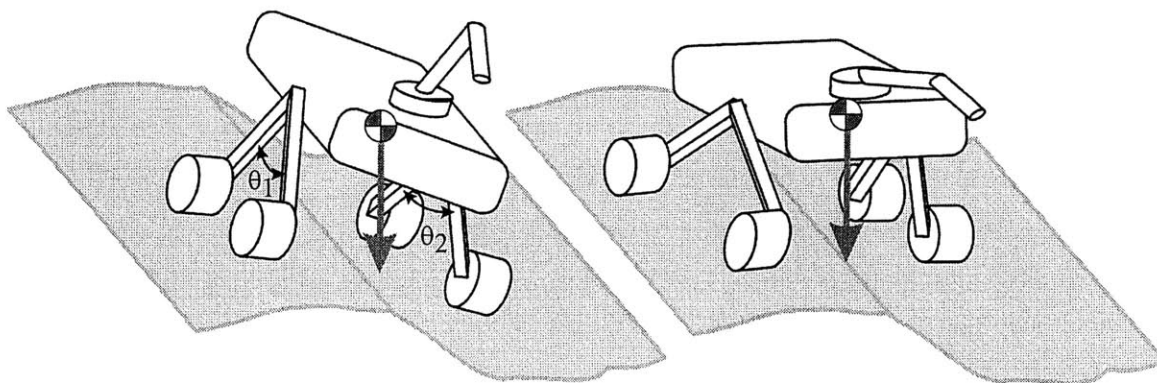


**Figure 1.4:** A reconfigurable robot improving rough-terrain tipover stability by adjusting joint angles $\theta_1$ and $\theta_2$

Previous researchers have suggested the use of kinematic reconfigurability to enhance rough-terrain mobility (Sreenivasan, and Wilcox, 1994; Sreenivasan, and Waldron, 1996; Farritor *et al.*, 1998(a)). In (Sreenivasan, and Wilcox, 1994) a simple planar system is reconfigured based on an ad-hoc stability metric. In (Farritor *et al.*, 1998(a)) a computationally intensive genetic algorithm is used to determine an optimal kinematic configuration for a given task. None of the previously proposed methods have been demonstrated on an experimental rover system in rough terrain. In this thesis an efficient

method for kinematic reconfigurability is presented, and applied experimentally to the JPL Sample Return Rover (SRR) (Huntsberger *et al.*, 1999; Iagnemma *et al.*, 2000(c)).

### 1.3.3 Rough-Terrain Control: How Should a Rover Do It?

In rough terrain, it is critical for mobile robots to maintain adequate wheel traction. Excessive wheel slip could cause a rover to lose control and become trapped. Substantial work has been performed on traction control of passenger vehicles operating on flat roads (Mohan and Williams, 1995; Kawabe et al., 1997; Van Zanten *et al.*, 1997; Van Zanten *et al.*, 1998). These approaches rely on mechanical torque distribution systems, such as differentials, which mobile robots are not equipped with. Fuzzy logic wheel-slip control has been proposed for passenger vehicles on paved roads (Mauer, 1995; Cheok *et al.*, 1997). These methods assumes that the vehicle forward velocity is known, which allows computation of wheel slip. The wheel slip is then used as a control variable. The forward velocity is generally unknown for mobile robots.

Researchers have proposed a variable-structure control approach for traction control of passenger vehicles on paved roads that does not utilize a mechanical differential (Tan and Chin, 1991; Tan and Chin, 1992; Lee and Tomizuka, 1996). However, these approaches assume a form of the traction-slip ratio relationship that is valid only for deformable tires on hard terrain. Off-road wheel-terrain interaction mechanics are substantially different and more complex, since the wheel may be rigid and the terrain is generally soft.

Traction control for low-speed mobile robots on flat terrain has been studied (Reister and Unseren, 1993). Later work has considered the important effects of terrain

unevenness (Sreenivasan and Wilcox, 1994). This work assumes knowledge of terrain

geometry and soil characteristics, and has not been validated experimentally. In

applications such as planetary exploration the terrain geometry and soil characteristics are

usually unknown. A fuzzy-logic traction control algorithm for a rocker-bogie rover that

did not assume knowledge of terrain geometry has been developed (Hacot, 1998). This

approach is based on heuristic rules related to vehicle mechanics, and again assumes that

the wheel slip ratio is measurable, which is generally not true for slow-moving rovers. In

this thesis a rough-terrain control method is presented that utilizes simple sensory inputs

to optimize for maximum wheel traction or minimum power consumption, depending on

the local terrain difficulty (Iagnemma and Dubowsky, 2000(b)). It does not rely on

mechanical torque distribution systems or measured wheel slip.


## 1.4    Outline of this Thesis

This thesis is composed of five chapters and three appendices. This chapter serves as an

introduction and overview of the work, and summarizes related research.

Chapter 2 addresses the question "What can a rover do?" by presenting models for

mobile robot kinematic analysis, force analysis, and wheel-terrain interaction. A method

for on-line estimation of important terrain physical parameters is presented. A method

for estimating wheel-terrain contact angles from on-board sensors is also presented.

Simulation and experimental results are presented for a six-wheeled rover in rough, sandy

terrain.

Chapter 3 addresses the question "What should a rover do?" by presenting two

rough-terrain motion planning methods. The goal of the first planning method is to find a

safe, direct path from the rover's current position to a goal position several rover lengths distant. The goal of the second planning method is to determine the optimal state of a kinematically reconfigurable rover, for improved tipover stability during travel in rough terrain. Simulation and experimental results are presented for the JPL SRR operating in outdoor terrain.

Chapter 4 addresses the question "How should a rover do it?" by presenting a servo-level control method for improved wheel traction or reduced power consumption in rough terrain. Simulation and experimental results are presented for a six-wheeled rover in rough sandy terrain.

Chapter 5 summarizes the contributions of this thesis and presents suggestions for future work.

The appendices to this thesis give detailed information on specific topics related to the work presented. Appendix A presents a kinematic and force analysis of a six-wheeled mobile robot. Appendix B presents a series of equations related to wheel-terrain interaction mechanics. Appendix C describes the Field and Space Robotics Laboratory six-wheeled microrover testbed, which is used to experimentally validate much of this work. Appendix D presents a description of an Extended Kalman Filter (EKF) that is used for wheel-terrain contact angle estimation.

<div align="right">

**Chapter**

# 2

</div>

# Rough-Terrain Modeling: What Can a Rover Do?

## 2.1   Introduction

This chapter presents physical models of rovers and terrain that will be used throughout this thesis. Section 2.2 briefly describes important aspects of mobile robot kinematic and force analysis, with more detailed analysis presented in Appendix A. Section 2.3 presents a model of rover wheel-terrain interaction, and a method for on-line terrain parameter estimation. Section 2.4 presents results of terrain parameter estimation simulations and experiments, and shows that critical parameters of sandy soil can be estimated with good accuracy. Section 2.5 describes a method for on-line estimation of wheel-terrain contact angles. Section 2.6 presents results of wheel-terrain contact angle estimation simulations and experiments, and shows that wheel-terrain contact angles can be accurately estimated using simple on-board sensors. Section 2.7 is a summary of the chapter and presents conclusions drawn from the work.

## 2.2    Rover Kinematic and Force Analysis

In this thesis the general problem of mobile robot kinematic and force analysis on uneven terrain is not addressed.    For completeness, the application of kinematic and force analysis to terrain traversability prediction is briefly discussed.    Detailed kinematic and force analyses of a six-wheeled rocker-bogie rover with a rocker-bogie suspension, similar to the Sojourner rover mobile robot, are presented in Appendix A.

### 2.2.1    Rover Kinematic Analysis

The purpose of kinematic analysis is to determine if a rover can physically conform to a given region without violating joint limit or interference constraints.    In this work the inverse kinematics problem is of primary interest, and can be stated as follows: *Given an elevation map of the terrain and the position of the center of the rover body, compute the orientation of the rover body and the configuration of the rover suspension.*    An illustration of the inverse kinematics problem is shown in Figure 2.1.
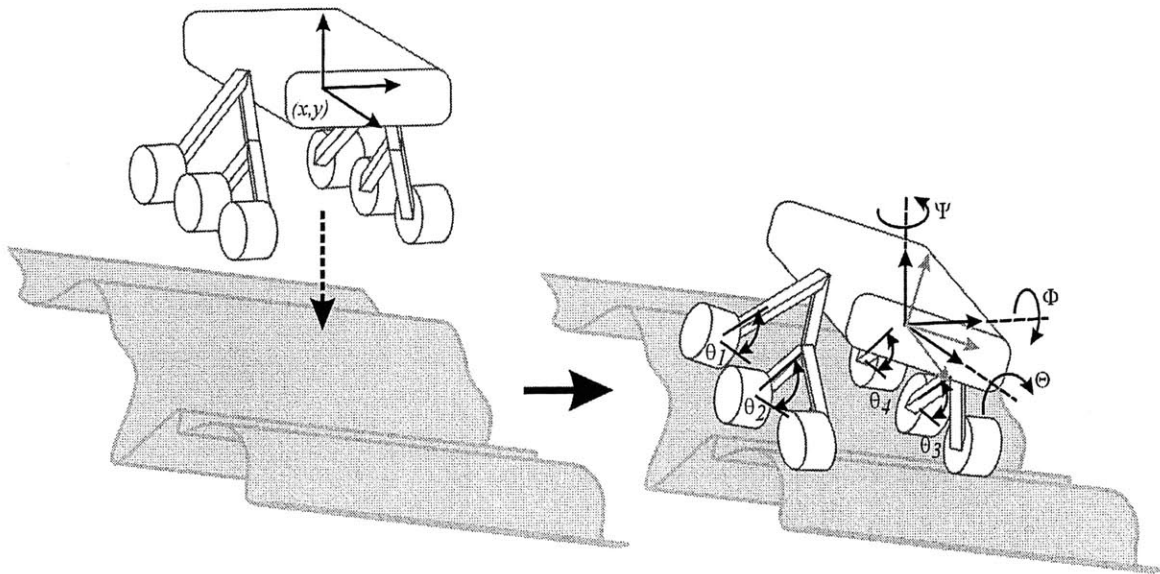


**Figure 2.1**: Illustration of rover inverse kinematics problem

A more rigorous definition of the inverse kinematics problem and a solution for a six-wheeled rover are presented in Appendix A. It should be noted that the solution of the inverse kinematics problem for a multi-wheeled rover involves simultaneous solution of multiple nonlinear equations, which is a nontrivial problem.

Kinematic analysis is used throughout this work as a basis for terrain traversability analysis, since terrain regions that cause the rover to violate kinematic constraints are clearly untraversable. Kinematic analysis is also used for vehicle stability analysis, since static stability is a function of only the rover orientation and configuration.

## 2.2.2 Rover Force Analysis

The purpose of force analysis is to determine if the rover can exert enough thrust at the wheel-terrain interface to produce motion in a desired direction without violating motor torque saturation or terrain traction constraints. The force analysis problem can be stated as follows: *Given the rover configuration and wheel-terrain contact angles, determine if a set of wheel-terrain contact forces exist that balance a body force vector in the direction of desired motion.*

See Figure 2.2 for an illustration of the rover force analysis problem. A detailed analysis of the mobile robot force analysis problem is presented in Appendix A. It should be noted that a force analysis of a mobile robot is an underconstrained problem (i.e. one with more unknown variables than equations), and cannot always be solved using simple linear algebraic techniques.
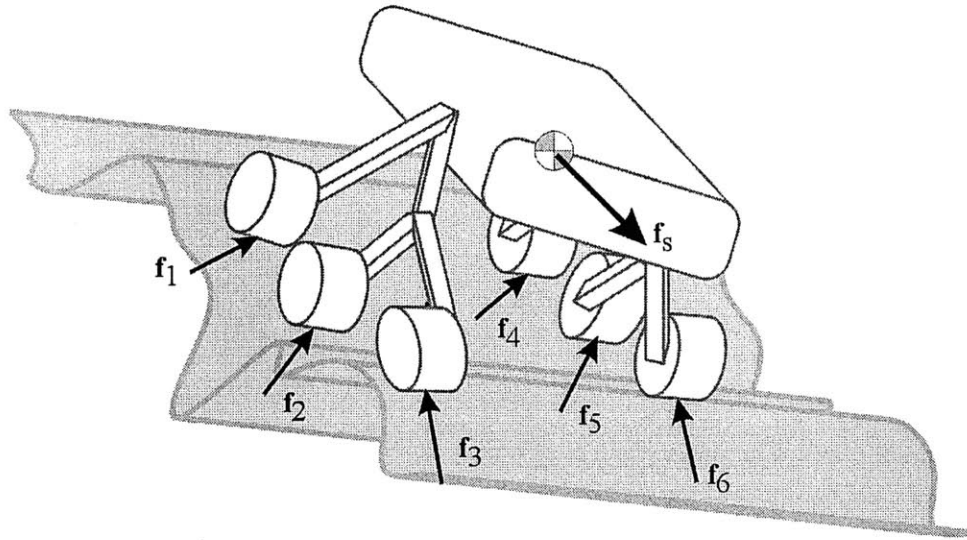
**Figure 2.2**: Illustration of rover force analysis

Force analysis is used throughout this work as a basis for terrain traversability analysis, since terrain regions that have unusually high motion resistance (due to a high degree of roughness, for example) may be untraversable.

## 2.3    Terrain Characterization and Identification

Wheel-terrain interaction has been shown to play a critical role in rough-terrain mobility (Bekker, 1956). The purpose of terrain characterization and identification is to identify key terrain parameters, which can be used as part of a wheel-terrain interaction model. This will enable accurate terrain traversability prediction. The following work was performed in collaboration with Dr. Hassan Shibly while he was a visiting scholar at MIT. A summary of this work can be found in (Shibly *et al.*, 2000).

In this thesis the case of a smooth rigid wheel traveling through deformable terrain is considered. This analysis is one of four possible wheel-terrain cases. Other cases are 1)

a rigid wheel traveling over rigid terrain, 2) a deformable wheel traveling over rigid terrain, and 3) a deformable wheel traveling over deformable terrain (see Figure 2.3).
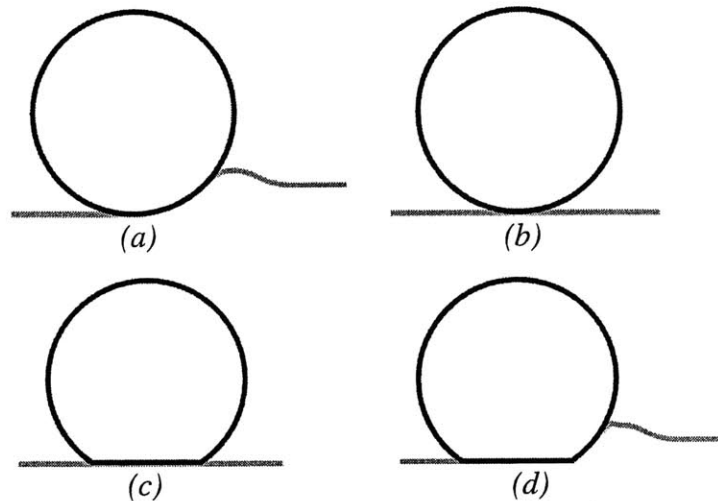


**Figure 2.3:** Four cases of wheel-terrain interaction mechanics: (a) rigid wheel traveling over deformable terrain, (b) rigid wheel traveling over rigid terrain, (c) deformable wheel traveling over rigid terrain, and (d) deformable wheel traveling over deformable terrain

It is important to distinguish between these cases, as fundamental wheel-terrain mechanics vary depending on the interaction mechanics (Bekker, 1969; Plackett, 1985; Wong, 1993). Here the case of a rigid wheel in deformable terrain is examined, as this is the expected condition for planetary exploration vehicles (e.g. the Sojourner Rover on Mars). Note, however, that this case is common in terrestrial vehicles, since a pneumatic tire can be considered rigid if its inflation pressure is high compared to the terrain stiffness (Bekker, 1969). In conclusion, proper analysis of a wheel-terrain system depends on the relative stiffness of both the wheel and terrain.

It should be noted that wheel-terrain interaction mechanics are similar for smooth wheels and wheels with grousers or treads. Grouser and tread effects can generally be considered by appending "surcharge" terms to wheel-terrain interaction equations (Bekker, 1969).

To estimate terrain physical parameters, equations relating the parameters of interest to physically measurable quantities (such as force, velocity, etc.) must be developed. A free-body diagram of a driven rigid wheel traveling through deformable terrain is shown in Figure 2.4. A vertical load $W$ and a horizontal force $DP$ are applied to the wheel by the vehicle suspension. A torque $T$ is applied at the wheel rotation axis by an actuator. The wheel has angular velocity $\omega$, and the wheel center possesses a linear velocity, $V$. The angle from the vertical at which the wheel first makes contact with the terrain is denoted $\theta_1$. The angle from the vertical at which the wheel loses contact with the terrain is denoted $\theta_2$. Thus, the entire angular wheel-terrain contact region is defined by $\theta_1 + \theta_2$.

$W$

$T, \omega$

$DP$

$V$

$\theta_1$

$\theta_2$

$\theta$

$\tau$

$z$

$\theta_m$

$\sigma$

$\sigma_2$

$\sigma_1$
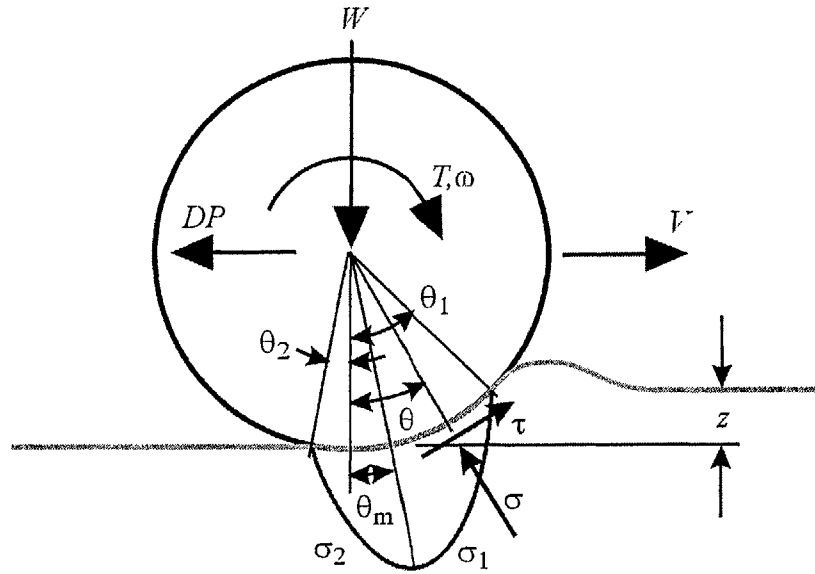
**Figure 2.4**: Free-body diagram of rigid wheel on deformable terrain

In the following analysis the vertical load $W$ and the torque $T$ are assumed to be known quantities. The vertical load $W$ can be computed from a static analysis of the rover, with knowledge of the mass distribution. Static analysis is valid due to the low speeds of these vehicles (i.e. on the order of 10 cm/sec). The torque $T$ can be estimated with reasonable accuracy from the current input to the wheel motor.

A stress region is created at the wheel-terrain interface, and is indicated by the regions $\sigma_1$ and $\sigma_2$. At a given point on the interface, the stress can be decomposed into a component acting normal to the wheel at the wheel-terrain contact point, termed the normal stress, $\sigma$, and a stress acting parallel to the wheel at the wheel-terrain contact point, termed the shear stress, $\tau$. The angle from the vertical at which the maximum stress occurs is denoted $\theta_m$.

A semi-empirical expression for the shear stress as a function of the angle $\theta$ has been proposed by Bekker as:

$$\tau(\theta) = (c + \sigma(\theta)\tan\phi)(1 - e^{-j/k})$$ (2.1)

where $c$ is the soil cohesion, $\phi$ is the soil internal friction angle, $j$ is the shear deformation, and $k$ is a constant (Bekker, 1956). This equation is derived from elasticity theory. A modification of this equation was introduced that relates the shear deformation of a point on the wheel rim to wheel slip, as:

$$\tau(\theta) = (c + \sigma(\theta)\tan\phi)\left(1 - e^{-\frac{r}{k}[\theta_1 - \theta - (1-i)(\sin\theta_1 - \sin\theta)]}\right)$$ (2.2)

where $i$ is the wheel slip, and is defined by $i = 1 - (V/r\omega)$ (Onafko and Reece, 1967). This equation is more convenient for physical experimentation purposes, as wheel slip is a more readily measurable quantity than shear deformation.

Bekker has also proposed a general expression for normal stress:

$$\sigma(z) = (k_1 + k_2 b)\left(\frac{z}{b}\right)^n$$ (2.3)

where $z$ is the vertical sinkage (see figure 2.4), $b$ is the wheel width, and $k_1$ and $k_2$ are constants (Bekker, 1956). An expression for the normal stress as a function of the

angular location $\theta$ on the wheel rim is desirable. This is accomplished by expressing the sinkage of any point on the wheel as a function of the angular location $\theta$:

$$z(\theta) = r(\cos\theta - \cos\theta_1)$$  (2.4)

Substituting Equation (2.4) into Equation (2.3) yields an expression for the distribution of the normal stress along the wheel-terrain contact surface, as:

$$\sigma_1(\theta) = (k_1 + k_2 b)\left(\frac{r}{b}\right)^n (\cos\theta - \cos\theta_1)^n$$  (2.5)

$$\sigma_2(\theta) = (k_1 + k_2 b)\left(\frac{r}{b}\right)^n \left(\cos\left(\theta_1 - \frac{\theta}{\theta_m}(\theta_1 - \theta_m)\right) - \cos\theta_1\right)^n$$  (2.6)

Examination of Figure 2.4 shows that the stresses beneath the wheel balance the vertical load $W$ on the wheel, the net forward force or "drawbar pull" $DP$, and the torque $T$ at the wheel axle. These force balance equations can be written as:

$$W = rb\left(\int_{\theta_2}^{\theta_1} \sigma(\theta)\cos\theta \cdot d\theta + \int_{\theta_2}^{\theta_1} \tau(\theta)\sin\theta \cdot d\theta\right)$$  (2.7)

$$DP = rb\left(\int_{\theta_2}^{\theta_1} \tau(\theta)\cos\theta \cdot d\theta - \int_{\theta_2}^{\theta_1} \sigma(\theta)\sin\theta \cdot d\theta\right)$$  (2.8)

$$T = r^2 b\int_{\theta_2}^{\theta_1} \tau(\theta) \cdot d\theta$$  (2.9)

Soil physical parameters and the drawbar pull $DP$ are unknown quantities in Equations (2.1-2.9). The soil parameters of interest are the cohesion $c$ and the internal friction angle $\phi$. Knowledge of these parameters allows estimation of the maximum drawbar pull $DP$ (or net forward force) that a given wheel-terrain system can generate. This in turn allows prediction of the traversability of a given terrain region.

Analytical solutions to Equations (2.7-2.9) are required to facilitate symbolic manipulation. Symbolic manipulation is necessary to attain closed-form expressions for the cohesion and internal friction angle. However, the analytical solutions of Equations (2.7-2.9) are not amenable to manipulation. This complexity motivates the use of an approximate form of the fundamental stress equations.

### 2.3.1 Equation Simplification

Figure 2.5 is a plot of the shear and normal stress distributions (as defined by Equations (2.2) and (2.3), respectively) around the rim of a driven rigid wheel on deformable terrain for varying sinkage coefficients $n$. Note that although $n$ has the largest influence on the shape of the stress distribution curves, the variables $\theta_1$, $\phi$, $r$, $k$, and $i$ also weakly influence the shape. However, it has been observed that $n$ dominates the shape of the stress distribution curves, and is thus the primary parameter of interest.
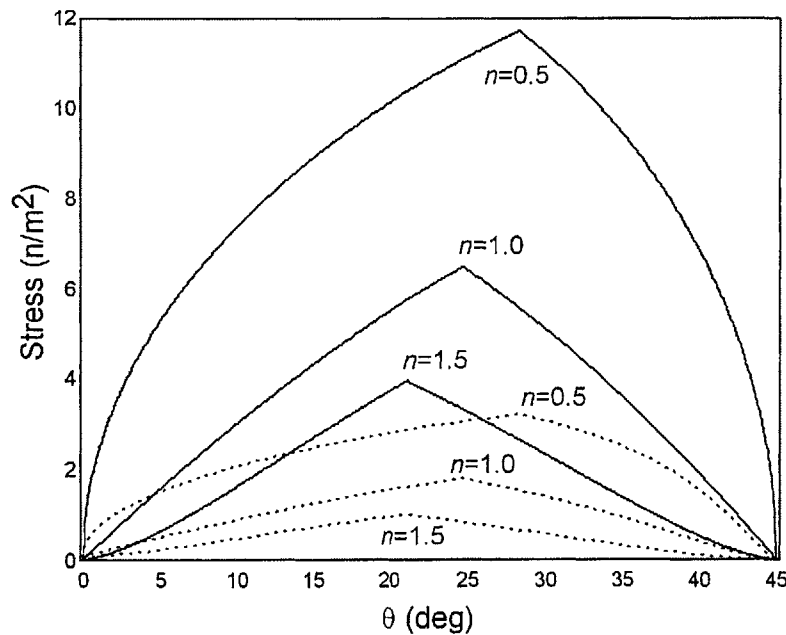


**Figure 2.5**: Normal stress (solid) and shear stress (dotted) distribution around the rim of a driven rigid wheel on deformable terrain for varying sinkage coefficients $n$

The shear and normal stress distribution curves are approximately triangular for a wide range of $n$. This observation was first made by (Vincent, 1961) but was not used for modeling purposes. Based on this observation, a linear approximation of the shear and normal stress distribution equations can be written as:

$$\sigma_1(\theta) = -\frac{\sigma_m}{\theta_1 - \theta_m}\theta + \frac{\sigma_m\theta_1}{\theta_1 - \theta_m} \tag{2.10}$$

$$\sigma_2(\theta) = \frac{\sigma_m}{\theta_m}\theta \tag{2.11}$$

$$\tau_1(\theta) = -\frac{\tau_m}{\theta_1 - \theta_m}\theta + \frac{\tau_m\theta_1}{\theta_1 - \theta_m} \tag{2.12}$$

$$\tau_2(\theta) = \frac{\tau_m}{\theta_m}\theta \tag{2.13}$$

Simulations were conducted to compare the linear approximations (Equations (2.10-2.13)) to the original equations (Equations (2.2-2.3)). Approximately 15,000 simulations were conducted in the following parameter ranges:

$$-0.2 < n < 1.5$$

$$-25.0 < \theta_1 < 55.0$$

$$-20.0 < \phi < 32.0$$

$$-3.0 < r < 15.0$$

$$-0.1 < k < 1.00$$

$$-0.0 < i < 1.0$$

These parameter ranges are reasonable for small planetary exploration rovers traveling on soft to moderately firm terrain. An average difference of 10.4% was found

between the approximate and actual shear stress distribution equations, and 9.6% between the approximate and actual normal stress distribution equations. Thus, the linear approximations were considered sufficiently accurate representations of the true functions.

Simplified forms of the force balance equations can now be written by combining Equations (2.7-2.9) and Equations (2.10-2.13), as:

$$W = rb\left( \int_{\theta_m}^{\theta_1} \sigma_1(\theta)\cos\theta \cdot d\theta + \int_0^{\theta_m} \sigma_2(\theta)\cos\theta \cdot d\theta + \int_{\theta_m}^{\theta_1} \tau_1(\theta)\sin\theta \cdot d\theta + \int_0^{\theta_m} \tau_2(\theta)\sin\theta \cdot d\theta \right) \quad (2.14)$$

$$DP = rb\left( \int_{\theta_m}^{\theta_1} \tau_1(\theta)\cos\theta \cdot d\theta + \int_0^{\theta_m} \tau_2(\theta)\cos\theta \cdot d\theta - \int_{\theta_m}^{\theta_1} \sigma_1(\theta)\sin\theta \cdot d\theta - \int_0^{\theta_m} \sigma_2(\theta)\sin\theta \cdot d\theta \right) \quad (2.15)$$

$$T = r^2 b\left( \int_{\theta_m}^{\theta_1} \tau_1(\theta) \cdot d\theta + \int_0^{\theta_m} \tau_2(\theta) \cdot d\theta \right) \quad (2.16)$$

Evaluation of Equations (2.14) and (2.16) leads to the following expressions for the normal load and torque:

$$W = \frac{rb}{\theta_m(\theta_1 - \theta_m)}\left[\sigma_m\left(\theta_1\cos\theta_m - \theta_m\cos\theta_1 - \theta_1 + \theta_m\right) + \tau_m\left(\theta_1\sin\theta_m - \theta_m\sin\theta_1\right)\right] \quad (2.17)$$

$$T = \frac{1}{2}r^2 b\tau_m\theta_1 \quad (2.18)$$

The above two equations are functions of three unknowns: the maximum shear stress $\tau_m$, maximum normal stress, $\sigma_m$, and the angular location of the maximum stress, $\theta_m$. An additional equation can be written if the location of the maximum shear and normal stress are assumed to occur at the same location $\theta_m$. Figure 2.5 shows that this assumption is reasonable for a wide range of soil values. With this assumption, Equation (2.2) can be modified to relate $\tau_m$, $\sigma_m$, and $\theta_m$ as:

$$\tau_m = \left(c + \sigma_m \tan\phi\right)\left(1 - e^{-\frac{r}{k}[\theta_1 - \theta_m - (1-i)(\sin\theta_1 - \sin\theta_m)]}\right)$$ (2.19)

Theoretically the system of Equations (2.17), (2.18), and (2.19) can be solved for the unknown quantities $\tau_m$, $\sigma_m$, and $\theta_m$. However, symbolic manipulation of this system is difficult due to the complex form of the exponent in Equation 2.19. A simplified form of the exponent was written in the following form:

$$f = \frac{r(\theta_1 - \theta)}{2k}[(1 - \cos\theta_1) + i \cdot (1 + \cos\theta_1)]$$ (2.20)

This function is similar to the exponent in Equation (2.19) for a wide range of slip $i$ and $\theta_1$, as shown in Figure 2.6. Note that $\theta_m$ does not appear in Equation (2.20). This is allowable because in practice $\theta_m$ is generally small.
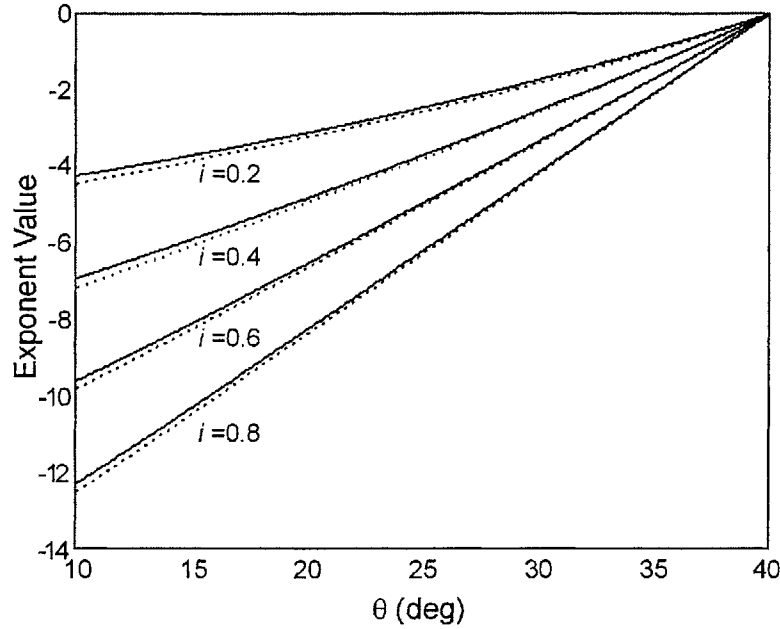


**Figure 2.6**: Value of $-\frac{r}{k}[\theta_1 - \theta_m - (1-i)(\sin\theta_1 - \sin\theta_m)]$ (solid) and modified function $f$ (dotted) for $\theta_l = 30°$ and varying slip $i$

Using the modified exponent form (Equation (2.20)), Equations (2.17) and (2.18) can be reformulated. The results of these expressions are given in Appendix B. These

equations have trigonometric and exponential forms which can be simplified by factorization and expansion. The result of the simplified equations for $W$, $DP$, and $T$ are (see also Appendix B):

$$W = rb\left(\frac{1}{3}ch_0\theta_1^2 + h_1\sigma_m + \sigma_m \tan\phi\left(h_3 + h_2\theta_1^2\right)\right) \quad (2.21)$$

$$DP = rb\left(ch_0 \sin\theta_1 + \sigma_m \tan\phi\left(h_1 + h_4 \sin\theta_1\right) - h_3\sigma_m\right) \quad (2.22)$$

$$T = r^2b\theta_1\left(ch_0 + \sigma_m \tan\phi\left(\frac{1}{2} + h_4\right)\right) \quad (2.23)$$

where $h_0$, $h_1$, $h_2$, $h_3$, and $h_4$ are functions of measured quantities. Their expressions are given in Appendix B. Thus, the equations for $W$, $DP$, and $T$ can be expressed as compact functions of measurable quantities.

Figure 2.7 shows a representative simulated result of the drawbar pull generated by a rigid wheel traveling on soft terrain. The input parameters are the soil parameters and the wheel normal load $W$ and torque $T$. The soil parameters were chosen to approximate sandy soil. The wheel torque was chosen to approximate actual driven-wheel data from a rover testbed. A comparison is presented between the numerically integrated drawbar pull equation proposed by (Wong and Reece, 1967), the simplified drawbar pull equation (the difference of Equations (B.2 and B.3)), and the modified simplified drawbar pull equation (Equation (2.23)).

It can be seen that the simplified and modified simplified equation agree closely with the original (i.e. Wong and Reece) equation. Simulation results generally showed agreement within 10% over a wide range of terrain parameters. Thus, it can be concluded that the simplified equations closely approximate the original, complex functions for a wide range of terrain parameters.
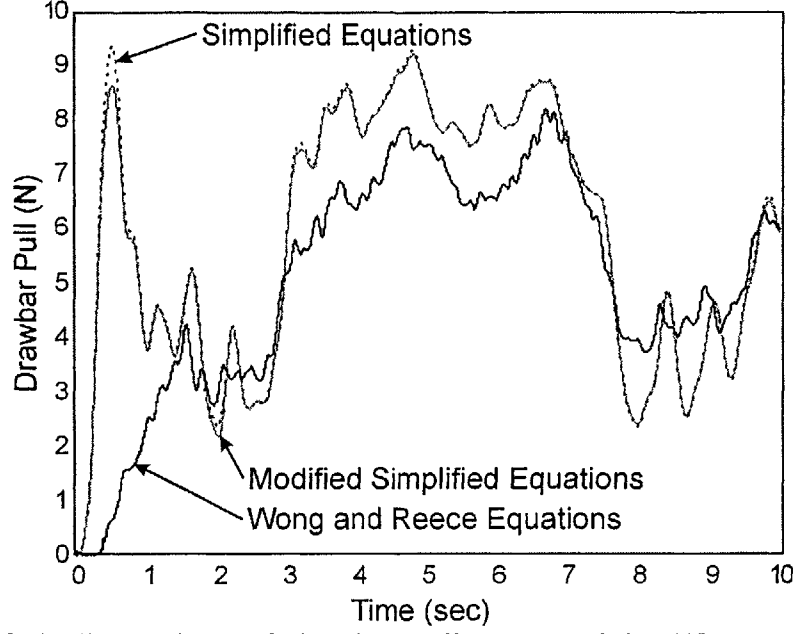
**Figure 2.7**: Comparison of drawbar pull computed by Wong and Reece wheel-terrain equations (solid black), simplified equations (dotted black), and modified simplified equations (solid gray)

It is now possible to symbolically manipulate the simplified closed-form expressions for $DP$, $W$, and $T$. The expressions can solved for the internal friction angle $\phi$, as:

$$\tan \phi = \frac{h_1 h_6 - c h_0 h_1}{h_8 - c h_9} \tag{2.24}$$

with the expressions for $h_0$, $h_1$, $h_6$, $h_8$ and $h_9$ given in Appendix B. Equation 2.21 is a single equation in the two unknowns $\phi$ and $c$. However, in homogeneous terrain the internal friction angle is constant. Thus, the left-hand side of Equation (2.24) remains constant during a terrain characterization experiment on a homogeneous terrain. For $n$ measurements in the same terrain, a set of equations can be written as:

$$\frac{h_1^1 h_6^1 - c h_0^1 h_1^1}{h_8^1 - c h_9^1} = \frac{h_1^2 h_6^2 - c h_0^2 h_1^2}{h_8^2 - c h_9^2}$$

$$\vdots \tag{2.25}$$

$$\frac{h_1^1 h_6^1 - c h_0^1 h_1^1}{h_8^1 - c h_9^1} = \frac{h_1^n h_6^n - c h_0^n h_1^n}{h_8^n - c h_9^n}$$

Each equation in the Equation set (2.25) can be solved as a quadratic in $c$. Two solutions for $c$ can be computed for each measurement, one of which is physically unreasonable (i.e. a negative value). The $n$ physically reasonable solutions of $c$ can be averaged to find a mean value of the soil cohesion.

With knowledge of the soil cohesion $c$, the internal friction angle $\phi$ can be computed from Equation (2.24), averaged over $n$ measurements, as:

$$\tan\phi = \frac{\displaystyle\sum_{i=1}^{n} \frac{h_1^i h_6^i - ch_0^i h_1^i}{h_8^i - ch_9^i}}{n} \tag{2.26}$$

Thus, estimates of soil cohesion $c$ and internal friction angle $\phi$ can be computed from sensor measurements taken during a wheel-terrain characterization experiment.

## 2.3.2 On-Line Terrain Parameter Identification

The preceding analysis can be applied to a physical rover system for on-line terrain parameter identification. In the preceding analysis it was assumed that the applied wheel torque $T$, wheel normal load $W$, wheel slip $i$, and sinkage $z$ were known. Methods for estimating these inputs will be discussed in this section. A method for on-line terrain parameter identification will then be presented.

*Input Variable Estimation*

The torque $T$, wheel normal load $W$, wheel slip $i$, and sinkage $z$ are inputs to the terrain parameter identification algorithm. The wheel torque $T$ can be estimated with knowledge of the current input to the motor. The wheel normal load $W$ can be determined from static analysis, assuming the rover mass parameters are known and that

dynamic forces are small compared to static forces. This assumption is reasonable for slow-moving planetary exploration rovers.

The wheel slip $i$ is generally unknown, since wheel forward velocity is difficult to measure. When a rover is traveling on flat terrain, however, slip can be accurately estimated. In this case the rover travels with very little slip, and thus wheel center speeds are approximately equal to the product of the wheel angular velocity and radius. By driving one wheel at a different rate than the others for a short period of time, slip can be accurately estimated for the driven wheel. This computation assumes that increasing the speed at a single wheel does not greatly influence the speed of the other wheels.

The wheel sinkage $z$ of a rover on flat terrain can be determined from differential analysis of the rover configuration, assuming the configuration is completely observable. The configuration $Q$ is defined here as the rover suspension angles and the roll, pitch, and yaw defined with respect to an inertial frame.

For a robot with $n$ wheels in contact with the terrain, at least $n$-1 kinematic loop closure equations can be written by relating the elevation $z$ of each stationary wheel to the driven wheel (see Appendix A for loop closure equations of a six-wheeled rover). The wheel sinkage can be determined by integrating the total derivative of the loop closure equations with respect to time, as:

$$\Delta z = \int_0^t dz(Q) \cdot dt \qquad (2.27)$$

where the sinkage computation begins at time $t = 0$ and ends at time $t$.

Since the integral paths are not relevant, the sinkage can be computed as the difference between the initial and final states, as:

$$\Delta z = z(Q)\big|_{Q_1}^{Q_2} \qquad\qquad (2.28)$$

Note that sensor noise and kinematic parameter uncertainty will introduce error in the above computations. Sinkage computation accuracy for a given kinematic loop equation will vary depending on its sensitivity to both noise and kinematic parameter error. A sensitivity analysis could be performed to determine which loop equations are least sensitive to noise, and thus most accurate.

The preceding analysis was applied experimentally to the six-wheeled FSRL experimental rover testbed (see Appendix C). The rover was driven over flat, sandy terrain. The right-rear wheel was driven for several seconds and the sinkage was estimated from on-board joint potentiometer and accelerometer readings. The results from two kinematic loops corresponding to Equations (A.2) and (A.3) were averaged to compute the sinkage. The results for five trials of varying time periods are plotted in Figure 2.8.
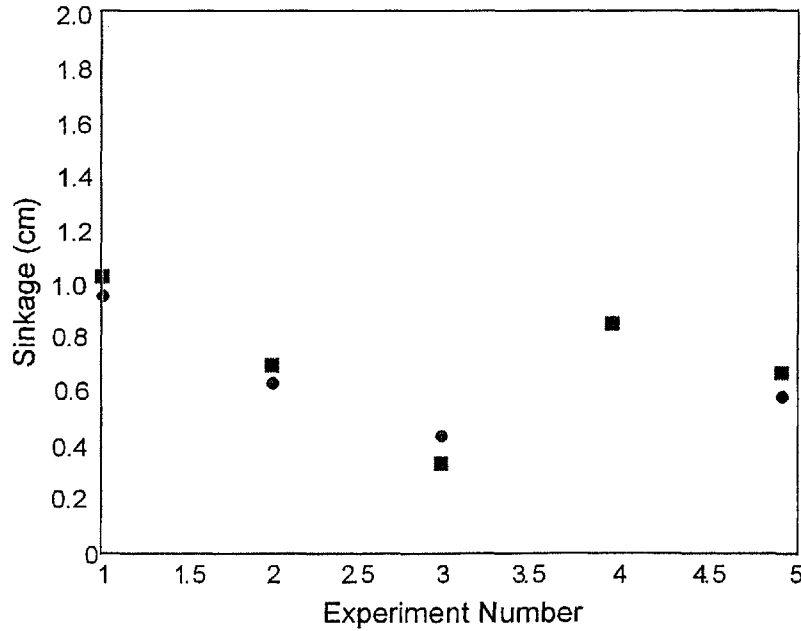


**Figure 2.8**: Measured (round) and estimated (square) sinkage on sandy soil

The RMS percent difference between the measured and actual sinkage is 13.4%. For a typical identification experiment on a small rover system, such as the FSRL rover, this represents an error of approximately 1 mm, which is equivalent to 0.035 radians along the rover wheel. This is deemed an acceptable error for the purposes of terrain parameter identification.

*On-Line Terrain Parameter Identification Procedure*

The procedure for on-line terrain parameter identification is as follows:

1) While the rover is traveling on nearly flat terrain (as determined through wheel-terrain contact angle estimation (see Section 2.5)) with all wheels rotating at a uniform angular velocity, a single wheel is driven at an angular velocity greater than the others for a short period of time.

2) Simultaneous measurements of the applied motor torque and rover configuration are taken. The wheel sinkage, wheel normal load, and wheel slip are computed as described earlier in this section.

3) The terrain cohesion and internal friction angle are computed as described in Section 2.3.1 using multiple data points collected during the experiment.

Figure 2.9 depicts an illustration of a rover during a terrain identification experiment.
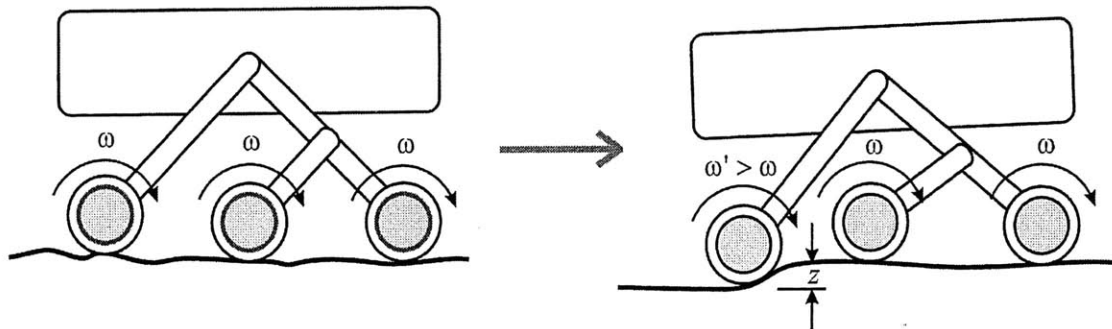


**Figure 2.9**: Illustration of terrain identification experiment

## 2.4 Results—Terrain Identification

Experiments were performed to examine the accuracy of the parameter identification method. Experiments were first performed on the FSRL terrain characterization testbed, which was constructed by Mrs. Sharon Lin (see Figure 2.10). The testbed consists of a driven rigid wheel mounted on an undriven vertical axis. The wheel-axis assembly is mounted to a driven horizontal carriage. By driving the wheel and carriage at different rates, variable slip ratios can be imposed. The vertical load on the wheel can be arbitrarily modified by adding weight to the vertical axis.
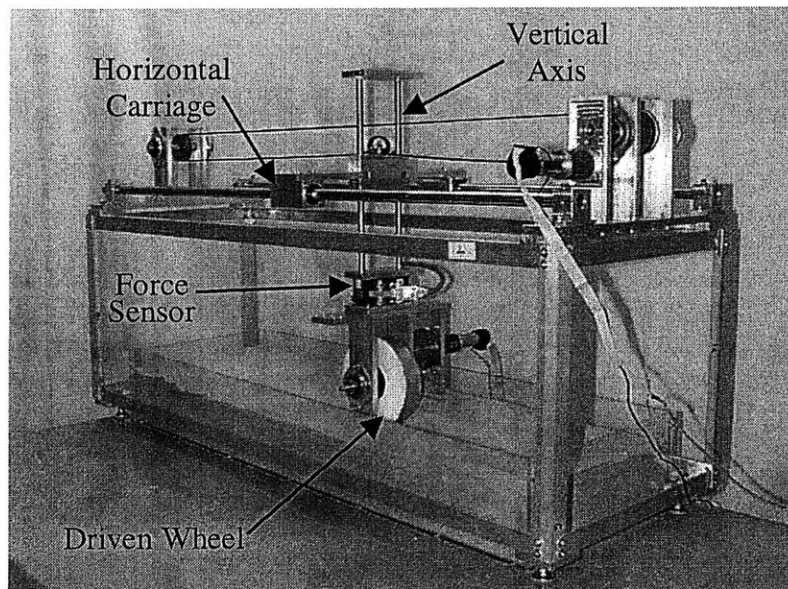


**Figure 2.10**: Field and Space Robotics Laboratory terrain characterization testbed

The testbed is instrumented with encoders to measure angular velocities of both the wheel and the carriage pulley. The carriage linear velocity is computed from the carriage pulley angular velocity. The vertical wheel sinkage is measured with a linear potentiometer. The current input to the wheel is estimated by measuring the voltage across a $3\Omega$ current-sense resistor. The six-component wrench between the wheel and

carriage is measured with an AMTI UFS-4A100-MR6260 six-axis force/torque sensor. The force sensor allows measurement of the normal load $W$ and drawbar pull $DP$.

The wheel diameter and width are 14.6 and 6.0 cm., respectively. The wheel maximum angular velocity is 1.1 rad/sec. This results in a maximum linear velocity of 8.0 cm/sec, which is identical to the maximum carriage velocity. The wheel size and speed were chosen to be similar to current and projected planetary exploration rovers (Hayati, 1996; Schenker, 1997).

Experiments were performed in low-density sandy soil. Sandy soil was chosen as a test medium due to its deformability, and similarity to soil found on Mars by the Pathfinder mission. An experiment was performed by Adam Rzepniewski to characterize the soil using classical terramechanics methods. A device known as a Bevameter was constructed for the purpose of terrain parameter identification (see Figure 2.11). A Bevameter can be used to identify $c$ and $\phi$ by imposing a normal pressure and measuring the maximum soil shear stress (Bekker, 1956). Note that this is an off-line, non-analytical method of terrain identification and is not suitable to on-line characterization.
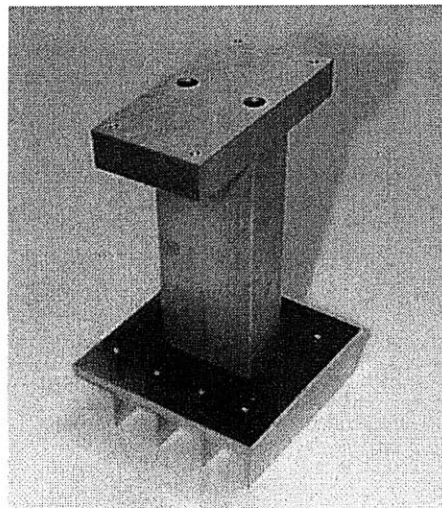


**Figure 2.11**: Bevameter (i.e. BEkker VAlue METER) for soil parameter identification

Results from the identification experiment are shown in Figure 2.12. The experiment

yielded a cohesion of 0.18 kPa and internal shear angle of 29.2°. Sandy soil generally

possesses cohesion in the range of 0.0-0.5 kPa, and internal friction angles $\phi$ in the range

of 25°-32° (Bekker, 1956). Thus the identified parameters were consistent with

published data. They were used as the true soil values for on-line identification
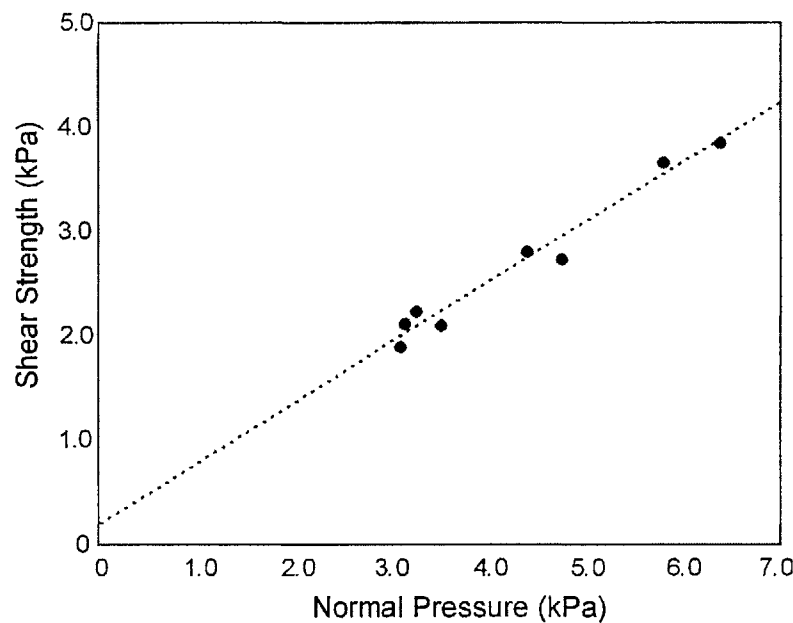
experiments.



**Figure 2.12**: Results of Bevameter identification experiments

On-line identification experiments were first performed on the wheel-terrain testbed.

A measured normal load $W$ was applied to the vertical axis and the wheel was driven with

a constant angular velocity. The input motor torque $T$ was measured and the slip $i$ was

computed from the measured wheel angular velocity and carriage velocity.

Terrain parameters computed from Equations 2.25 and 2.26 during the experiments

were in the range of 0.06-0.10 kPa for cohesion, and 23°-29° for internal friction angle.

This agrees well with both published data for sandy soil and results of the terrain

characterization experiment. A comparison was then made between the measured drawbar pull *DP* and the *DP* computed from Equation A.6. Results for a representative experiment are shown in Figure 2.13. The computed *DP* agrees closely with the measured value. Thus, the thrust for a rigid wheel in sandy terrain can be accurately predicted on the wheel-terrain testbed.
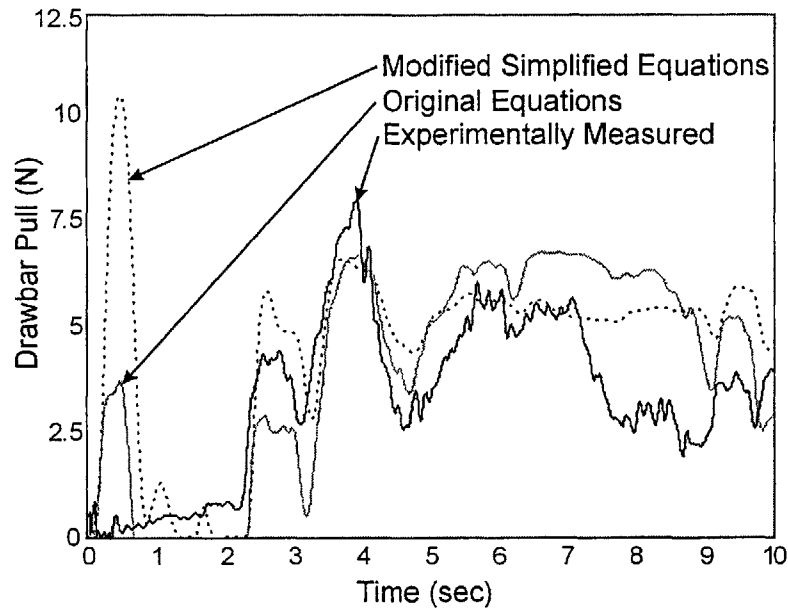


**Figure 2.13**: Comparison of experimentally measured drawbar pull (solid black), predicted drawbar pull using modified simplified equations (dotted black), and predicted drawbar pull using original equations (solid gray)

On-line identification experiments were then performed with the FSRL experimental rover system (see Appendix C). The rover was driven over flat terrain with a nominal wheel angular velocity in the range of 0.1-1.0 rad/sec. The right-rear wheel velocity was increased for a period of 4 seconds, which caused sinkage in the sandy soil. The wheel sinkage, slip, normal load, and torque were computed as described in Section 2.3.2. See Figure 2.14 for a representative sinkage computation result, and Figure 2.15 for a representative wheel slip computation result.
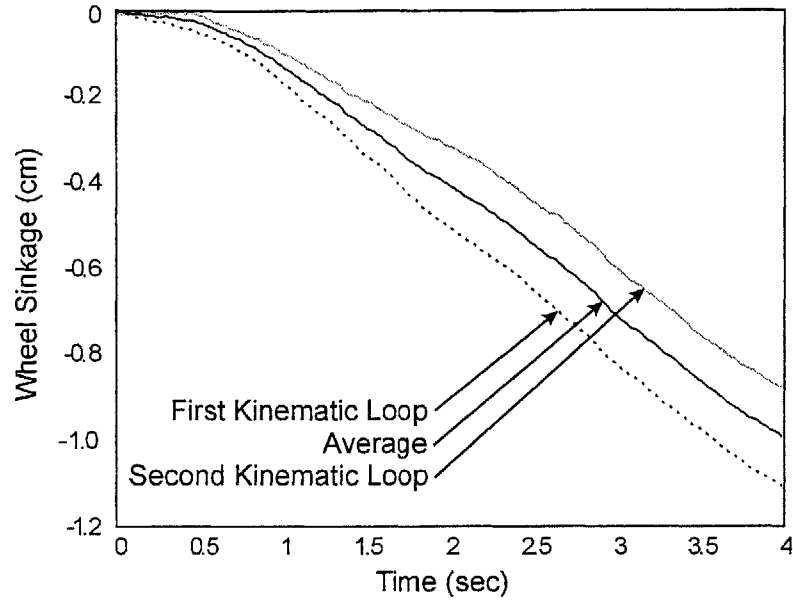
**Figure 2.14**: Averaged sinkage of left-rear FSRL rover wheel (solid black) during soil parameter identification experiment, and sinkage as computed from two different kinematic loops (dotted black and solid gray)
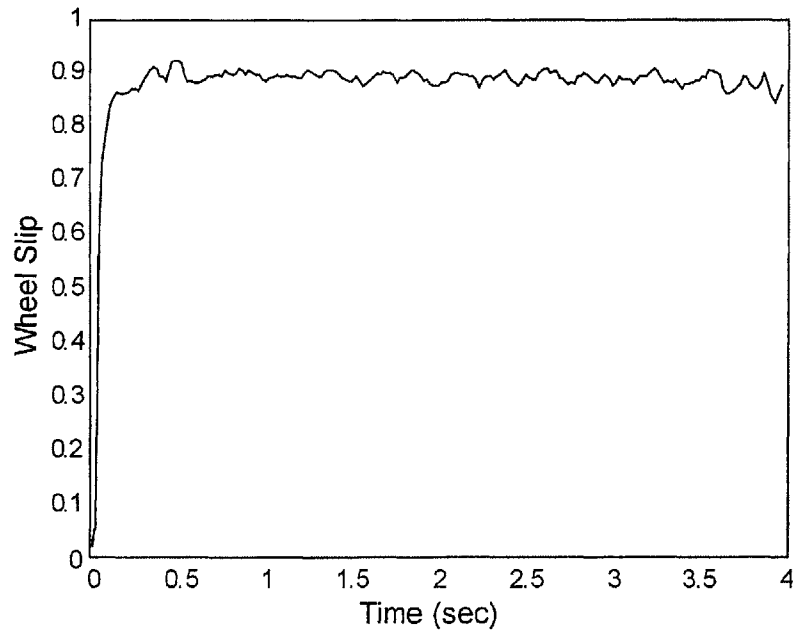


**Figure 2.15**: Wheel slip of left-rear FSRL rover wheel during soil parameter identification experiment

Soil cohesion and internal friction angle were computed during numerous identification experiments. Representative results are shown in Figures 2.16 and 2.17.

After an initial transient the average soil parameters were 0.10-0.55 kPa for cohesion, and 25°-32° for internal friction angle. This agrees well with both published data for sandy soil and the results of both the soil characterization experiment and the soil testbed identification experiment. Thus, it can be concluded that terrain parameters can be accurately estimated on-line during rover motion.
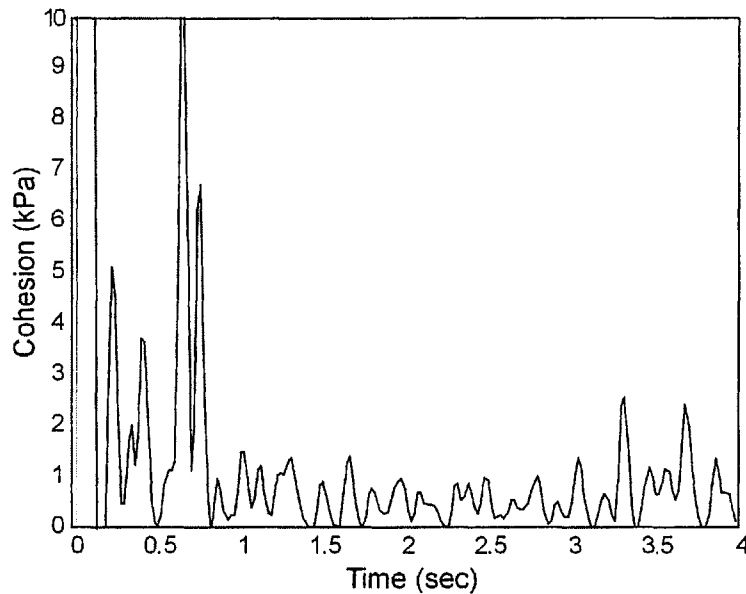


**Figure 2.16**: Estimated soil cohesion $c$ during soil parameter identification experiment
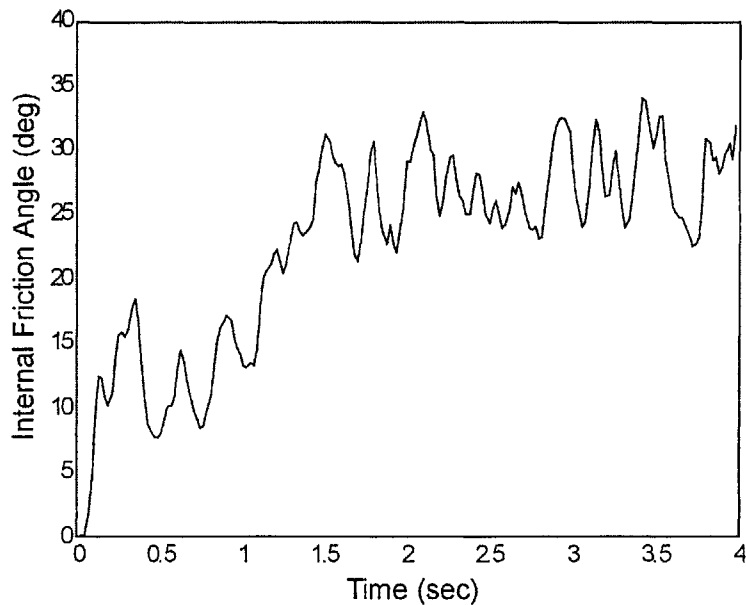


**Figure 2.17**: Estimated friction angle $\phi$ during soil parameter identification experiment

## 2.5 Wheel-Terrain Contact Angle Estimation

Wheel-terrain contact angles greatly influence rover force application properties. For example, a rover traversing flat, even terrain has very different mobility characteristics than one traversing steep, uneven terrain. In this section a method for estimating wheel-terrain contact angles from simple on-board rover sensors is presented. A summary of this work can be found in (Iagnemma and Dubowsky, 2000(a)).

Consider the planar two-wheeled system on uneven terrain shown in Figure 2.18. A planar analysis is appropriate since the rover can neither move nor apply forces in the transverse direction. Thus, transverse contact angles are not considered. In this analysis the terrain is assumed to be rigid, and the wheels are assumed to make contact with the terrain at a point. This is a reasonable assumption for rigid wheels travelling on firm terrain.
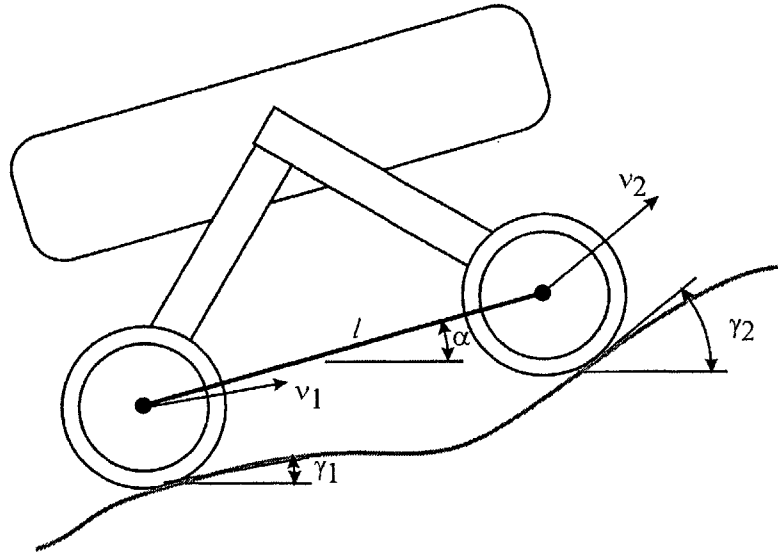


**Figure 2.18**: Planar two-wheeled system on uneven terrain

For rigid wheels travelling on deformable terrain, the single-point assumption no longer holds. However, an "effective" wheel-terrain contact angle is defined as the

angular direction of travel imposed on the wheel by the terrain during motion (see Figure 2.19).
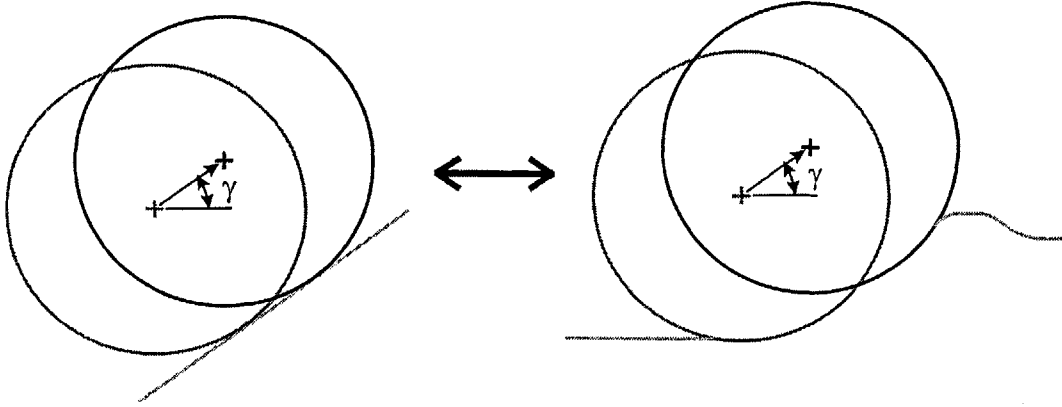


**Figure 2.19**: Wheel-terrain contact angle $\gamma$ for rigid wheel on rigid terrain and equivalent effective wheel-terrain contact angle $\gamma$ for rigid wheel on deformable terrain

In Figure 2.18 the rear and front wheels make contact with the terrain at angles $\gamma_1$ and $\gamma_2$ from the horizontal, respectively. The vehicle pitch, $\alpha$, is also defined with respect to the horizontal. The wheel centers have speeds $v_1$ and $v_2$. These speeds are in a direction parallel to the local wheel-terrain tangent due to the rigid terrain assumption. The distance between the wheel centers is defined by $l$.

For this system, the following kinematic equations can be written:

$$v_1 \cos(\gamma_1 - \alpha) = v_2 \cos(\gamma_2 - \alpha) \qquad (2.29)$$

$$v_2 \sin(\gamma_2 - \alpha) - v_1 \sin(\gamma_1 - \alpha) = l\, \dot{\alpha} \qquad (2.30)$$

Equation (2.29) represents the kinematic constraint that the wheel center length $l$ does not change. Equation (2.30) is a rigid-body kinematic relation between the velocities of the wheel centers and the vehicle pitch rate $\dot{\alpha}$.

Combining Equations (2.29) and (2.30) results in:

$$\sin\left(\gamma_2 - \alpha - (\gamma_{12} - \alpha)\right) = \frac{l\,\dot{\alpha}}{v_1}\cos(\gamma_2 - \alpha) \tag{2.31}$$

With the definitions:

$$\theta \equiv \gamma_2 - \alpha, \quad \beta \equiv \alpha - \gamma_1, \quad a \equiv \frac{l\,\dot{\alpha}}{v_1}, \quad b \equiv \frac{v_2}{v_1}$$

Equations (2.29) and (2.31) become:

$$(b\sin\theta + \sin\beta)\cos\theta = a\cos\theta \tag{2.32}$$

$$\cos\beta = b\cos\theta \tag{2.33}$$

Equations (2.32) and (2.33) can be viewed as the equivalent geometric system shown in Figure 2.20, and can be solved for the wheel-terrain contact angles $\gamma_1$ and $\gamma_2$ as:

$$\gamma_1 = \alpha - \cos^{-1}(h) \tag{2.34}$$

$$\gamma_2 = \cos^{-1}\left(\frac{h}{b}\right) + \alpha \tag{2.35}$$

where:

$$h \equiv \frac{1}{2a}\sqrt{2a^2 + 2b^2 + 2a^2b^2 - a^4 - b^4 - 1}$$
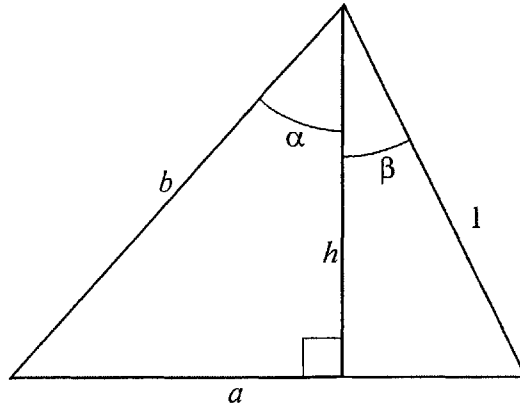


**Figure 2.20**: Equivalent geometric system for Equations (2.32) and (2.33)

There are two special cases that must be considered in this analysis. The first special case occurs when the rover is stationary. In this case Equations (2.32) and (2.33) do not

yield a solution, since if $\dot{\alpha} = v_1 = v_2 = 0$ both $a$ and $b$ are undefined. Physically, the lack of a solution results from the fact that a stationary rover can have an infinite set of possible contact angles at each wheel.

The second special case occurs when $\cos\theta$ equals zero. In this case $\gamma_2 = \pm\pi/2 + \alpha$ from the definition of $\theta$, and Equation (2.34) yields the solution $\gamma_1 = \pm\pi/2 + \alpha$. Physically this corresponds to two possible cases: the rover undergoing pure translation or pure rotation (see Figure 2.21 (a-b)).
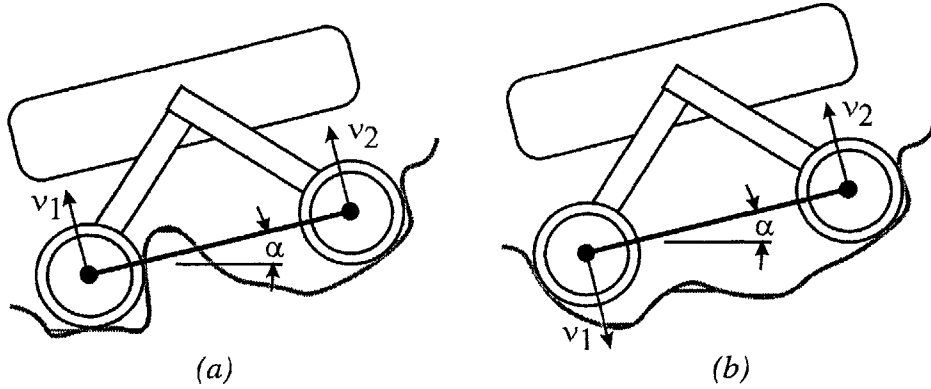


**Figure 2.21**: Physical interpretations of $\cos\theta = 0$: Pure translation (a) and pure rotation (b)

These cases are unlikely to occur in practice. However, both are easily detectable. For the case of pure rotation, $v_1 = -v_2$ and $b = -1$. The solutions for $\gamma_1$ and $\gamma_2$ can be written by inspection as:

$$\gamma_1 = \alpha + \frac{\pi}{2}\text{sgn}(\dot{\alpha}) \tag{2.36}$$

$$\gamma_2 = \alpha - \frac{\pi}{2}\text{sgn}(\dot{\alpha}) \tag{2.37}$$

For the case of pure translation, $\dot{\alpha} = 0$, $v_1 = v_2$ and $b = 1$. This implies that $h$ is undefined and the system of Equations (2.32) and (2.33) has no solution. However, for

low-speed rovers considered in this work, the terrain profile varies slowly with respect to the data sampling rate. This implies that wheel-terrain contact angles computed at a given timestep will be similar to wheel-terrain contact angles computed at the previous timestep. Thus, previously estimated contact angles can be used in situations when a solution to the estimation equations does not exist.

The pitch and pitch rate can be physically measured with rate gyroscopes or inclinometers. The wheel center speeds can be estimated from the wheel angular rate as measured by a tachometer. Thus, wheel-terrain contact angles can be estimated with common, low-cost on-board sensors. The estimation process is computationally simple, and thus suitable for on-board implementation.

### 2.5.1 Extended Kalman Filter Implementation

In the previous section it was shown that the wheel-terrain contact angles could be computed from simple, measurable quantities. However, sensor noise will degrade these measurements, and wheel slip will further corrupt the estimate. In this section an extended Kalman filter (EKF) is developed to compensate for these effects.

An extended Kalman filter is an effective framework for fusing data from multiple noisy sensor measurements to estimate the state of a nonlinear system (Brown, 1997; Welch and Bishop, 1999). In an EKF the process and sensor signal noise are assumed to be unbiased Gaussian white noise with known covariance. These are reasonable assumptions for the signals considered in this work, such as wheel tachometers, gyroscopes, and inclinometers. A description of standard EKF equations are presented in Appendix D.

For wheel-terrain contact angle estimation, the EKF computes a minimum mean square estimate of the state vector $\mathbf{x} = \begin{bmatrix} \alpha & \dot{\alpha} & v_1 & v_2 & \gamma_1 & \gamma_2 \end{bmatrix}^T$. Inputs to the EKF are the system matrix $\mathbf{F}$, measurement matrix $\mathbf{H}$, process and measurement error covariance matrices $\mathbf{Q}$ and $\mathbf{R}$, respectively, and an initial state and covariance estimate (see Appendix D). The EKF measurement vector is defined as $\mathbf{z} = \begin{bmatrix} \alpha & v_1 & v_2 \end{bmatrix}^T$ since vehicle pitch $\alpha$ can be measured, and the wheel center speeds $v_1$ and $v_2$ can be approximated from knowledge of the wheel angular velocities and radii. Measurements are taken at every time step during vehicle motion.

The system and measurement matrices are computed from the system kinematic equations. The measurement error covariance matrix $\mathbf{R}$ is assumed to be diagonal, and the elements of $\mathbf{R}$ corresponding to vehicle pitch and wheel center speed can be estimated via off-line measurement of the sensor noise. The elements of $\mathbf{R}$ corresponding to unmeasured quantities, such as the wheel-terrain contact angles, can be computed by linearizing Equations (2.32) and (2.33) and summing the contributions of the measured noise terms. The process error covariance matrix $\mathbf{Q}$ is assumed to be diagonal, and its elements are computed from estimates of the error inherent in the basic wheel-terrain contact angle estimation process (e.g. error in the assumed values of system kinematic parameters such as wheel radius).

Computation of the EKF involves several matrix inverse operations. Note, however, that the matrices involved are generally near-diagonal. Efficient inversion techniques can be used to reduce computational burden (Duff *et al.*, 1986). Thus, EKF computation remains efficient and suitable for on-board mobile robot implementation.

---

## 2.6    Results—Wheel-Terrain Contact Angle Identification

Simulations and experimental trials of the wheel-terrain contact angle estimation algorithm were conducted on the FSRL rover testbed. These results are presented below.

### 2.6.1    Simulation Results

A simulation was performed to characterize the accuracy of wheel-terrain contact angle estimation in the presence of noisy sensor signals. The simulated system is a planar, two-wheeled vehicle traversing undulating terrain shown in Figure 2.22. The pitch $\alpha$ was corrupted with white noise of standard deviation $3°$. This is approximately 10% of its range of values experienced during the simulation. The pitch rate $\dot{\alpha}$ was computed from $\alpha$. The rear and front wheel velocities, $v_1$ and $v_2$, were corrupted with white noise of standard deviation 0.05 cm/sec, which represents approximately 10% of their range of values experienced during the simulation. This simulates error due to effects of wheel slip and tachometer noise. In this simulation the wheel spacing distance $l$ was 1 m.
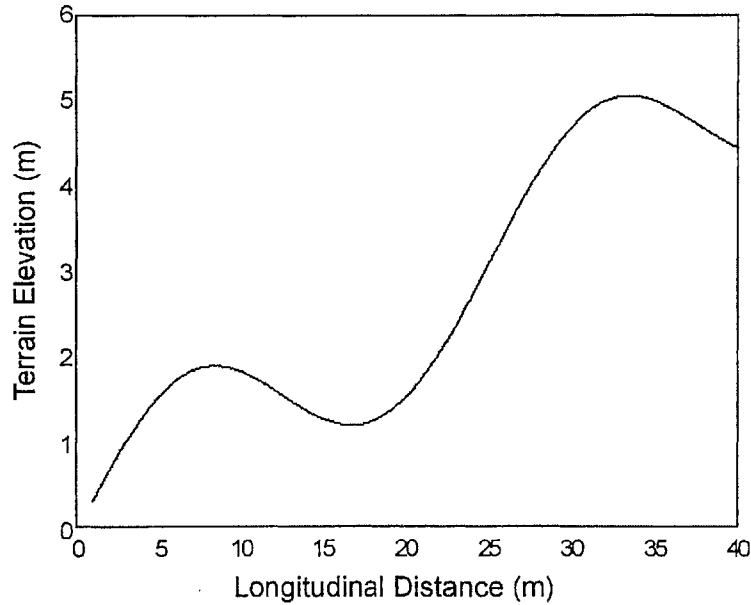


**Figure 2.22**: Simulated undulating terrain profile

---

The EKF measurement covariance matrix **R** was chosen based on the simulated sensor noise levels. The measurement covariances were chosen to be 150% of the simulated sensor noise levels in an attempt to emulate conservative human modeling of a physical rover system. The EKF process noise matrix **Q** was chosen based on expected uncertainty sources such as wheel slip. Note that in practice, covariance estimates could be determined *a priori* from off-line characterization of the physical sensors.

Results of the contact angle estimation simulation are shown in Figure 2.23. The EKF estimate is compared to an unfiltered computation (i.e. direct calculation from Equations (2.32) and (2.33)), and the true contact angle values. After an initial transient, the EKF estimate of the terrain contact angle is very accurate, with RMS errors of 0.98° and 1.32° for the front and rear contact angles, respectively. Error increases at flat terrain regions (i.e. where the values of front and rear contact angles are identical) since the angle estimation equations become poorly conditioned due to reasons discussed previously. In general, the EKF does an excellent job of estimating wheel-terrain contact angles in the presence of noise.
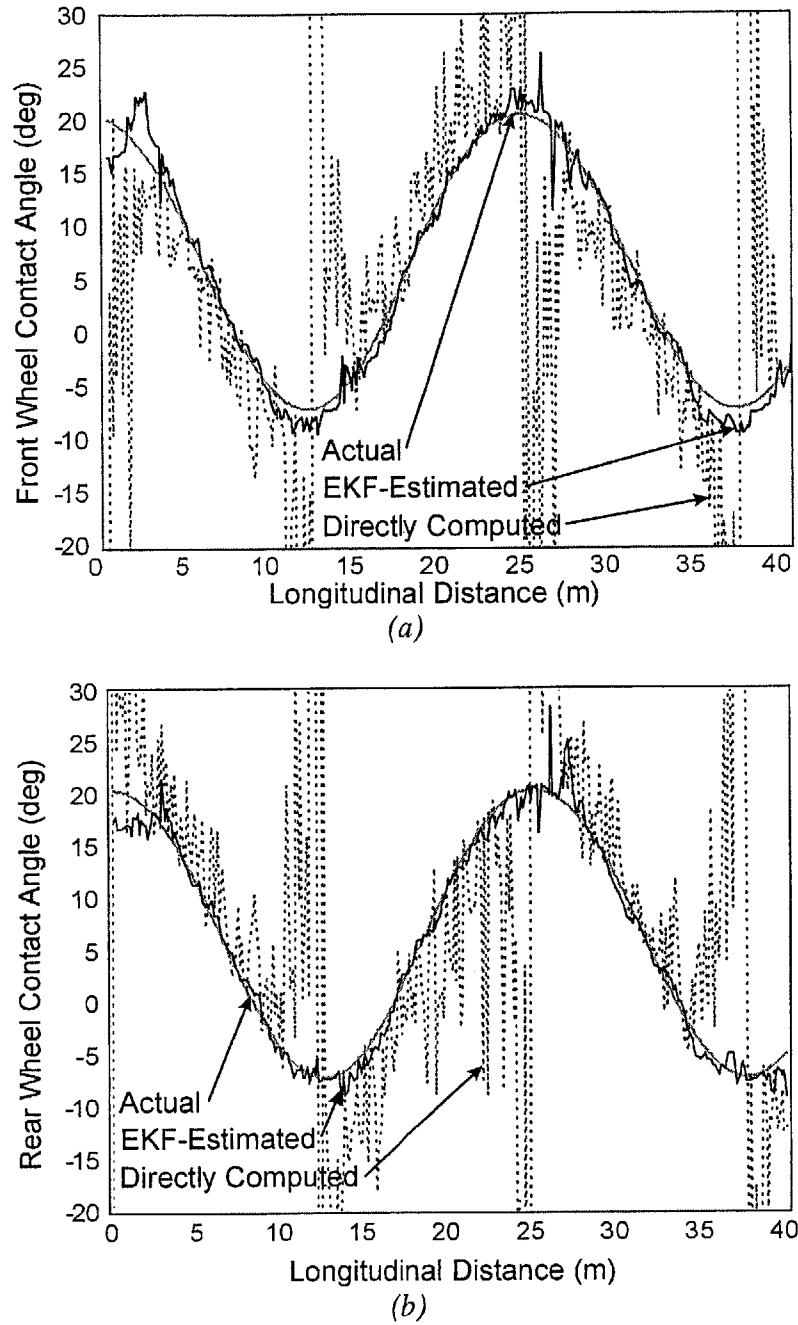
**Figure 2.23**: EKF-estimated (solid black), directly computed (dashed black), and actual (solid gray) wheel-terrain contact angles for front (a) and rear (b) wheels

## 2.6.2 Experimental Results

The EKF-based contact angle estimation algorithm was implemented on the FSRL

laboratory six-wheeled rover (see Appendix C). For this type of rocker-bogie vehicle

suspension, the contact angles for the front and middle wheels can be directly estimated with Equations (2.32) and (2.33). The rear wheel does not maintain a fixed distance from either the front or middle wheel. However, it does maintain a fixed distance to the bogey free-pivot joint and can thus be estimated from Equations (2.32) and (2.33) with $l$ taken as the distance from the rear wheel center to the center of the bogey free-pivot joint.

Measurement noise covariances for the EKF were estimated off-line by analyzing the standard deviation of sensor readings for the wheel tachometers and joint potentiometers during a trial motion. Process noise covariances were estimated based on results from the simulation.

Two experiments were performed. In the first experiment the rover was driven over a rock of approximately one-half wheel diameter in size. The wheel-terrain contact angles were estimated using the EKF framework described above.

Results of this experiment can be seen in Figure 2.24. The wheel-terrain contact angles increase as the wheel ascends the rock, decrease to zero atop the rock, and become negative as the wheel descends the rock. As expected, the contact angle estimates are similar for all three wheels.
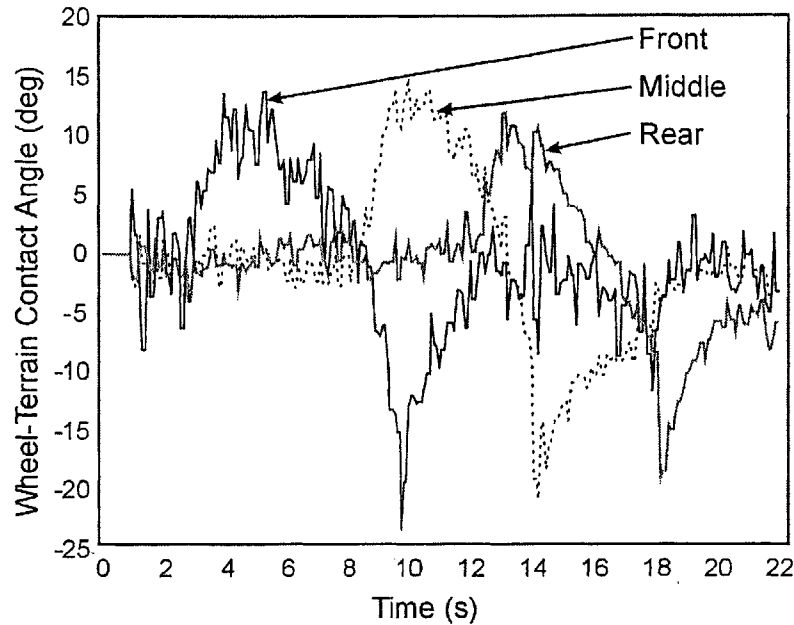
**Figure 2.24**: EKF-estimated wheel-terrain contact angle of FSRL rover traversing a rock: Front wheel (black solid), middle wheel (black dotted), and rear wheel (gray solid)

In the second experiment the rover was driven from flat terrain up a 20° incline, and the front and middle wheel-terrain contact angles were estimated (see Figure 2.25). The goal of this experiment was to obtain a quantifiable measure of wheel-terrain contact angle estimation accuracy.
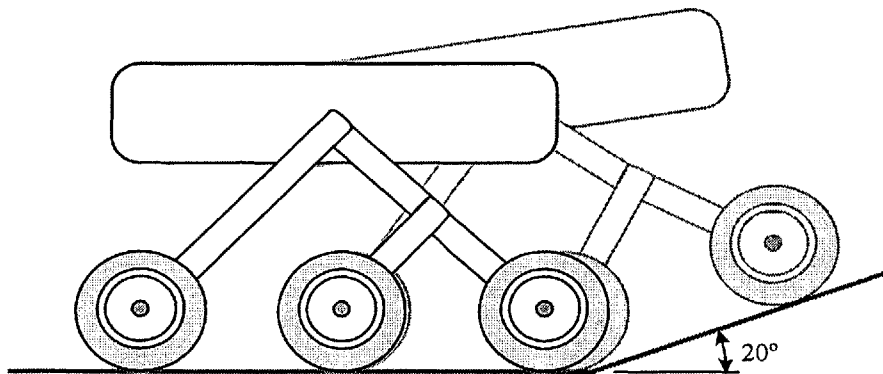


**Figure 2.25**: Rover traversing 20° incline

Results of this experiment can be seen in Figure 2.26. The RMS error of the front wheel contact angle estimate is 2.21° while the middle wheel RMS error is 1.84°.

Average computation time for both experiments was 0.6 msec/cycle, which is reasonable for on-board implementation. Thus it can be concluded that wheel-terrain contact angles can be accurately estimated on-line by a rover with noisy sensors and limited computational resources.
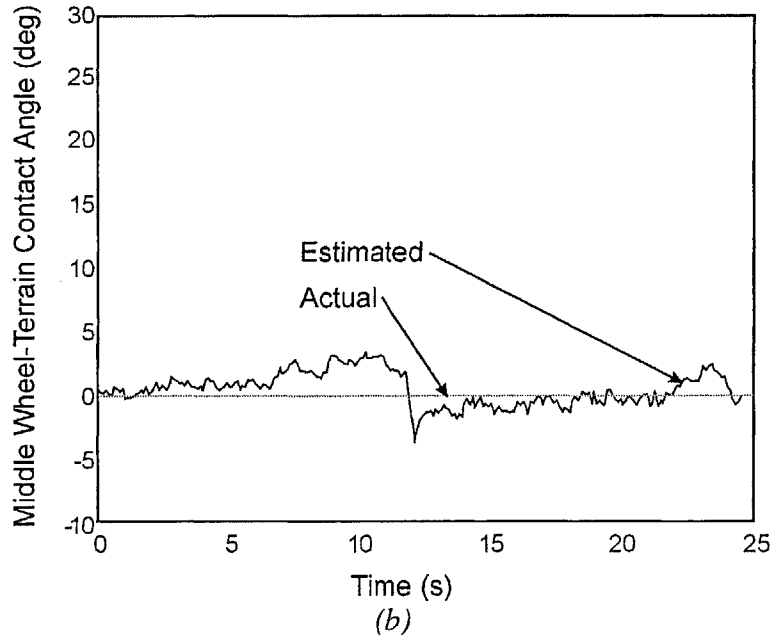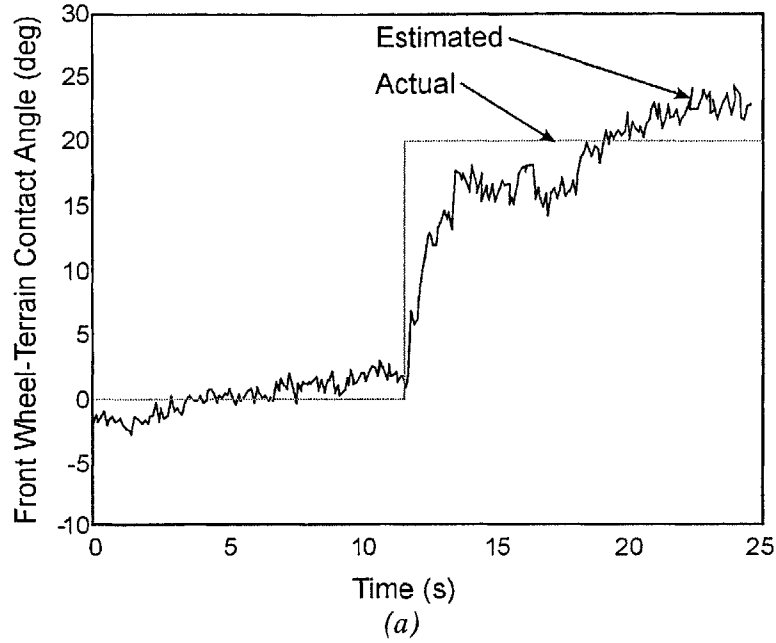


Figure 2.26: EKF-estimated (black) and actual (gray) experimental results of FSRL rover traversing 20° incline for front (a) and middle (b) wheels

## 2.7 Summary and Conclusions

This chapter has presented a set of physical models of rovers and terrain, with a goal of answering the question "What can a rover do?"

Kinematic and force analyses of a six-wheeled rover were briefly discussed. A method of characterizing important terrain parameters and estimating these parameters on-line was presented. A key aspect of this method is the simplification of fundamental equations to allow symbolic manipulation. Simulation and experimental results show that critical parameters of sandy soil can be estimated with good accuracy.

A wheel-terrain contact angle estimation algorithm based on rigid-body kinematic equations was presented. The algorithm utilizes an extended Kalman filter to fuse on-board sensor signals. Simulation and experimental results for a six-wheeled rover have shown that the algorithm can accurately estimate wheel-terrain contact angles in rough terrain.

# Chapter

# 3

# Rough-Terrain Planning:
# What Should a Rover Do?

## 3.1  Introduction

This chapter presents two rough-terrain motion planning methods.  Section 3.2 describes a method to finds safe, short paths from the rover's current position to a distant goal position.  Section 3.3 presents simulation results for the motion planning method, and shows that it finds safe, direct paths through rough terrain compared to a traditional planning method.  Section 3.4 presents a planning method for kinematically reconfigurable rovers that optimizes the rover's physical structure to improve tipover stability.  Section 3.5 presents simulation and experimental results for the kinematic reconfiguration method, and shows that it greatly improves rough terrain tipover stability.

## 3.2  Rough-Terrain Planning

In future planetary exploration missions, rovers will be required to obtain 3D terrain range data, identify a scientific goal, and autonomously plan a path to the goal through

rough terrain. In this section a planning method is presented that employs a non-binary obstacle representation, considers range data and rover localization uncertainty, and utilizes detailed physical models of the rover and its environment to assess path traversability. A summary of this work can be found in (Iagnemma *et al.*, 1999(a)).

The input to the planning method is a 3D terrain range map, obtainable from a laser rangefinder or stereo camera pair. The assumed range of this data is approximately 5-10 rover lengths.

The method is composed of two steps (see Figure 3.1). The first step is a rapid search through the terrain map for a candidate path, and is described in Section 3.2.1. The rapid path search uses a measure of local terrain roughness and a classical $A*$ graph search algorithm to quickly find a "reasonable" path through the range map from the rover start position to the goal position (Nilsson, 1980). Terrain roughness is defined with respect to rover physical parameters such as wheel diameter.
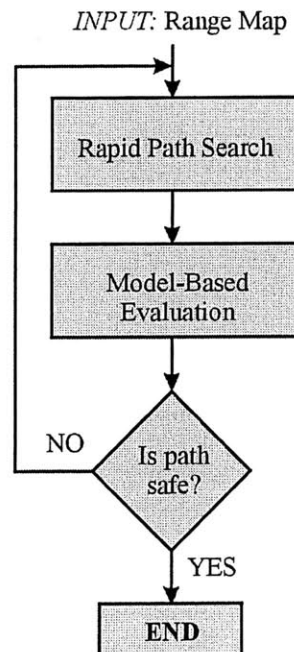


**Figure 3.1:** Simplified flowchart of the planning algorithm

The second step is a rigorous evaluation of the proposed path using rover and terrain physical models, and is described in Section 3.2.2. Uncertainty in terrain measurement and rover localization are considered. If the model-based evaluation determines that the rover could be subject to failure along the proposed path, the $A^*$ cost function is increased at the potential failure location, and the path is replanned to avoid the hazard.

### 3.2.1 Step One: Rapid Path Search

The purpose of the rapid path search is to quickly find a direct, reasonable path from the current rover position to the goal position. In the interest of reducing computation time for on-board implementation, the rapid search is not a globally optimal search. The input to the search is a 3D terrain range map, such as would be obtainable from a laser rangefinder or stereo camera pair. The terrain is represented as a map of elevations $z$ associated with a grid in $(x,y)$ (see Figure 3.2).
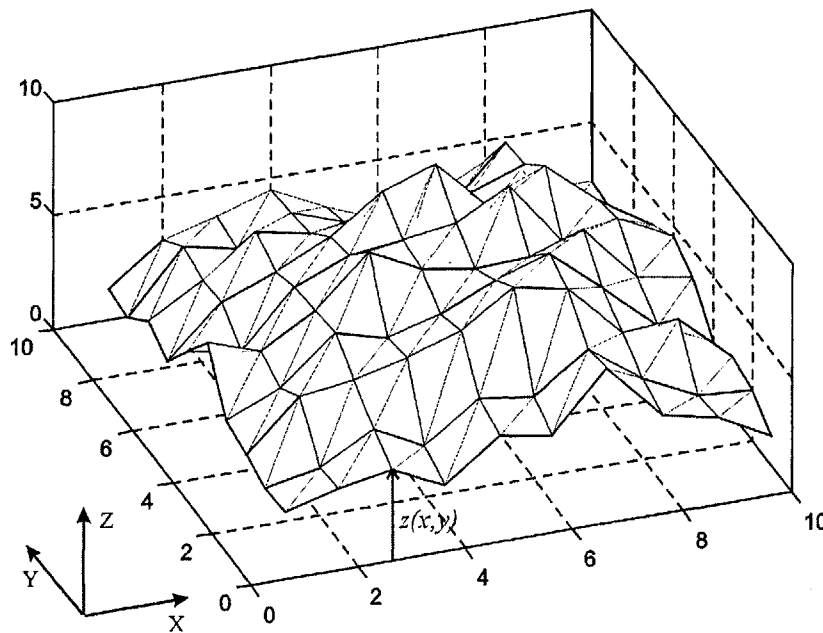


**Figure 3.2:** Example of terrain data input to rapid path search

An $A^*$ algorithm is used to rapidly find a path through the terrain grid from the current rover position to the goal position (Nilsson, 1980). The $A^*$ algorithm is a graph-search technique, and is attractive due to its optimality and high speed for relatively small graphs. In this work, the assumed graph size is approximately $10^4$ cells. The $A^*$ algorithm computes an optimal path based on a user-defined performance index, $\Phi$.

*Performance Index Definition*

The performance index is formulated as a function of three variables. Terrain roughness, $r$, is considered since it is directly related to traversability and rover safety (Bekker, 1969). Rover turning action, $t$, is considered, since in rough terrain excessive turning may not be desirable or possible. Path length, $l$, is considered in order to minimize energy expenditure. Since the performance index must be evaluated a large number of times, it should be mathematically simple to speed computation.

Terrain roughness can be defined in numerous ways. Here a roughness definition is proposed based on the statistical variance of the terrain elevation. Consider a rover centered at a point *(x,y)* and oriented in the direction of motion along a proposed path. Let $\mathfrak{R}$ be the set of terrain elevation points inside the convex hull defined by the wheel-terrain contact points of the rover on flat ground, as shown in Figure 3.3. The terrain roughness $r$ at *(x,y)* is defined as the root of the variance of all elevation points in $\mathfrak{R}$:

$$r(x, y) = \sqrt{\mathrm{var}(z(\mathfrak{R}))} \tag{3.1}$$

with the root taken to preserve dimensional consistency within the performance index.

Note that it is important to include "interior" terrain points (i.e. inside the rover footprint) in order to provide an estimate of potential rover hang-up failure (Bekker,

1969). Hang-up failure occurs when the rover body becomes lodged atop an obstacle, causing loss of wheel traction and rover entrapment.
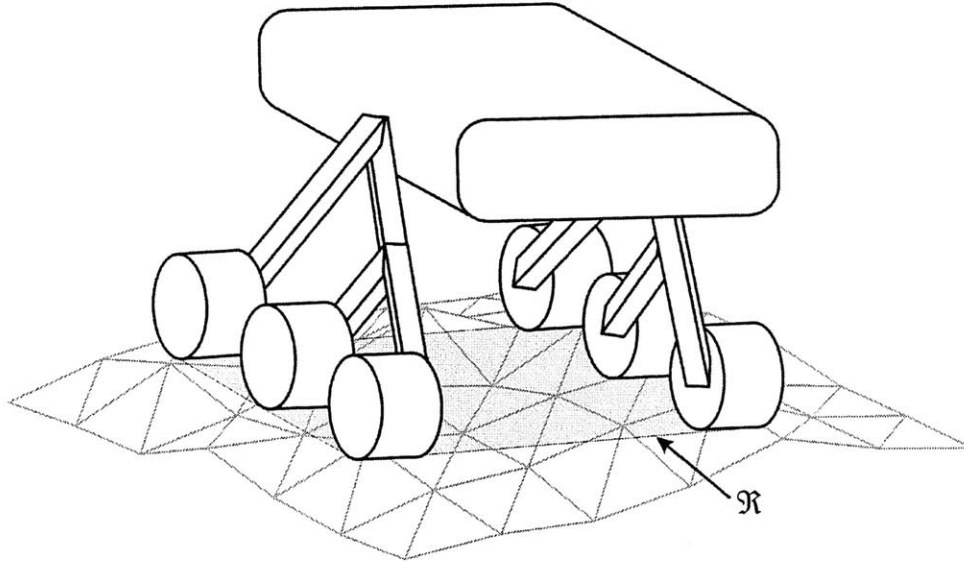


**Figure 3.3:** Terrain roughness definition

Clearly, terrain with extremely large roughness $r$ relative to the rover size is untraversable. Although there is no notion of a discrete "obstacles" in the planning method, it is desirable to assign high cost to these terrain regions. To accomplish this a modified roughness measure $r'$ is defined, as:

$$r'(x, y) = \left(\frac{r}{d}\right)^{\alpha} \tag{3.2}$$

where $d$ is the rover wheel diameter, and $\alpha$ is a positive constant. This has the effect of increasingly penalizing terrain regions that are clearly untraversable, while maintaining a continuous (as opposed to binary) terrain representation.

The cost, $t$, associated with rover turning assumes that skid steering is utilized as the turning mode. On flat terrain, skid steering allows point turns. In rough terrain, however, it may not be possible to skid-steer due to high terrain-induced transverse forces. A cost

is assigned proportional to terrain roughness, at points where the proposed path changes heading. The turning cost function $t$ is defined as:

$$t(x,y) = \left( \frac{\sqrt{\mathrm{var}(z(\mathfrak{R}'))}}{d} \right)^{\alpha}$$  (3.3)

where $\mathfrak{R}'$ is defined as the set of points inside a circle centered at $(x,y)$ with radius equal to the distance from the rover center to the most distant wheel-terrain contact point. Thus, $\mathfrak{R}'$ can be viewed as a superset of $\mathfrak{R}$ augmented to include the area swept during turning. The wheel diameter is again utilized for scaling and non-dimensionalizing the cost function.

The cost, $l$, associated with path length is simply taken as the proposed path length $L$ divided by a rover characteristic length, such as the wheel diameter, for dimensional consistency:

$$l(x,y) = \frac{L}{d}$$  (3.4)

The final performance index $\Phi$ is formed as a weighted sum of the functions considering terrain unevenness, turning, and path length:

$$\Phi = k_1 r' + k_2 t + k_3 l$$  (3.5)

with constants $k_1$, $k_2$, and $k_3$ chosen to adjust the relative values of $r'$, $t$, and $l$ to address mission-specific constraints.

A least-cost path $P$ is found from the current rover position to the goal position using the $A^*$ algorithm. The path $P$ is composed of $n$ neighboring $(x,y)$ pairs, $P = \{x_1 \ y_1,...,x_n \ y_n\}$, and combines terrain smoothness, minimum turning requirement, and short distance. The path is not guaranteed to be hazard-free, due to the simple heuristic nature of the

performance index. Again, the performance index was selected due to its ease of evaluation and intuitive relationship to rover mobility. It is intended to rapidly lead to a reasonable path through the terrain.

### 3.2.2 Step Two: Model-Based Evaluation

The path generated by the rapid search is not guaranteed to be hazard-free, since it is based on a simple, heuristic performance index. A model-based evaluation of the proposed path is required to ensure rover safety.

To perform the model-based evaluation, the rover configuration is first computed at each $(x,y)$ pair in $P$, as described in Section 2.2.1. The model-based evaluation is then composed of a stability analysis, kinematic analysis, and force analysis at each configuration corresponding to an $(x,y)$ pair in $P$.

*Stability Analysis*

With the rover configuration known, stability is computed in a manner similar to that proposed by (Papadopoulos and Rey, 1996). This definition is briefly reviewed here.

For a general mobile robot, $m$ wheel-terrain contact points $\mathbf{p}_i$, $i=\{1,...,m\}$ are numbered in ascending order in a clockwise manner when viewed from above (see Figure 3.4). Note that all vectors in this analysis are expressed in the inertial frame $\{XYZ\}$. The lines joining the wheel-terrain contact points are referred to as tipover axes and denoted $\mathbf{a}_i$, where the $i^{th}$ tipover axis is given by:

$$\mathbf{a}_i = \mathbf{p}_{i+1} - \mathbf{p}_i, \quad i = \{1,...,m\text{-}1\} \tag{3.6}$$

$$\mathbf{a}_m = \mathbf{p}_1 - \mathbf{p}_m \tag{3.7}$$

Clearly, a vehicle with $m$ wheels or feet in contact with the terrain has in general $m$ tipover axes. Tipover axis normals $\mathbf{l}_i$ that intersect the center of mass can be described as:

$$\mathbf{l}_i = \left(\mathbf{1} - \hat{\mathbf{a}}_i \hat{\mathbf{a}}_i^T\right)\mathbf{p}_{i+1} \tag{3.8}$$

where $\hat{\mathbf{a}} = \mathbf{a}/\|\mathbf{a}\|$.
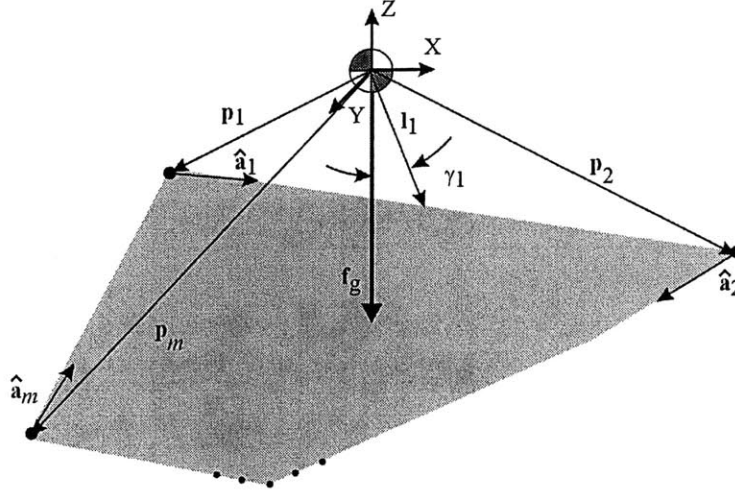


**Figure 3.4:** Stability definition diagram

Stability angles can be computed for each tipover axis as the angle between the gravitational force vector $\mathbf{f}_g$ and the axis normal $\mathbf{l}_i$:

$$\gamma_i = \sigma_i \cos^{-1}\left(\hat{\mathbf{f}}_g \cdot \hat{\mathbf{l}}_i\right), \quad i = \{1,\ldots,m\} \tag{3.9}$$

with

$$\sigma_i = \begin{cases} +1, & \left(\hat{\mathbf{l}}_i \times \hat{\mathbf{f}}_g\right) \cdot \hat{\mathbf{a}}_i < 0 \\ -1, & \text{otherwise} \end{cases} \tag{3.10}$$

The overall vehicle stability angle is defined as the minimum of the $m$ stability angles:

$$\alpha = \min(\gamma_i), \quad i = \{1,\ldots,m\} \tag{3.11}$$

When $\alpha \leq 0$ a tipover instability is occurring. Thus, a point in $P$ is deemed a failure

point if $\alpha < \alpha_{min}$, where $\alpha_{min}$ is a positive constant that can be viewed as a safety margin.

*Kinematic Analysis*

To verify that a rover configuration is kinematically valid (i.e. that no joint-limit or

interference constraints are violated), at each point along the path the rover joint values

are required to satisfy an inequality constraint:

$$\theta_i^{min} < \theta_i < \theta_i^{max} , \quad i = \{1,...,q\}$$ (3.12)

where $\theta_i^{min}$ and $\theta_i^{max}$ can be functions of the rover configuration, and $q$ is the number of

rover suspension joints. If the inequality constraint is violated for any joint the point is

deemed a failure point and the cost associated with the point is increased.

*Force Analysis*

A quasi-static force analysis is performed at each point along the path, as described in

Section 2.2.2 and Appendix A. The input force $f_s$ to the force analysis is composed of a

small positive constant in the direction of rover motion along the path. Thus, if a solution

to the force analysis exists, the rover can generate enough force to cause motion in the

desired direction. If the analysis predicts that the rover cannot move in the desired

direction, the point is deemed a failure point and the cost associated with the failure point

is increased.

If no stability, kinematic validity, or force validity constraints are violated, the

proposed path $P$ is deemed safe.

### 3.2.3 Uncertainty in Rough-Terrain Planning

There are numerous sources of uncertainty associated with rough-terrain planning. If uncertainty is not explicitly considered in the planning method, rover instability or entrapment may result. The primary quantifiable sources of uncertainty lie in the measurement of terrain location data points, and rover localization. In this section models of these uncertainty sources are presented.

*Terrain Measurement Uncertainty*

Terrain location as measured by laser-based and stereo-camera range sensors is subject to significant error (Hebert and Krotkov, 1992; Matthies and Grandjean, 1994; Matthies *et al.*, 1995). This error can be decomposed into a random, noise-based component, and a systematic component due to sensor bias and miscalibration (Matthies and Grandjean, 1994).

The random component of sensor error is dominated by noise. For stereo camera ranging systems, it has been shown to be approximately gaussian in nature, and a quadratic function of range:

$$\sigma_Z = \sigma_r Z^2 \tag{3.13}$$

where $Z$ is the distance from the sensor to the terrain point of interest, and $\sigma_r$ is the standard deviation of the sensor noise. Note that $\sigma_r$ can be characterized off-line through standard calibration techniques (Matthies and Grandjean, 1994).

The systematic component of sensor error is dominated by miscalibration. It has been shown to be a linear function of range (Matthies *et al.*, 1995):

$$\sigma_Z = K_s Z \tag{3.14}$$

where $K_s$ can be identified off-line through standard calibration techniques. This error can be viewed physically as the angular displacement of the true sensor location from the assumed location.

Thus, uncertainty in terrain measurement can be modeled as the sum of a random and systematic component, as:

$$\sigma_Z = Z(\sigma_r Z + K_s) \qquad (3.15)$$

In general the uncertainty increases with range distance and can be characterized off-line.

*Rover Localization Uncertainty*

Localization refers to estimation of the rover's position and orientation with respect to a fixed reference frame (Borenstein *et al.*, 1996). The most common method of localization is dead reckoning based on wheel odometry information. In general there is uncertainty associated with this type of localization due to wheel slip and sensor noise (Matthies *et al.*, 1995).

This error has been studied and characterized for numerous planetary exploration rovers (Matthies *et al.*, 1995; Volpe, 1999). In general a linear error relation has been observed in both the estimated distance traveled and the estimated change in heading during turns:

$$\sigma_L^{pos} = K_{pos}d \qquad (3.16)$$

$$\sigma_L^{head} = K_{head}\Delta \qquad (3.17)$$

where $d$ is the linear distance traveled, $\Delta$ is the angular change in heading, and $K_{pos}$ and $K_{head}$ are constants. These constants can be identified experimentally off-line via empirical analysis.

Note that uncertainty in advanced localization techniques has also been studied and characterized (Vlassis and Tsanakas, 1998). However, in this thesis dead reckoning is considered, as it is the expected localization technique for planetary exploration vehicles.

### 3.2.4. Incorporating Uncertainty in the Rapid Path Search

Uncertainty is considered in both the rapid path search and model-based evaluation. In this section, methods for incorporating the terrain measurement and localization uncertainty models into the rapid path search are described.

*Terrain Measurement Uncertainty*

The rapid path search does not consider rover physics, but only the terrain characteristics. Thus, it is important to consider terrain measurement uncertainty in the rapid search.

Terrain measurement uncertainty threatens path safety, as it implies a misrepresentation of terrain feature placement. For example, the range sensor could misreport the position of a large boulder, and the planning algorithm could propose a path that intersects the boulder. Thus it is important to introduce some notion of a "safety margin" into the algorithm to account for terrain location uncertainty. This is accomplished by pre-filtering the terrain range map with a two-dimensional gaussian filter:

$$z'(x, y) = \frac{e^{-\frac{x_r^2 + y_r^2}{2\sigma_z^2}}}{\sigma_z \sqrt{2\pi}}$$
(3.18)

where the standard deviation $\sigma_z$ of the filter is defined by Equation (3.15) and $x_r$ and $y_r$ refer to the $x$ and $y$ distance, respectively, from the rover to the terrain point. Note that this filter is applied in discrete form on a window of approximately twice $\sigma_z$.

The filter has the effect of "blurring" the terrain. This can be observed in Figure 3.5, a comparison of filtered and unfiltered simulated range data of a large discrete obstacle. The filtered range map has an enlarged area of uneven terrain compared to the unfiltered map, and thus the cost associated with terrain roughness extends further from the filtered obstacle. The rapid path search will plan a path that is further from the potential obstacle, imputing a safety margin to the proposed path.



*(a)*                    *(b)*
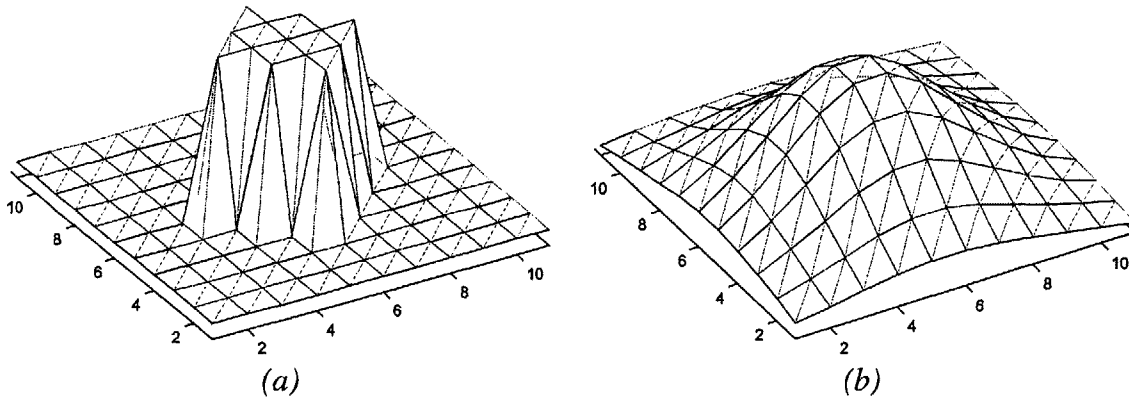
**Figure 3.5**: Terrain data before (a) and after (b) gaussian filter

Localization uncertainty is not explicitly considered in the rapid path search. It is considered in the model-based evaluation, which is discussed below.

### 3.2.5. Incorporating Uncertainty in the Model-Based Evaluation

The model-based evaluation verifies rover stability and force validity at discrete points along the proposed path. However, the model-based evaluation must account for imperfect knowledge of the terrain, and the fact that the rover may not accurately follow the proposed path due to localization error.

*Terrain Measurement Uncertainty*

Uncertainty in terrain measurement affects the model-based evaluation by creating ambiguity in the true rover configuration at a given terrain point. This affects computation of stability, kinematic validity, and force state. To conservatively assess path safety, the potential worst-case rover configurations must be examined.

Potential worst-case configurations exist at the possible terrain point location boundaries. The extreme possible elevations of a given terrain point $z_n$ can be computed from Equation (3.15), as:

$$z_n^+ = z_n + \sigma_z, \quad z_n^- = z_n - \sigma_z \tag{3.19}$$

where the worst-case rover configurations are assumed to lie on the extreme elevation changes. This assumption is made to speed computation.

A set of $m$ potential worst-case rover configurations $Q' = \{Q_1,...,Q_m\}$ are computed by solving the inverse kinematic solution of the rover at each unique terrain point combination (see Figure 3.6). Thus for an $n$-wheeled rover, the number of rover configurations in $Q'$ is $m = 2^n$. Note that for simplicity the location pairs are taken as deviations in the $z$ direction from the nominal configuration. This may not represent the

true worst-case kinematic configuration, but again is taken as a rapid approximation to speed computation.
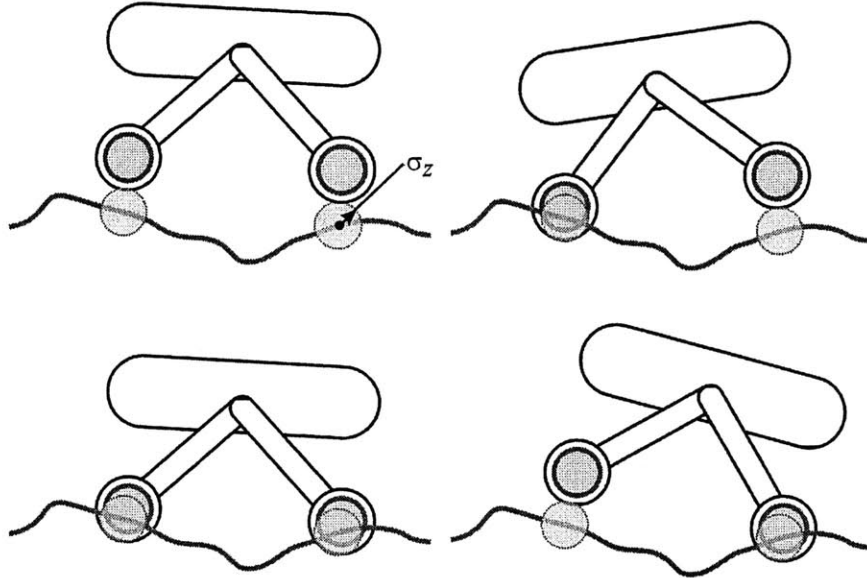


**Figure 3.6:** Set of possible planar configurations for a two-wheeled rover

Although sophisticated techniques exist for dealing with uncertainty propagation, due to the relatively small number of potential configurations a brute-force analysis is appropriate (Latombe, 1991; Page and Sanderson, 1995; Zhang *et al.*, 1998). Thus, each configuration in $Q'$ is examined for stability, kinematic validity, and force validity as described in Section 3.2.2. If the configuration is deemed unsafe, the point is deemed a failure point and the cost associated with the failure point is increased. The rapid path search is then called to re-plan the path.

Note that from Equation (3.15), terrain measurement uncertainty increases as range distance increases. Clearly, at some finite distance the uncertainty will increase to a point where no kinematically valid rover configuration can be found. This places an upper bound on the range of the planning algorithm independent of the maximum sensing distance of the range sensor.

Uncertainty in rover localization affects the model-based evaluation by increasing the number of possible configurations a rover may experience during execution of the proposed path. That is, given a path $P$ from the rapid path search, a superset $P'$ of $P$ can be formed by including all points near $P$ within a distance proportional to the rover localization uncertainty (see Figure 3.7).

All points in $P'$ are examined for stability, kinematic validity, and force validity as described in Section 3.2.2. If any configurations associated with points in $P'$ are deemed unsafe, the point is deemed a failure point and the cost associated with the failure point is increased. The rapid search is then called to re-plan the path. If the configurations in $P'$ are deemed safe, the motion planning problem is considered solved and the algorithm ends.
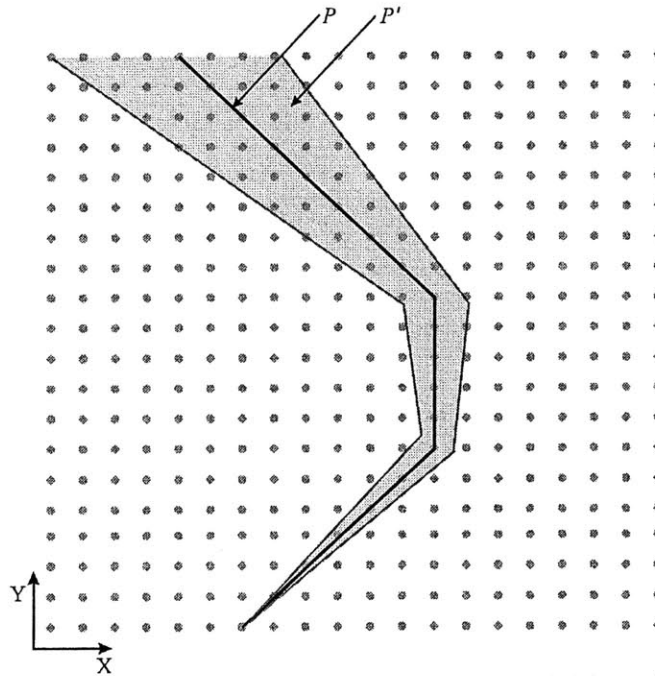


**Figure 3.7:** Effect of localization uncertainty on model-based evaluation

## 3.3 Simulation Results—Rough Terrain Planning

A simulation was performed of a six-wheeled rocker-bogie rover traversing rough terrain. The purpose of this simulation was to compare the rough-terrain planning method to a conventional planning methods which does not utilize knowledge of rover physics, does not consider uncertainty, and treats obstacles in a binary manner.

Three simulated terrains of increasing difficulty were generated by a pseudo-random terrestrial terrain generator based on the logit transform (Pickover, 1995) (see Figure 3.8 (a-c). The terrain generator creates elevation maps based on user-specified terrain feature density. Note that the maps in Figure 8 have been downsampled and rectangularly meshed for ease of viewing.



*(a)*

*(b)*

*(c)*
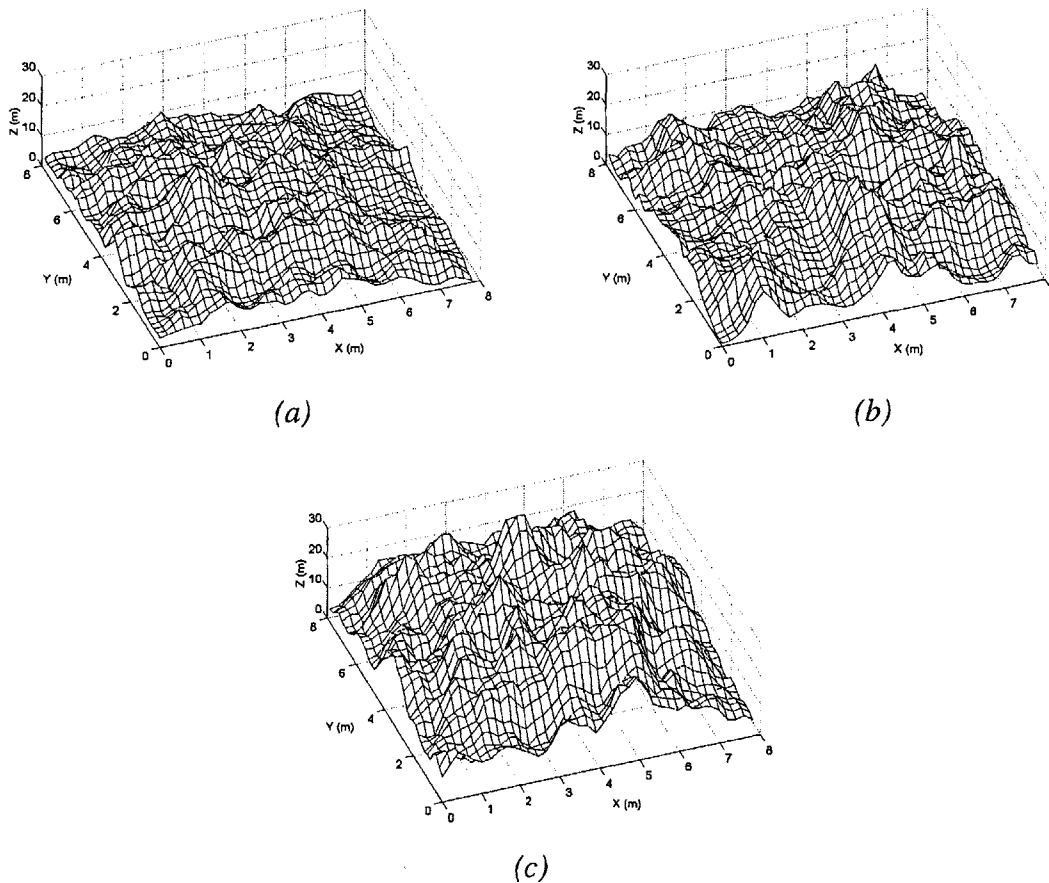
**Figure 3.8:** Simulated terrain elevation maps: benign (a), moderate (b), and difficult (c)

Ten trials were performed for each terrain. Start and goal locations were randomly-generated, with a minimum straight-line spacing of 5 m. Each terrain map was a grid of 195 x 195 equally-spaced terrain points, with a uniform square spacing of 4 cm. This corresponded to a map approximately 8 m square. For the rough terrain planning method, the exponent $\alpha$ in Equations (3.2) and (3.3) was taken as 3. The weighting factors $k_1$, $k_2$, and $k_2$ of the performance index defined in Equation (3.5) were 5.0, 0.1, and 0.1, respectively. The planning method was simulated on a 300 MHz Pentium PC.

The rough terrain planning method was compared to a conventional planning algorithm that attempted to find the shortest path between the start and goal while avoiding obstacles. Here, an obstacle was defined by considering the maximum change in elevation between a terrain point and its eight nearest neighbors. If the maximum change in elevation was greater than 80% of the diameter of a rover wheel, the terrain point was considered an obstacle. The obstacle "cutoff" height was chosen based on heuristic knowledge of the rover system, much as it might be done in practice. Based on this definition, the three terrain maps in Figure 8 had obstacle densities of 0.05, 0.23, and 0.72 obstacles/rover area. Thus, the terrain shown in Figure 3.8 (a) is fairly benign, while the terrain shown in Figure 3.8 (c) is densely populated with obstacles.

Results of the 30 simulation trials are summarized in Table 3.1. Rough terrain planning (RTP in the table) found safe paths that were on average 7.35% shorter than the binary planning method (BP in the table). This is due to the fact that rough terrain planning uses a physical model of the rover system, which allows it to plan paths through regions that a binary planning method would consider an obstacle. Since path length is

directly related to power consumption, the rough terrain planning method is a more power-efficient planning method than a conventional planning method.

Table 3.1: Results of motion planning algorithm comparison

| | | Average Path Length (m) | Average Computation Time (s) | Number of Reachable Goals |
|---|---|---|---|---|
| Terrain 1 | RTP | 6.02 | 35.5 | 10 |
| | BP | 6.44 | | 10 |
| Terrain 2 | RTP | 6.34 | 40.5 | 10 |
| | BP | 6.95 | | 9 |
| Terrain 3 | RTP | 6.95 | 118.1 | 9 |
| | BP | 7.48 | | 6 |

More important than path length, however, is the result that the rough terrain planning methods resulted in an increased number of reachable goals, compared to the binary planning method. For the highly difficult terrain shown in Figure 3.8 (c), the rough terrain planning method found 50% more safe paths than the binary planning method. This is a significant result for planetary exploration, where a goal point might be a potentially interesting science sample.

A representative simulation trial is presented in Figure 3.9. Paths through the terrain shown in Figure 3.8 (b) as found by the rough terrain planner and the binary planner are presented. It can be seen that the path generated by the rough terrain planner is more direct than the one generated by the binary planner. This is due to the fact that the binary planner viewed the crest at $(x,y) = (2.75, 2.10)$ as an obstacle and avoided it. The rough terrain planner analyzed the crest and determined it was traversable, and thus proceeded directly over it.
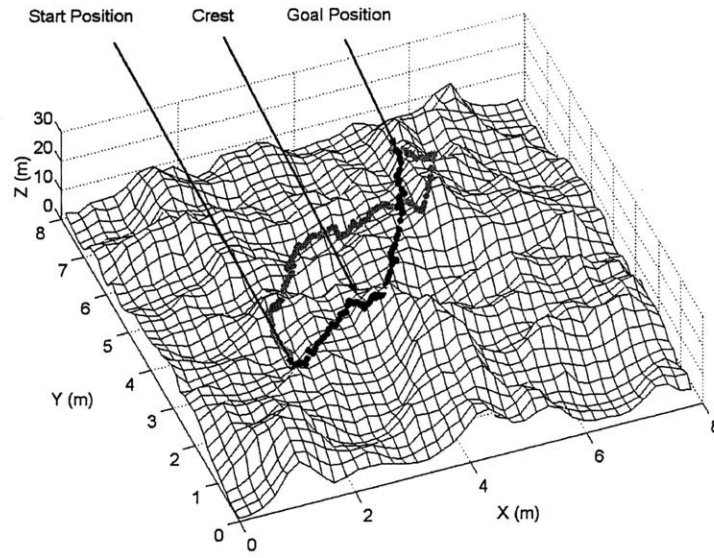
**Figure 3.9:** Representative simulation trial for rough terrain planning method (black) and binary planning method (gray)

A final simulation was conducted, with the obstacle cutoff height for the binary planner increased to 120% of the wheel diameter. This is an aggressive assumption about terrain traversability, which would be implemented to allow the rover to traverse highly rough terrain. Again, however, it is based on heuristic knowledge of the rover capabilities, and is not justified by rigorous model-based analysis. A route was planned through the terrain shown in Figure 3.8 (c), as shown in Figure 3.10. This route was deemed safe by the binary planning algorithm. However, review of the path by the model-based analysis showed a kinematic inadmissibility failure at point $(x,y) = (2.80, 3.00)$ and force analysis failures at point $(x,y) = (3.40, 3.40)$. The failure points were avoided in the rough terrain planning algorithm. However, the binary planning algorithm's lack of physical knowledge of the rover system leads to a potential failure situation.

---
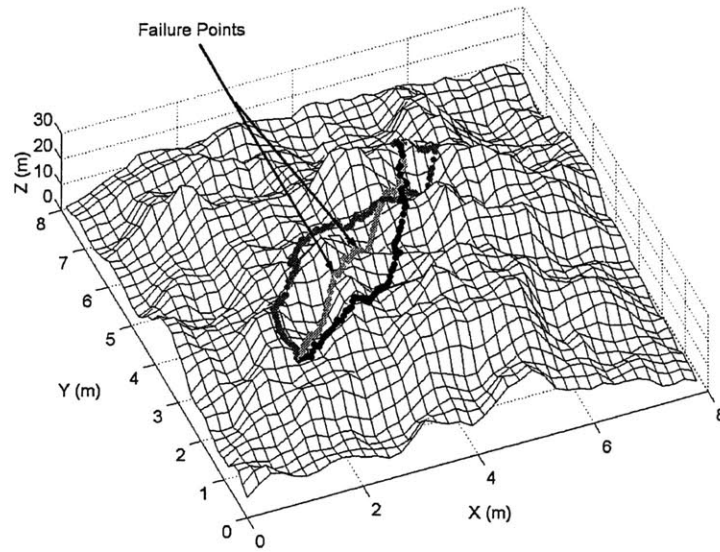
**Figure 3.10:** Simulation trial for rough terrain planing (black), binary planning method with obstacle criteria of 80% of one wheel diameter (dark gray), and binary planning with obstacle criteria of 120% of one wheel diameter (light gray)

Based on these results, it is clear that the rough-terrain planning algorithm plans paths that are shorter and safer than a traditional planning method, and allows access to a larger percentage of the terrain. All of these factors are important considerations in autonomous planetary exploration.

## 3.4 Rough-Terrain Kinematic Reconfigurability

To accomplish planned future missions, rovers may evolve from traditional "fixed configuration" designs to ones with actively reconfigurable suspensions (Schenker *et al.*, 2000). These "reconfigurable rovers" can modify their kinematic structure to improve mobility in rough terrain. For example, when traversing an incline a reconfigurable rover could modify its suspension configuration to increase its tipover stability margin (see Figure 3.11). In this section a method for kinematic reconfigurability is presented, and

applied to stability enhancement of the Jet Propulsion Laboratory Sample Return Rover (SRR) shown in Figure 3.12 (Huntsberger *et al.*, 1999). A summary of this work can be found in (Iagnemma *et al.*, 2000(c)). This work was performed in collaboration with Adam Rzepniewski of MIT.
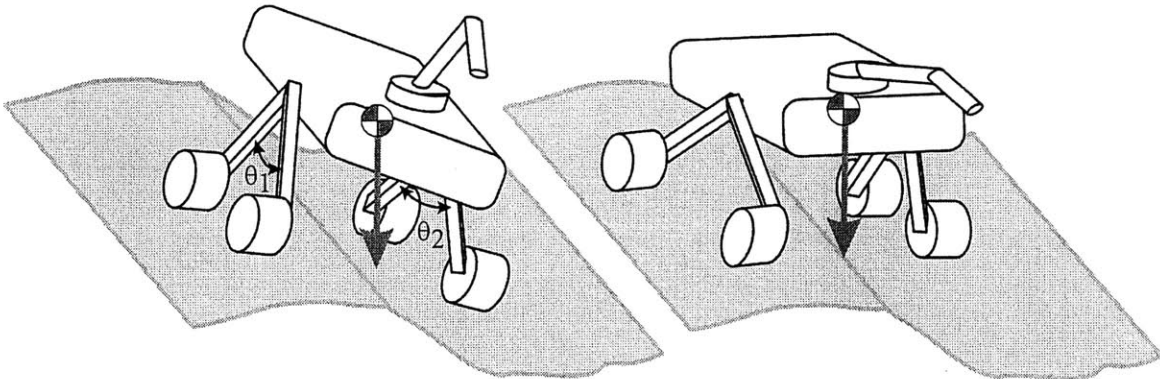


**Figure 3.11:** Example of reconfigurable robot improving rough-terrain stability by adjusting shoulder joints
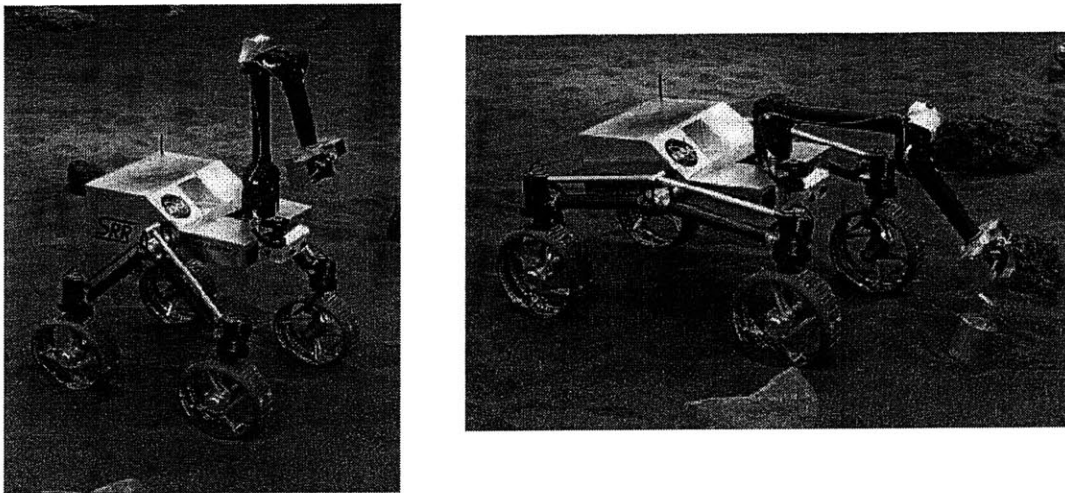


**Figure 3.12:** Jet Propulsion Laboratory Sample Return Rover (SRR)

Consider a general $n$-link tree-structured mobile robot on uneven terrain. An example of such a robot is shown in Figure 3.13. The $n$ links can form hybrid serial-parallel kinematic chains. It is assumed that the robot's $l$ joints are active revolute or prismatic joints, and their values are denoted $\theta_i$, $i=\{1,...,l\}$. It is also assumed that the make point

contact with the terrain. The *m* wheel-terrain contact points are denoted $P_j$, $j = \{1,...,m\}$ with their location defined as a vector $\mathbf{p}_j$ from the vehicle center of mass. The wheel-terrain contact angles at each point $P_j$ are denoted $\alpha_j$, $j = \{1,...,m\}$.
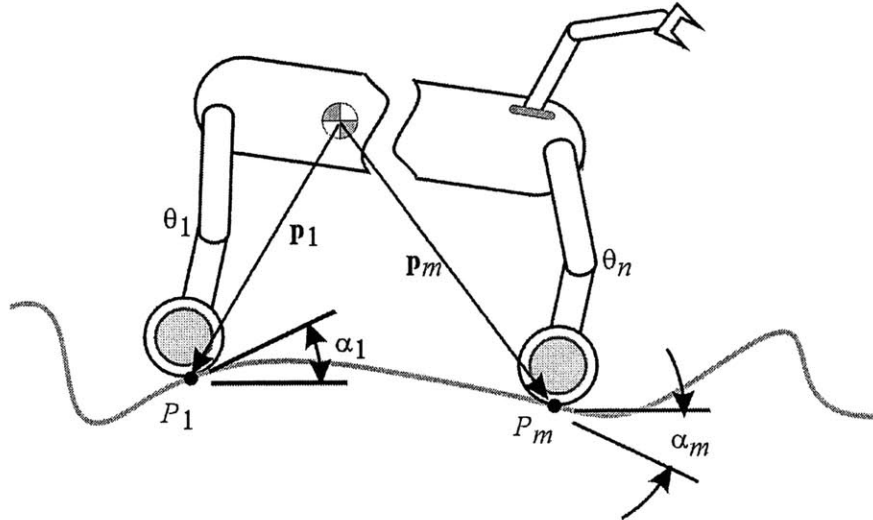


**Figure 3.13:** A general tree-structured mobile robot

The goal of kinematic reconfigurability is to improve robot performance by modifying the robot joint variables $\theta_i$ to optimize a user-specified performance index. This performance index might assess static stability, wheel traction, vehicle pose for optimal force application, or others. Since forward and inverse kinematic solutions of hybrid serial-parallel chains are in general difficult to formulate, analytical solutions often cannot be obtained for the optimal kinematic configuration. This motivates the use of numerical optimization techniques.

On-line kinematic reconfigurability requires three steps:

1) Evaluation of the robot kinematic configuration using on-board sensor readings. The configuration is defined as $Q = (\theta_1,...,\theta_l, \alpha_1,...,\alpha_m, \Theta, \Phi)$ where $\Theta$ and $\Phi$ denote the roll and pitch, respectively, of a reference member

such as the vehicle body measured in an inertial frame. The wheel-terrain contact angles $\alpha_j$ can be estimated from stereo range data or via on-board sensor-based methods (refer to Section 2.5) (Balaram, 2000).

2) Computation of a kinematic configuration $Q'$ which optimizes a performance index based on the joint variables $\theta_i$.

3) Motion from the current configuration $Q$ to the optimal configuration $Q'$.

Kinematic reconfigurability is divided here into two cases: internal reconfigurability and external reconfigurability. These cases are discussed below.

*Internal reconfigurability*

In internal reconfigurability the wheel-terrain contact points $P_j$ remain fixed relative to the terrain during the reconfiguration process (see Figure 3.14). Note that the wheels must be actively controlled to remain fixed without rolling. An internally reconfigurable robot has mobility greater than or equal to one while stationary on the terrain (i.e. the robot has available self-motions), as defined by the Grubler mobility criterion (Eckhardt, 1989):

$$F = 6(l - j - 1) + \sum_{i=1}^{j} f_i \qquad (3.20)$$

where $j$ is the number of joints, $l$ is the number of links including the ground, and $f_i$ is the number of constraints for each joint $i$. For an internally reconfigurable system the wheel is not allowed to translate, but is allowed to rock about two axes in the plane of the terrain and twist about an axis normal to the terrain.
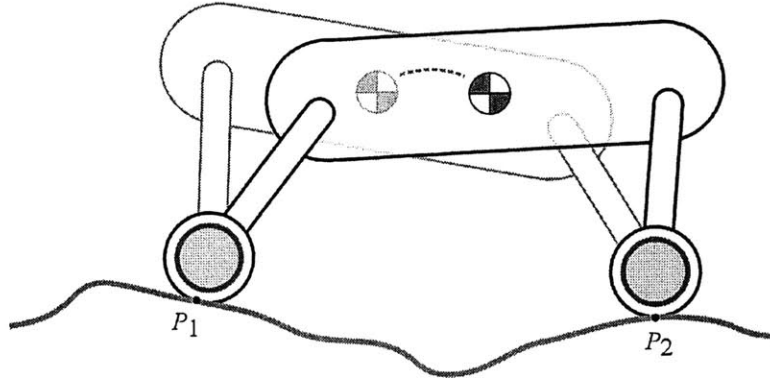
**Figure 3.14:** Planar view of a mobile robot undergoing internal reconfiguration

For an internally reconfigurable robot the terrain profile does not influence the reconfiguration process. The robot configuration can be defined without terrain information as $Q = (\theta_1,...,\theta_n,\ \Theta,\ \Phi)$. Thus, knowledge of robot kinematics alone is sufficient to pose the optimization problem. Note that for an internally reconfigurable robot it is theoretically possible to find a globally optimal solution for the kinematic configuration. The dimension of the optimization search space is equal to the internal mobility $F$ of the system.

Optimization constraints in internally reconfigurable systems take the form of joint limit and interference constraints, and kinematic loop equations between wheel-terrain contact points to ensure they remain fixed.

*External reconfigurability*

In external reconfigurability one or more wheel-terrain contact points $P_j$ move relative to the terrain during the reconfiguration process. The robots in Figures 3.11 and 3.12 are examples of externally reconfigurable robots. Note that the mobility analysis of an externally reconfigurable robot is different from that of an internally reconfigurable robot. Wheel-terrain contacts must be treated as higher-order pairs (Eckhardt, 1989).

For externally reconfigurable robots the terrain profile influences the reconfiguration process. Without knowledge of the terrain profile it is impossible to find a globally optimal solution for the kinematic configuration. The terrain profile is generally not well known. However, the local wheel-terrain contact angles can be estimated. The wheel-terrain contact angle $\alpha_j$ describes the terrain profile in a local region about the point $P_j$. An optimization problem can therefore be posed with the constraint that the rover configuration change results in only small displacements of the points $P_j$ with respect to the terrain. Thus, a locally optimal solution for the kinematic configuration can be found.

Optimization constraints in an externally reconfigurable system take the form of kinematic joint limit and interference constraints, and joint excursion limits that restrict the displacements of the points $P_j$ relative to the terrain.

### 3.4.1 Stability-Based Kinematic Reconfigurability

The reconfiguration methodology outlined above can be used to improve different criteria such as tipover stability or traction. In this section a method for stability-based kinematic reconfigurability is described. A static analysis is performed due to the low speeds of planetary exploration rovers (on the order of several cm/sec).

In Section 3.2.2 a vehicle stability metric was defined. Here, the stability metric is extended to consider the effects of manipulator forces. A performance index is then proposed that depends on this stability metric, and an optimization method for reconfigurability is outlined.

*Stability Analysis Extension*

In rough-terrain a rover may be required to manipulate its environment. Some manipulation tasks, such as coring, may require the application of large forces, which could have a destabilizing effect on the robot. During these tasks it would be desirable for the rover to optimize its kinematic structure to maximize stability.

Manipulation forces can be accounted for in the stability computation. Given an applied force $\mathbf{f}_m$ by the manipulator on its environment, the resultant force along a tipover axis is computed as:

$$\mathbf{f}_i = \left(\mathbf{1} - \hat{\mathbf{a}}_i \hat{\mathbf{a}}_i^T\right)\left(\mathbf{f}_g + \mathbf{f}_m\right). \tag{3.21}$$

with $\mathbf{f}_m$ expressed in an inertial frame.

If there is a moment $\mathbf{n}_m$ associated with $\mathbf{f}_m$, the net force about a tipover axis is computed with Equation (3.21) and:

$$\mathbf{f}_i^* = \mathbf{f}_i + \frac{\hat{\mathbf{l}}_i \times \left(\hat{\mathbf{a}}_i \hat{\mathbf{a}}_i^T\right)\mathbf{n}_m}{\|\mathbf{l}_i\|} \tag{3.22}$$

The stability angle $\alpha$ is then computed from Equations (3.9-3.11) using the net force $\mathbf{f}_i^*$.

*Performance index definition and optimization method description*

To optimize the rover configuration for maximum stability, a performance index $\Phi$ is defined based on the above stability measure. A function of the following form is proposed:

$$\Phi = \sum_{i=1}^{n}\left(\frac{K_i}{\gamma_i} + K_{n+i}\left(\theta_i - \theta_i'\right)^2\right) \tag{3.23}$$

where $\gamma_i$ are the stability angles defined in Equation (3.9), $\theta_i'$ are the nominal values of the $i^{\text{th}}$ joint variables (i.e. the values of $\theta_i$ when the robot is at a user-specified configuration, such as on flat terrain), and $K_i$ are constant weighting factors.

The first term of $\Phi$ tends to infinity as the stability at any tipover axis tends to zero. The second term penalizes deviation from a nominal configuration of the shoulder joints, thus maintaining adequate ground clearance, an important consideration in rough terrain. The constants $K_i$ allow control of the relative importance of vehicle stability and joint excursion. Since joint excursion is directly related to power consumption, this can also be viewed as control of the stability-power consumption tradeoff.

The goal of the stability-based kinematic reconfigurability optimization problem is to minimize the performance index $\Phi$ subject to joint-limit, interference and possibly kinematic loop constraints. Since $\Phi$ possesses a unique local minimum for simple systems such as the SRR, a rapid optimization technique such as the conjugate-gradient search can be employed (Arora, 1989).

## 3.5 Results—Rough-Terrain Kinematic Reconfigurability

Simulation and experiments of the kinematically reconfigurable Jet Propulsion Laboratory Sample Return Rover traversing rough terrain were performed. These results are presented below.

### 3.5.1 Simulation Results

Simulations of the JPL SRR traversing rough terrain were performed. The SRR is a 7 kg, four-wheeled mobile robot with independently steered wheels and independently

controlled shoulder joints (Huntsberger *et al.*, 1999) (see Figure 3.12). A 2.25 kg three

d.o.f. manipulator is mounted at the front of the SRR. The controllable shoulder joints

and manipulator allow the SRR to reposition its center of mass. The SRR is equipped

with an inertial navigation system to measure body roll and pitch. Since the ground

speed of the SRR is typically 6 cm/sec, dynamic forces do not have a large effect on

system behavior, and thus static stability-based reconfigurability is appropriate.

Planar mobility analysis shows that the SRR has a mobility of 0. Thus the rover is

only externally reconfigurable. This is intuitively correct, as the SRR cannot reconfigure

a shoulder joint without moving at least one wheel-terrain contact point relative to the

terrain.

The optimization performance index used in the simulation was similar to Equation

(3.23) and considered the two shoulder angle joints $\theta_1$ and $\theta_2$ and the three manipulator

degrees of freedom $\psi_1$, $\psi_2$, and $\psi_3$:

$$\Phi = \sum_{j=1}^{4} \frac{K_j}{\gamma_j} + \sum_{i=1}^{2} K_{i+4} \left( \theta_i - \theta_i{}' \right)^2 \tag{3.24}$$

Note that the stability angles $\gamma_j$ are functions of the shoulder and the manipulator degrees

of freedom (i.e. $\gamma_j = \gamma_j(\theta_1, \theta_2, \psi_1, \psi_2, \psi_3)$).

Results of a representative simulation trial are shown in Figure 3.15. Vehicle stability

margin as defined by Equation (3.11) is plotted for reconfigurable and fixed-

configuration systems. The mean stability of the reconfigurable system was 37.1%

greater than the fixed-configuration system. The stability margin of the fixed-

configuration system reaches a minimum value of 1.1°, indicating that the system

narrowly avoided tipover failure. The minimum stability margin of the reconfigurable system was 12.5°, a comfortable margin.
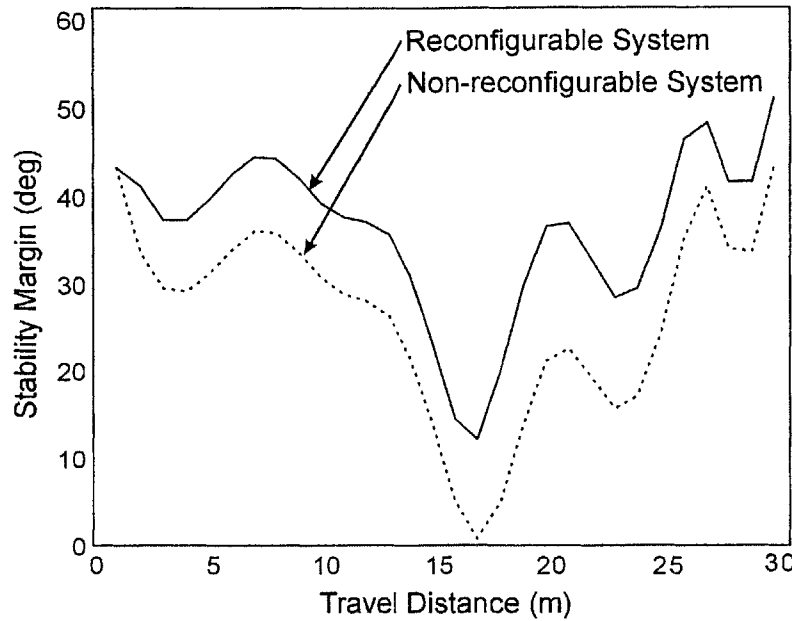


**Figure 3.15:** SRR Stability margin for reconfigurable system (solid) and non-reconfigurable system (dotted)

### 3.5.2 Experimental Results

Numerous experimental trials were performed on the SRR in the JPL Planetary Robotics Laboratory and the Arroyo Seco in Altadena, California by Adam Rzepniewski of MIT and a support team of JPL researchers. The SRR was commanded to traverse a challenging rough-terrain path that threatened vehicle stability. For each trial the path was traversed first with the shoulder joints fixed, and then with the kinematic reconfigurability algorithm activated.

Results of a representative trial are shown in Figures 3.16 and 3.17. Figure 3.16 shows the shoulder joint angles during the traverse. Both left and right shoulder angles remain within the joint limits of ±45° of the initial values. Note that the non-reconfigurable shoulder angles vary slightly due to servo compliance.

Figure 3.17 shows vehicle stability for reconfigurable and fixed-configuration traverses. The average stability of the reconfigurable system was 48.1% greater than the fixed-configuration system. The stability margin of the fixed-configuration system reached dangerous minimum values of 2.1° and 2.5°. The minimum stability margin of the reconfigurable system was 15.0°. Clearly, kinematic reconfigurability results in greatly improved stability in rough terrain.
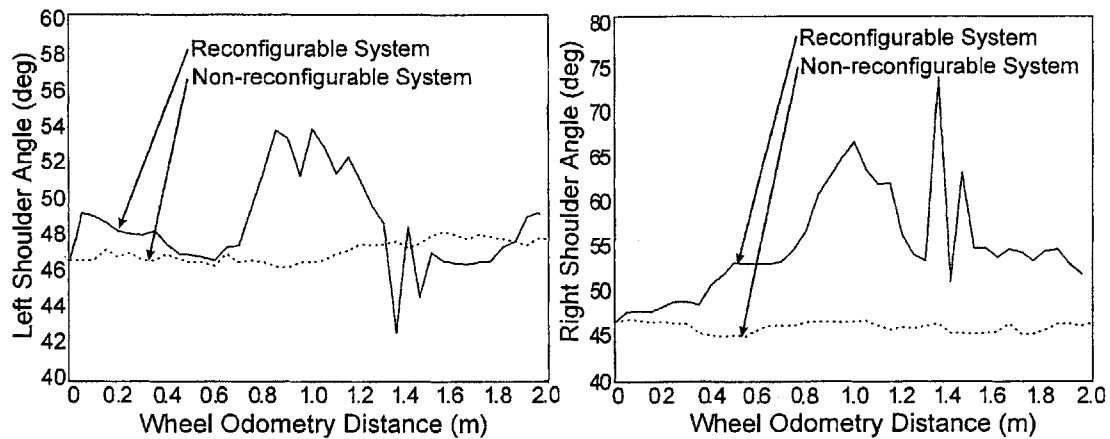
**Figure 3.16**: SRR left (a) and right (b) shoulder angles during rough-terrain traverse for reconfigurable system (solid) and non-reconfigurable system (dotted)
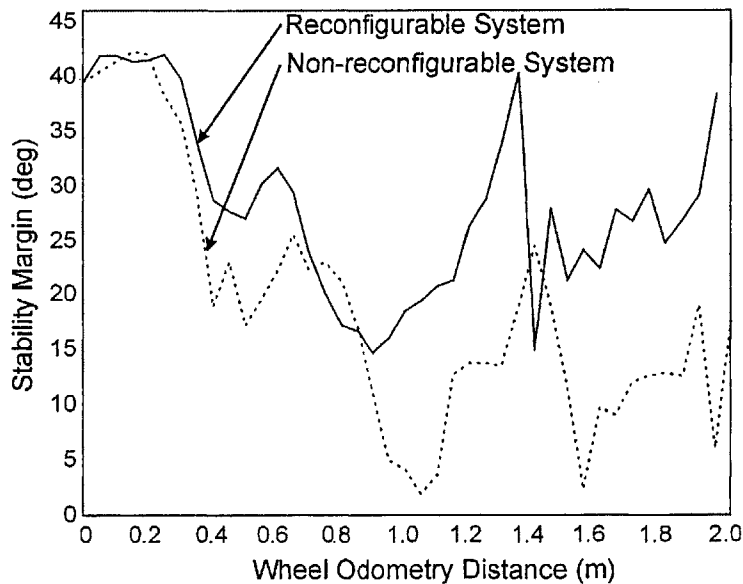
**Figure 3.17**: SRR stability margin for reconfigurable system (solid) and non-reconfigurable system (dotted)

Optimization was performed on-line with a 300MHz AMD K6 processor. Average processing time for a single constrained optimization computation was 40 $\mu$sec. Thus, the kinematic reconfigurability greatly improves tipover stability in rough terrain and is feasible for on-board implementation.

## 3.6    Summary and Conclusions

In this chapter a model-based planning method for rough-terrain rovers was presented. The method utilizes range sensor data to rapidly plan a route through local ($\approx$ 5-10 rover length range) terrain. The rapid path search uses an estimate of terrain roughness, and is based on a classical $A^*$ algorithm. This route is then evaluated rigorously with a physical rover model. Uncertainty in terrain range data and rover localization uncertainty are accounted for in the method. Simulation results show that the rough-terrain planning method results in shorter path lengths, safer paths, and increased terrain accessibility compared to a traditional approach.

A method for stability-based reconfigurability was also presented. The method optimizes a performance index relating the reconfigurable joint variables to vehicle stability angles. Simulation and experimental results for the JPL SRR show that the method yields greatly improved tipover stability in rough terrain.

# Chapter

# 4

# Rough-Terrain Control:
# How Should a Rover Do It?

## 4.1 Introduction

This chapter presents a rough-terrain control (RTC) algorithm for mobile robots. This algorithm uses the models and techniques developed earlier in this thesis to improve rover mobility in rough terrain. Section 4.2 outlines the theoretical background of the method. Section 4.3 discusses optimization methods and constraints for RTC. Section 4.4 presents simulation and experimental results of the RTC algorithm, and shows that it improves mobility of a multi-wheeled rover in rough terrain compared to a traditional velocity-controlled system.

## 4.2 Mobile Robot Rough Terrain Control (RTC)

Future planetary exploration missions will require rovers to traverse highly challenging terrain (Hayati, 1996; Matijevic, 1997(c); Schenker, 1997). Most control algorithms are not well suited to rough-terrain, since they do not consider the physical capabilities of both the rover and its environment. In this section, the theoretical background of a

rough-terrain control algorithm is presented that utilizes models of the rover and terrain to improve mobility. A summary of this work can be found in (Iagnemma and Dubowsky, 2000(b)).

Consider an $n$-wheeled mobile robot on rough terrain, shown in Figure 4.1. In the following analysis it is assumed that wheel-terrain contact occurs at a single point. The validity of this assumption was discussed in Section 2.5. It is also assumed that no moments exist at the wheel-terrain contact points, a reasonable assumption for natural terrain (Bekker, 1969). Finally, it is assumed that the vehicle is steered via skid-steering. The motivation for this assumption will be discussed later in this section.
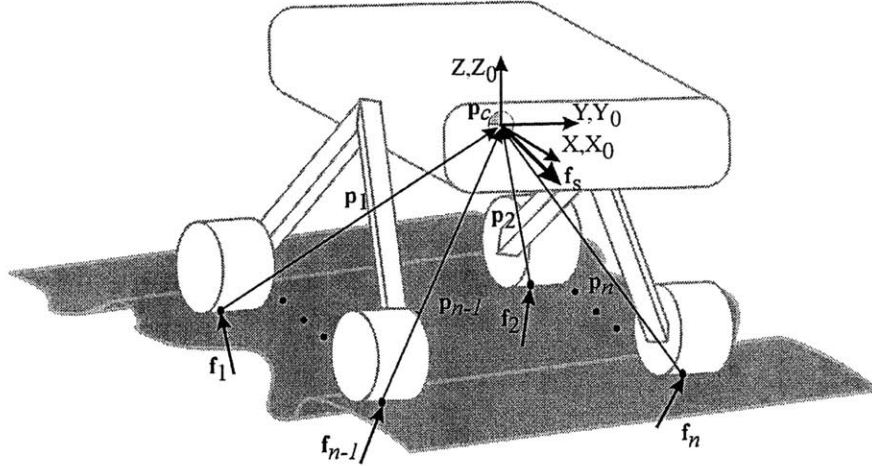


**Figure 4.1**: An $n$-wheeled rover in rough terrain

The vectors $\mathbf{f}_i = [f_i^x \, f_i^y \, f_i^z]^T$, $i = \{1,\ldots,n\}$, represent wheel-terrain interaction forces and are expressed in the inertial frame $\{XYZ\}$. The vectors $\mathbf{p}_i = [p_i^x \, p_i^y \, p_i^z]^T$, $i = \{1,\ldots,n\}$, are directed from the wheel-terrain contact points to the rover center of mass and are also expressed in the inertial frame $\{XYZ\}$. The vector $\mathbf{f}_s = [F_s^x \, F_s^y \, F_s^z \, M_s^x \, M_s^y \, M_s^z]^T$ at the rover center of mass represents the summed effects of gravitational forces, inertial forces, forces due to manipulation, and forces due to interaction with the environment or other robots.

Note that $\mathbf{f}_s$ possesses a user-specified component in the direction of desired motion. This user-specified component is an input to the rough-terrain control algorithm. The goal of RTC is to find a set of vectors $\mathbf{f}_i$ that balances $\mathbf{f}_s$ while optimizing a user-defined criteria, such as maximum traction or minimum power.

A set of quasi-static force-balance equations can be written for the system in Figure 4.1, as:

$$
\begin{bmatrix}
\mathbf{I} & & \vdots & \cdots & \vdots & & \mathbf{I} & \\
\hline
0 & p_1^z & p_1^y & & 0 & p_n^z & p_n^y \\
-p_1^z & 0 & -p_1^x & \cdots & -p_n^z & 0 & -p_n^x \\
-p_1^y & p_1^x & 0 & & -p_n^y & p_n^x & 0
\end{bmatrix}
\begin{bmatrix}
\mathbf{f}_1 \\
\vdots \\
\mathbf{f}_n
\end{bmatrix} = \mathbf{f}_s
\qquad (4.1)
$$

where $\mathbf{I}$ represents a 3 x 3 identity matrix. This set of equations can be written in compact matrix form as:

$$
\mathbf{Gx} = \mathbf{f}_s \qquad (4.2)
$$

where $\mathbf{x} = [\mathbf{f}_1,...,\mathbf{f}_n]^T$.

Equation set (4.2) is generally referred to as the force distribution equations (Hung *et al.*, 1999). This set of equations represents 6 equations in $3n$ unknowns. Note that the rank of the matrix $\mathbf{G}$ is six unless all $n$ wheel-terrain contact points are collinear, a trivial case. As discussed in Section 2.2 and Appendix A, the force analysis problem is underconstrained, and thus there exists an infinite set of wheel-terrain interaction force vectors $\mathbf{f}_i$ that balance $\mathbf{f}_s$. In general, the force analysis problem will be underconstrained except for the trivial case of a two-wheeled vehicle.

It is important to note, however, that wheeled mobile robots can only influence forces in the wheel plane. They cannot influence forces transverse to the wheel plane (i.e.

parallel to the wheel axle). The force analysis problem can thus be simplified by considering a planar analysis. This is a reasonable simplification for skid-steered rovers, or rovers travelling in a straight line.

### 4.2.1 Planar Force Analysis

Consider the planar view of an $n$-wheeled mobile robot on rough terrain, shown in Figure 4.2. It is again assumed that each wheel makes contact with the terrain at a single point, denoted $P_i$, $i = \{1,...,n\}$. Vectors from the points $P_i$ to the robot center of mass are denoted $\mathbf{p}_i = [p_i^x \ p_i^y]^T$, $i = \{1,...,n\}$ and are now expressed in the local frame $\{xy\}_i$ fixed at $P_i$. The 3x1 vector $\mathbf{f}_s = [F_s^x \ F_s^y \ M_s^z]^T$ is expressed in the inertial frame $\{XYZ\}$ and represents the summed effects of gravitational forces, inertial forces, forces due to manipulation, and forces due to interaction with the environment or other robots.
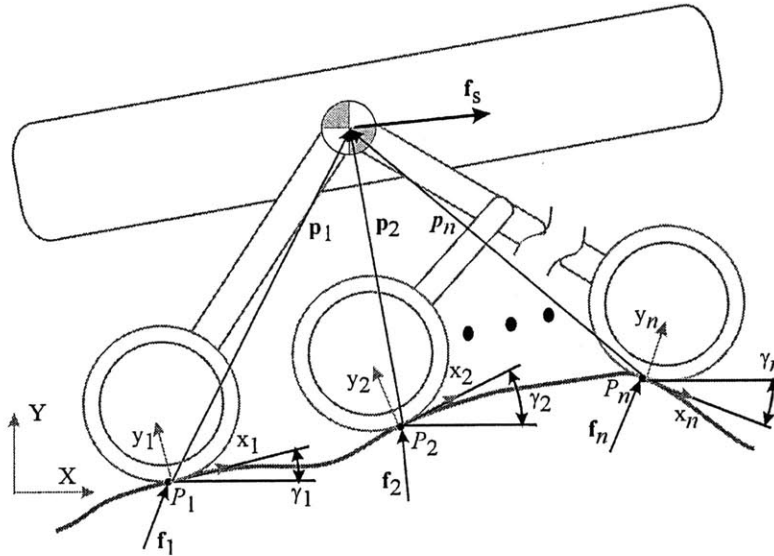


**Figure 4.2:** Planar view of $n$-wheeled rover on rough terrain

A wheel-terrain contact force exists at each point $P_i$ and is denoted $\mathbf{f}_i = [T_i \ N_i]^T$ (see Figure 4.3). The vector is expressed in the local frame $\{xyz\}_i$ and can be decomposed into

a tractive force $T_i$ tangent to the wheel at the wheel-terrain contact point, and a normal force $N_i$ normal to the wheel at the wheel-terrain contact point. It is again assumed that there are no moments acting at the wheel-terrain interface. The angles $\gamma_i$, $i = \{1,...,n\}$ represent the wheel-terrain contact angles.
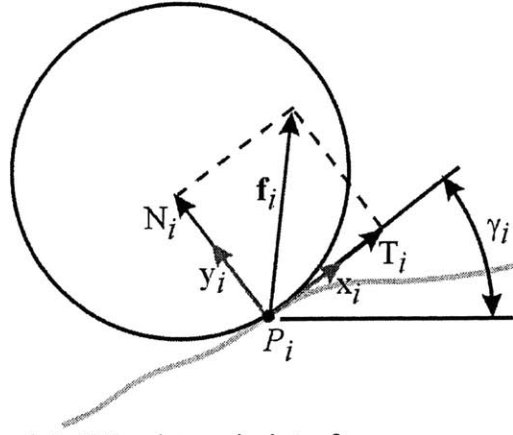


**Figure 4.3:** Wheel-terrain interface on uneven terrain

For the planar system shown in Figure 4.2 a set of quasi-static force balance equations can be written as:

$$
\begin{bmatrix} {}^0\mathbf{R}_1 & \vdots & {}^0\mathbf{R}_2 & \vdots & \cdots & \vdots & {}^0\mathbf{R}_n \\ p_1^y & -p_1^x & \vdots & p_2^y & -p_2^x & \vdots & \cdots & \vdots & p_n^y & -p_n^x \end{bmatrix} \begin{bmatrix} \mathbf{f}_1 \\ \vdots \\ \mathbf{f}_n \end{bmatrix} = \begin{bmatrix} F_x \\ F_y \\ M_z \end{bmatrix} \tag{4.3}
$$

where ${}^i\mathbf{R}_j$ represents a 2x2 rotation matrix transforming a vector expressed in frame $j$ to one in frame $i$.

We can again represent the force balance equations (Equation (4.3)) in matrix form as:

$$
\mathbf{Gx} = \mathbf{f}_s \tag{4.4}
$$

Equation set (4.4) represents 3 equations in $2n$ unknowns. In general, a planar system with $n$ wheel-terrain contact points possesses $(2n-3)$ degrees of actuation redundancy.

Note that in Equation 4.4 each element of the vector **x** can be modified by wheel input torques. The rough-terrain control problem is therefore to determine the set of input torques that balances the input body force $f_s$ while optimizing an aspect of system performance, such as traction or power consumption. The optimization approach is discussed below.

## 4.3    Wheel-Terrain Contact Force Optimization

Rovers operating in rough terrain must maintain good wheel traction. However, during traverses of benign terrain it is desirable that they be power-efficient. Optimization of wheel-terrain contact forces can be performed using several criteria, including maximum traction or minimum power consumption. These criteria are discussed below. Constraints on the optimization problem are then discussed.

### 4.3.1    Optimization Criteria

The actuation redundancy in Equation 4.4 can be resolved by optimizing the solution vector **x** subject to a user-defined criteria. An optimization criteria for maximizing traction can be developed based on the observation that for most soils the maximum allowable tractive force increases with increasing normal force (Bekker, 1969). Tractive force applied beyond this maximum results in soil failure and wheel slip.

A function $R$ representing the maximum ratio of the tractive force to the normal force can thus be used as an objective function for optimizing the force distribution equations:

$$R = \max_i \left\{ \frac{T_i}{N_i} \right\}$$

(4.5)

To maximize rover wheel traction, $R$ must be minimized. Physically, this is equivalent to diminishing the force ratio of the wheel closest to soil failure.

Similar criteria has been developed in (Sreenivasan and Wilcox, 1994) and an analytical solution to the optimization problem has been developed for a planar two-wheeled vehicle. In general, the optimal solution of the force distribution equations (Equation (4.4)) can be solved by standard optimization techniques such as linear programming (Chung and Waldron, 1993). This solution yields a set of tractive forces that can easily be converted to actuator torques and used for control.

An optimization criteria for minimum power consumption can be developed based on the fact that power consumption in a DC motor using PWM amplifiers can be estimated from the power dissipated in the motor resistance (Dubowsky $et\ al.$, 1995):

$$P = \sum_{i=1}^{n} R_i c_i^2 \tag{4.6}$$

where $R_i$ is the motor resistance and $c_i$ is the current in the $i^{\text{th}}$ motor. The current $c_i$ is related to the motor torque $\tau_i$ by:

$$c_i = \frac{\tau_i}{K_i^t} \tag{4.7}$$

where $K_i^t$ is the motor torque constant. Power consumption of the rover is thus a function of the motor torque:

$$P = \sum_{i=1}^{n} \frac{R_i \tau_i^2}{K_i^{t\,2}} \tag{4.8}$$

It is desirable to express power consumption in terms of the tractive force applied at the wheel-terrain interface, rather than the motor torque. The tractive force can be expressed as a function of the motor torque as:

$$T_i = \frac{N_i \tau_i}{r_i} \qquad (4.9)$$

where $r_i$ is the wheel radius and $N_i$ is the motor gear ratio. Rover power consumption can then be related to the tractive force $T_i$ as:

$$P = \sum_{i=1}^{n} \left( \frac{R_i r_i^2}{K_i'^2 N_i^2} \right) T_i^2 \qquad (4.10)$$

The function $P$ can be used as an objective function for power minimization. To minimize power consumption, $P$ must be minimized.

The two optimization criteria of Equations (4.3) and (4.8) can be combined into a dual-criteria objective function that optimizes for maximum traction or minimum power consumption depending on the terrain profile. In highly uneven terrain the objective function would maximize traction. In relatively flat terrain the objective function would minimize power consumption. This is desirable since planetary mobile robots operating in rough terrain must maintain adequate wheel traction. However, during traverses of benign terrain it is desirable that they be power-efficient.

A measure of terrain unevenness can be formulated based on the values of the wheel-ground contact angles (see Section 2.5). Consider the switching function $S$:

$$S = \begin{cases} 1 & \text{if } \max_i \{|\gamma_i|\} > C \\ 0 & \text{otherwise} \end{cases} \qquad (4.11)$$

where $C$ is an arbitrary constant threshold level. This function distinguishes between benign and challenging terrain. An objective function which combines Equations (4.5), (4.10), and (4.11) can then be expressed as:

$$Q = RS + T(1 - S) \qquad (4.12)$$

The optimization problem can thus be stated as follows: *Minimize Q subject to the equality constraint* $\mathbf{Gx = f}_s$. The solution to this problem will be a set of wheel-terrain thrust forces that are optimized for either maximum traction or minimum power consumption, depending on the local terrain profile. These thrust forces can be converted to actuator torques, which can then be applied to the rover wheels (see Section 2.3).

## 4.3.2 Optimization Constraints

Solutions of the force distribution equations must obey system physical constraints. The first physical constraint requires that all wheels remain in contact with the terrain, or equivalently that the normal force at each wheel remains positive:

$$N_i > 0, \quad \forall i, \ i = \{1,...,n\} \tag{4.13}$$

The second physical constraint requires that all joint torques remain within the saturation limits of the actuator, or:

$$\tau_i^{min} \leq (T_i \cdot r_i) \leq \tau_i^{max}, \quad \forall i, \ i = \{1,...,n\} \tag{4.14}$$

The third physical constraint requires that the tractive force exerted on the terrain not exceed the maximum shearing force the terrain can bear. If the applied shear force exceeds the allowable force, soil failure and excessive wheel slip will result. The maximum shearing force can be determined from Mohr-Coulomb theory and knowledge of soil parameters (see Section 2.3) as:

$$T^m = A(c + \sigma_m \tan\phi) \tag{4.15}$$

where $A$ is the wheel projected area and is a function of the wheel width and sinkage. A constraint can be written as:

$$-T_i^m \leq T_i \leq T_i^m, \quad \forall i, \ i = \{1,...,n\} \tag{4.16}$$

Thus, a solution to the force distribution equations must satisfy the equality constraint $\mathbf{Gx} = \mathbf{f}_s$ and must also obey the inequality constraints described by Equation (4.13), Equation (4.14), and Equation (4.16). See Figure 4.4 for a flowchart of the RTC algorithm. Note that this is an open-loop control scheme, in that there is no closed-loop feedback of the desired body force $\mathbf{f}_s$.

$$\mathbf{f}_S \downarrow$$

Wheel-terrain contact angle estimation (Section 2.5) → Evaluate rover configuration and form matrix **G**

↓

Evaluate switching function $Q = RS + T(1\text{-}S)$

↓

Wheel-terrain interaction analysis (Section 2.3) → Solve $\mathbf{Gx} = \mathbf{f}_S$ subject to constraints

$$T_i \downarrow$$
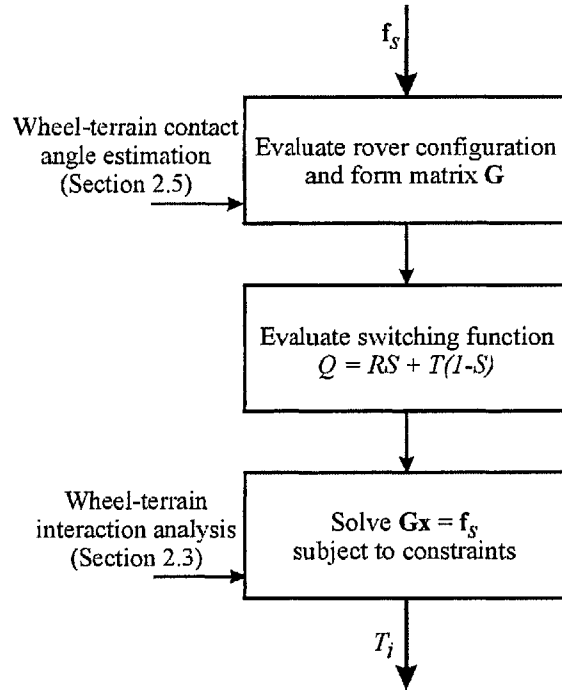
**Figure 4.4:** Block diagram of RTC algorithm

## 4.4 Results

Simulation and experiments of the RTC methodology were performed on the FSRL experimental rover system. These results are presented below.

### 4.4.1 Simulation Results

Performance of the RTC algorithm was compared in simulation to traditional individual-wheel velocity control. Velocity control was chosen for comparison since is a standard

rover control method. The simulated system is a planar, two-wheeled 10 kg vehicle traveling over rough terrain (see Figure 4.5). The wheel radius is 10 cm and wheel width is 15 cm. The wheel spacing is 70 cm. Measured quantities are assumed to be rover pitch and wheel angular velocities. Sensor noise was modeled as white noise with standard deviation equal to 5% of the full-range of values experienced during the simulation.
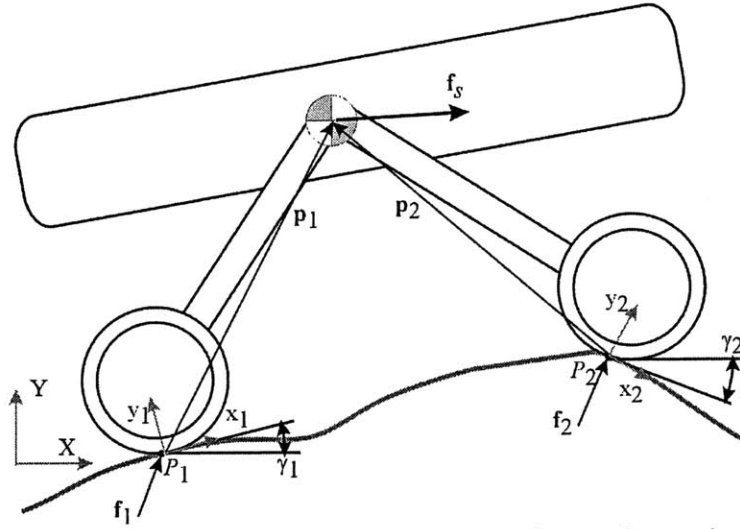


**Figure 4.5:** Two-wheeled planar rover in rough terrain

The force distribution equations for the simulated system can be written as:

$$\begin{bmatrix} \cos(\gamma_1) & -\sin(\gamma_1) & \cos(\gamma_2) & -\sin(\gamma_2) \\ \sin(\gamma_1) & \cos(\gamma_1) & \sin(\gamma_2) & \cos(\gamma_2) \\ p_1^y & -p_1^x & p_2^y & -p_2^x \end{bmatrix} \begin{bmatrix} T_1 \\ N_1 \\ T_2 \\ N_2 \end{bmatrix} = \begin{bmatrix} F_s^x \\ F_s^y \\ M_s^z \end{bmatrix} \quad (4.17)$$

This system of equations possesses $(2n-3) = 1$ degree of actuation redundancy. Thus, one of the tractive forces can be viewed as a free variable, which can be selected based on the dual-criteria optimization method discussed in Section 4.3.1.

The terrain was modeled as a moderately sandy soil similar to that which has been observed on Mars (Matijevic *et al.*, 1997(a); NASA 1988). The following soil parameters were used:

- Cohesion $c = 1.0$ kPa

- Internal slip angle $\theta = 29°$

- Bulk density $\rho = 1500$ kg/m$^3$

- Sinkage coefficient $n_s = 1$

- Frictional modulus of deformation $K_\phi = 850$ kN/m$^{n+2}$

- Coefficient of soil slip $k = 0.03$ m

At each simulation time increment the wheel thrust, motion resistance, and sinkage was computed as a function of the soil parameters, applied wheel torque, and wheel slip, as described in Section 2.3. Wheel sinkage was computed for each wheel as (Bekker, 1969):

$$z_i = \left[ \frac{3N_i}{(3-n_s)wK_\phi\sqrt{2r}} \right]^{\frac{2}{2n_s+1}} , \quad \forall i, \ i = \{1,...,2\} \tag{4.18}$$

Two representative simulation results are presented below. The first simulation involved the traverse of gently rolling terrain, shown in Figure 4.6. The velocity-controlled system was controlled with an individual-wheel PID control scheme with a desired angular velocity of 2.5 rad/sec. The RTC system was commanded by a horizontal inertial force vector of magnitude equal to the difference between a desired body velocity of 25 cm/sec and the actual body velocity, divided by the vehicle mass. Note that the RTC system is not explicitly velocity controlled. That is, if constraints must be violated to attain the desired body velocity of 25 cm/sec, the RTC system will travel slower than

25 cm/sec. The dual-criteria optimization threshold $C$ was set equal to 15°, since wheel-terrain angles below this threshold can generally be considered benign.
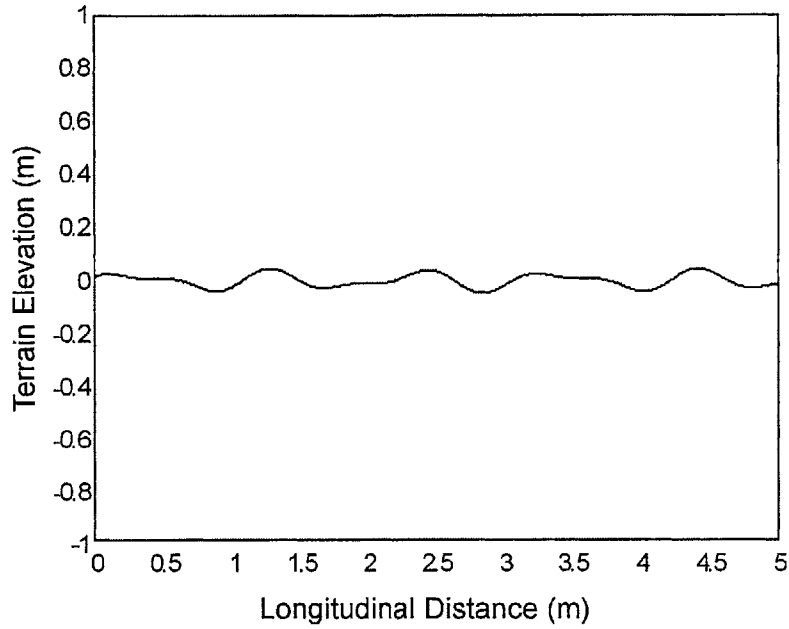


**Figure 4.6:** Simulated benign terrain profile

Both the velocity-controlled and RTC system successfully traversed the terrain, with the dual-criteria optimization remaining in energy-minimization mode during the traverse. The average power consumed by the RTC system was 2.9 W compared to 4.7 W by the velocity-controlled system, an improvement of 38.3%. This power savings is due to reduced wheel slip, as shown in Figure 4.7. The RTC system has an average slip ratio of 5.3% during the traverse while the velocity controlled system has an average slip of 9.4%. Thus, even in relatively gentle terrain RTC is beneficial.

The effectiveness of RTC in minimizing power consumption can be explained by noting that for legged vehicles, it has been shown that a minimum-norm pseudo-inverse solution to the force distribution equations represents a minimum-power solution (Kumar and Waldron, 1988; Kumar and Waldron, 1990). In RTC, minimization of the

optimization criteria proposed in Equation 4.10 is essentially a minimization of the sum of the squares of the applied tractive forces, i.e. a minimum-norm solution of a subset of **x**. Thus, the two solutions are closely related. Note, however, that RTC optimization explicitly considers such factors as motor resistance, gear ratio, and wheel radius, and thus represents a more accurate measure of power consumption.
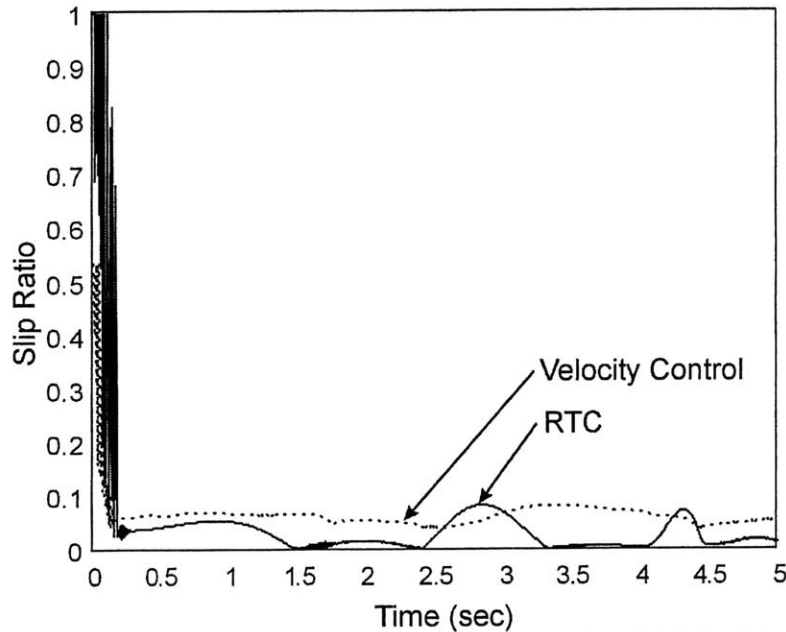


**Figure 4.7:** Average slip ratio of front and rear wheels for RTC (solid) vs. velocity controlled system (dotted)

The second simulation was the traverse of highly challenging terrain, shown in Figure 4.8. The maximum slopes in this terrain are near the internal friction angle of the soil.

The RTC system successfully completed the traverse while the velocity-controlled system did not. This is due to additional thrust force generated by the RTC algorithm, shown in Figure 4.9. The total wheel thrust generated by the RTC system remains higher than the thrust generated by the velocity-controlled system during most of the traverse. In this particular simulation the RTC system commanded increased torque to the rear wheel, which has a much higher load than the front wheel and thus a higher thrust

capacity, resulting in increased net thrust. The dual-criteria optimization remained in

traction maximization mode during the traverse.
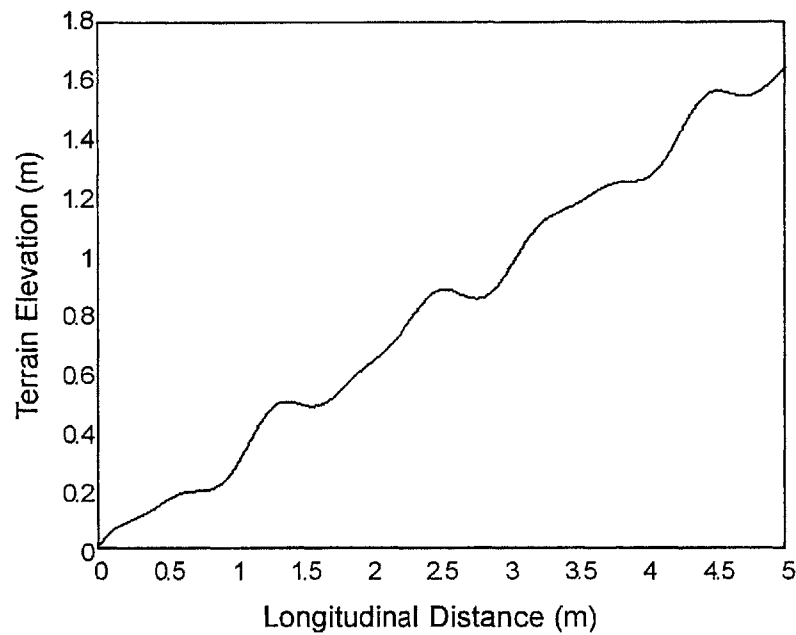


**Figure 4.8:** Simulated challenging terrain profile
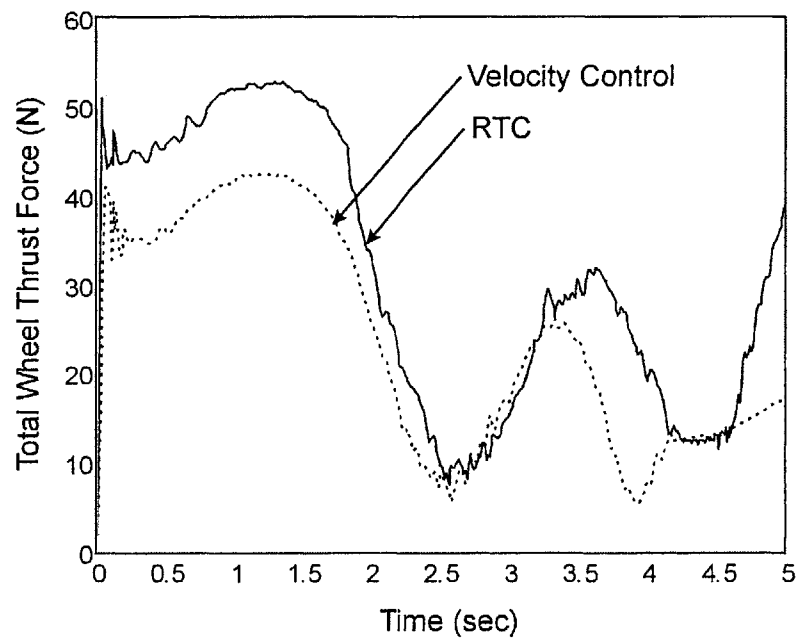


**Figure 4.9:** Total wheel thrust of RTC (solid) vs. velocity-controlled system (dotted)

The average wheel slip in the RTC system remained lower than the velocity-controlled system during most of the traverse, as seen in Figure 4.10. Note that although significant slip remained in the RTC system, this is due to the highly rough terrain.
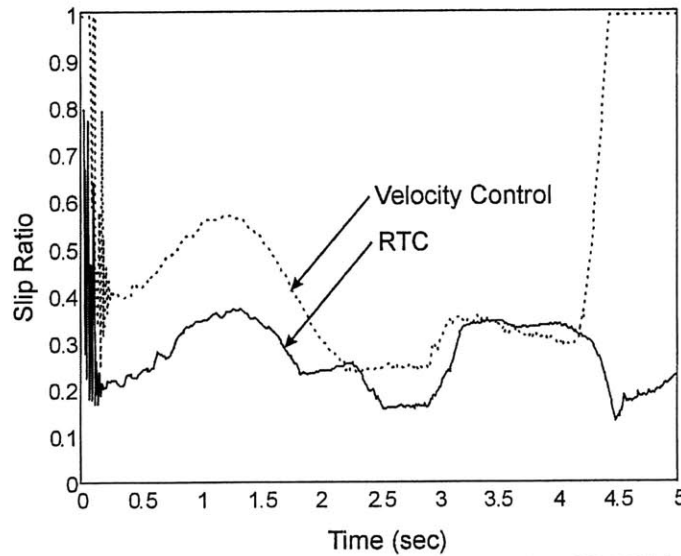


**Figure 4.10:** Average slip ratio of front and rear wheels of RTC (solid) vs. velocity-controlled system (dotted)

### 4.4.2 Experimental Results

The RTC algorithm was applied to the FSRL experimental rover operating in an indoor rough-terrain environment (see Appendix C). First, a go/no-go experiment was performed to examine the mobility improvement provided by the RTC algorithm compared to individual-wheel velocity control.

The FSRL rover was commanded to traverse a ditch covered by loose, sandy soil, shown in Figure 4.11. The maximum depth of the ditch was approximately one wheel diameter. The width of the ditch varies from approximately two to four wheel diameters. The wheel-terrain contact angles have been observed to vary greatly during traversal of the ditch (see Figure 4.12). Thus, ditch traversal is a challenging mobility task.
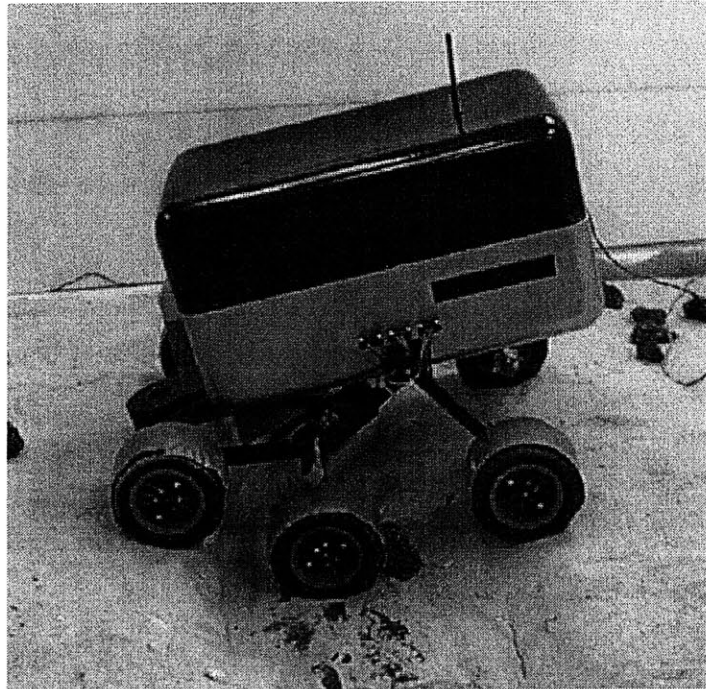
**Figure 4.11:** FSRL rover during go/no-go traversal experiment
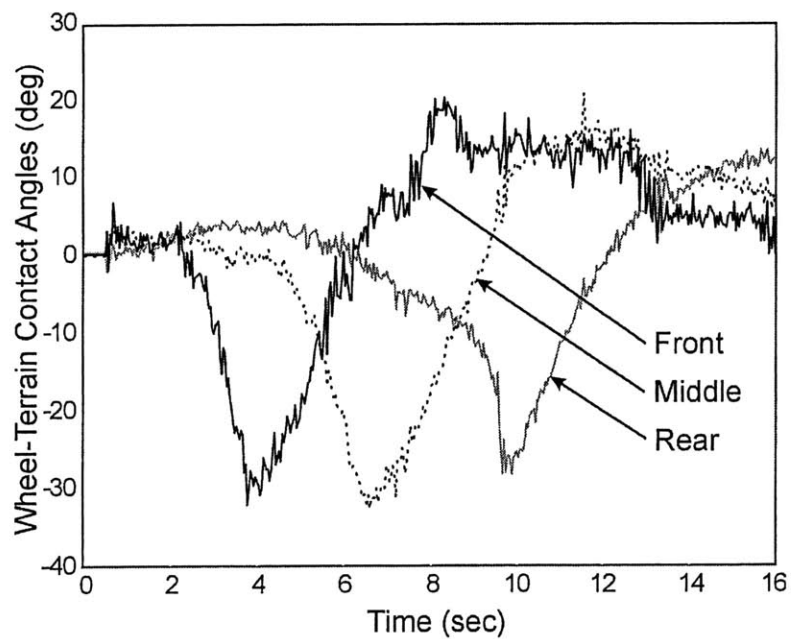


**Figure 4.12:** Wheel-terrain contact angles during ditch traversal: right front wheel (solid black), right middle wheel (dotted black), and right rear wheel (solid gray)

The ability of the RTC system to successfully traverse the ditch was compared to a velocity-controlled system over 20 trials in a go/no-go manner. It was observed that the RTC system successfully traversed the ditch 14 times out of 20, while the velocity controlled system successfully completed the traverse 6 times out of 20, an improvement of 133%. Variability in the results are due to irregularity in soil compactness and distribution, ditch traversal route, and commanded velocity (in the velocity-controlled system) and body force vector (in the RTC system).

The reason for the mobility improvement gained from RTC can be understood by examining a time history of the rover's right-side wheel-terrain normal forces during ditch traversal, shown in Figure 4.13. At time $t = 0$, when the rover is on flat terrain, it can be seen that the system weight is unevenly distributed over the wheels, with the rear wheel bearing approximately 49% of the rover weight, the middle wheel bearing 35%, and the front wheel 16%. During traversal, the normal forces vary as much as 87%, compared to their initial values.

The velocity controller applies whatever torque is necessary to achieve a desired angular velocity. This results in applied thrust that is generally either less than or greater than the maximum thrust the soil can support. If the applied thrust is less than the maximum thrust, the resulting total thrust exerted by the rover is sub-optimal. If the applied thrust is greater than the maximum soil thrust, soil failure occurs, and wheel slip results.

The RTC system, on the other hand, attempts to apply the maximum thrust the soil can support. Thus, the rear wheel (which has high normal force) is commanded greater torque than the front wheel (which has a low normal force). The resulting net vehicle

thrust is greater than the velocity-controlled system, resulting in improved rough-terrain mobility.
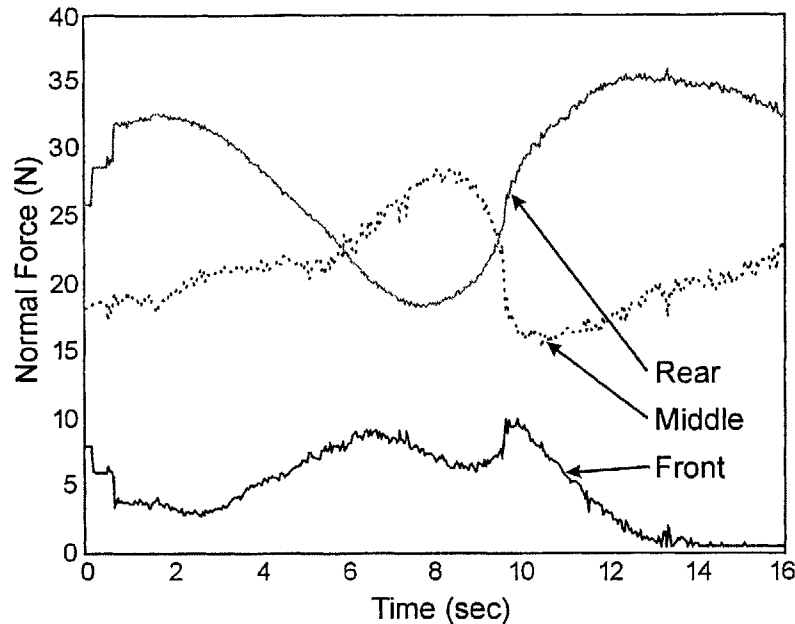


**Figure 4.13:** Estimated normal forces during ditch traversal: right front wheel (solid black), right middle wheel (dotted black), and right rear wheel (solid gray)

A second experiment was performed to quantify the thrust increase generated by the RTC algorithm compared to the velocity control algorithm. An aluminum sled was attached to a force/torque sensor mounted at the front of the FSRL rover, as shown in Figure 4.14. The force exerted on the sled was measured during the ditch traverse with a six-axis force/torque sensor (refer to Appendix C for details).

Results of a representative pair of trials are shown in Figure 4.15. It can be seen that the RTC system generated greater thrust than the velocity-controlled system during the majority of the traverse. Again, this thrust increase is due to optimization of the wheel-torque distribution by the RTC algorithm. The average thrust improvement was 82%, a substantial improvement. This thrust improvement allows a RTC-controlled rover to traverse more challenging terrain than a velocity-controlled rover.

---

*Chapter 4: How Should a Rover Do It?* 113
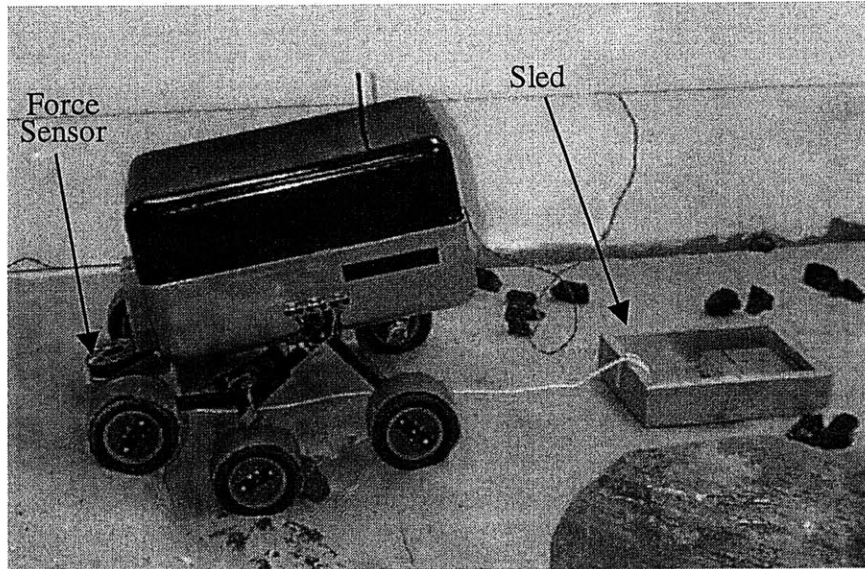
**Figure 4.14:** FSRL rover during thrust force measurement experiment
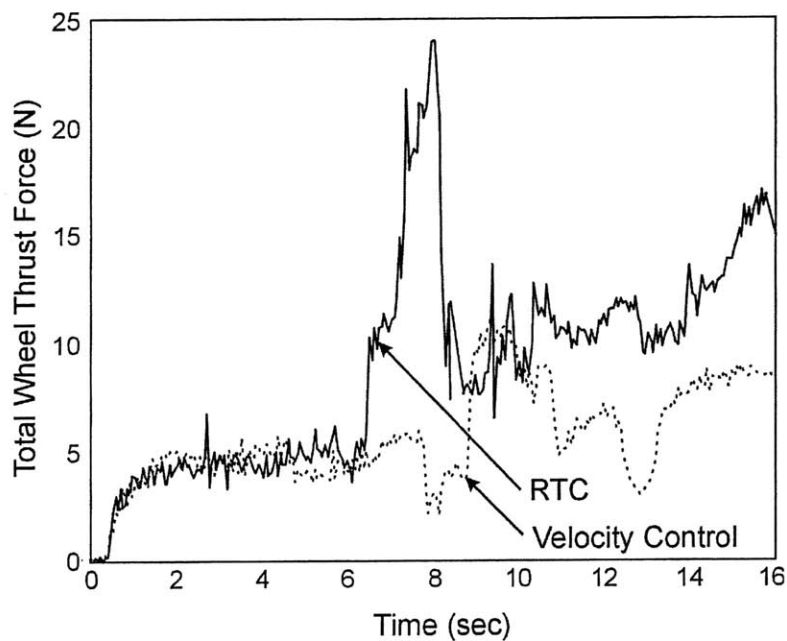


**Figure 4.15:** Thrust force during ditch traversal with rough-terrain control (solid) and velocity control (dotted)

## 4.5 Summary and Conclusions

In this chapter, a rough-terrain control (RTC) method has been presented that optimizes

force distribution for improved traction or reduced power consumption, depending on the

local terrain profile. Simulation results for a rover system operating on soft soil have shown that the RTC algorithm consumes less power and provides greater thrust than traditional individual-wheel velocity control. Experimental results on the FSRL rover testbed have shown that the RTC algorithm leads to increased mobility and thrust compared to a individual-wheel velocity control scheme.

# Chapter

# 5

# Conclusions and Suggestions for Future Work

## 5.1 Contributions of this Thesis

This thesis has investigated methods for improved mobile robot mobility in high-risk, rough-terrain environments, through the use of physical models of the rover and terrain.

In Chapter 2, a method for estimating important terrain parameters during rover motion was presented. These properties allow prediction of terrain traversability, and are critical elements of rough-terrain planning and control algorithms. An algorithm for on-line estimation of wheel-terrain contact angles was also presented. These contact angles are required for rover analysis and control. Simulation and experimental results showed that terrain parameters and wheel-terrain contact angles can be estimated on-line with good accuracy.

In Chapter 3, a rough-terrain motion planning algorithm was presented that utilizes the models and techniques presented in Chapter 2. The algorithm allows rapid, autonomous determination of a safe path through a proposed terrain region. Simulation results showed that the algorithm found shorter, safer paths than a traditional planning

method. An algorithm for geometric reconfiguration of a rover's kinematic structure was also presented. This algorithm was applied to the particular case of improving tipover stability of a reconfigurable rover in rough terrain. Simulation and experimental results showed that the algorithm substantially improved the tipover stability of the JPL SRR in rough outdoor terrain.

In Chapter 4, a rough-terrain control algorithm was presented that uses the models and techniques presented in Chapter 2. The algorithm uses a multi-criteria optimization method to maximize power efficiency or wheel traction, depending on the local terrain profile. Simulation and experimental results showed that the algorithm leads to improved performance in rough terrain, compared to traditional velocity control.

## 5.2 Suggestions for Further Work

This thesis has investigated several aspects of rough-terrain mobility. Although substantial work has been completed, further research could be conducted in several areas.

The terrain parameter estimation methodology presented in Chapter 2 is valid for the case of rigid wheels on deformable terrain. Although this is a commonly-occurring case (and is the expected case for planetary exploration rovers) it would be useful to extend the proposed approach to the case of deformable wheels in rigid or deformable terrain. Additionally, the wheel-terrain parameters are currently estimated via a simple linear regression. More sophisticated methods for parameter estimation could be investigated, such as adaptation. This could lead to improved algorithm robustness. Finally, visual

terrain cues such as color and roughness could aid parameter estimation by "focusing" the algorithm on a certain predicted range of values.

The rough-terrain planning algorithm presented in Chapter 3 is suitable for on-line implementation, but can be computationally cumbersome for large terrain maps. More efficient search algorithms, such as $D^*$, could be employed in the rapid search step to reduce computation time (Stentz, 1994). Also, the algorithm globally re-plans the path when it is deemed unsafe at any point. Local re-planning could lead to more efficient computation, although it is unclear how this would affect path optimality.

The kinematic reconfigurability algorithm presented in Chapter 3 is a general algorithm with wide applicability, but has been studied only for the specific case of tipover stability optimization. This method could be applied to other criteria, such as maximization of wheel traction.

# References

Arora, J., *Introduction to Optimum Design*, McGraw-Hill, New York, 1989

Balaram, J., "Kinematic State Estimation for a Mars Rover," *Robotica*, Volume 18, pp. 251-262, 2000

Bekker, G., *Theory of Land Locomotion*, University of Michigan Press, 1956

Bekker, G., *Introduction to Terrain-Vehicle Systems*, University of Michigan Press, 1969

Ben Amar, F., and Bidaud, P., "Dynamic Analysis of Off-Road Vehicles," *Proceedings of Fourth International Symposium on Experimental Robotics*, pp. 363-371, 1995

Bickler, D., "A New Family of JPL Planetary Surface Vehicles," *Missions, Technologies, and Design of Planetary Mobile Vehicles*, pp. 301-306, 1992

Borenstein, J., Everett, B., and Feng, L., *Navigating Mobile Robots: Systems and Techniques*, A. K. Peters Ltd., Wellesley, MA, 1996

Brown, R., and Hwang, P., *Introduction to Random Signals and Applied Kalman Filtering*, John Wiley and Sons, 1997

Burn, R., *Design of a Mars Exploration Rover*, M.S. Thesis, Massachusetts Institute of Technology, Cambridge, MA, 1997

Caurin, G., and Tschichold-Gurman, N., "The Development of a Robot-Terrain Interaction System for Walking Machines," *Proceedings of the IEEE International Conference on Robotics and Automation*, Volume 2, pp. 1013-1018, 1994

Chanclou, B., and Luciani, A., "Global and Local Path Planning in Natural Environments by Physical Modeling," *Proceedings of the International Conference on Intelligent Robots and Systems, IROS '96*, pp. 1118-1125, 1996

Cheok, K, Hoogterp, F, Fales, W., Hobayashi, K, and Scaccia, S., "Fuzzy Logic Approach to Traction Control Design," *Electronic Braking, Traction, and Stability Control*, SAE Paper Number 960957, 1997

Cherif, M., and Laugier, C., "Dealing with Vehicle/Terrain Interactions when Planning the Motions of a Rover," *IEEE International Conference on Robotics and Automation*, pp. 579-586, 1994

Cherif, M., "Kinodynamic Motion Planning for All-Terrain Wheeled Vehicles," *IEEE International Conference on Robotics and Automation*, pp. 317-322, 1999

Chottiner, J., *Simulation of a Six-Wheeled Martian Rover Called the Rocker-Bogie*, M.S. Thesis, The Ohio State University, Columbus, OH, 1992

Choi, B., and Sreenivasan, S., "Motion Planning of A Wheeled Mobile Robot with Slip-Free Capability on a Smooth Uneven Surface," *Proceedings of the IEEE International Conference on Robotics and Automation*, pp. 3727-3732, 1998

Chung, W., and Waldron, K., "Force Distribution by Optimizing Angles for Multifinger Systems," *Proceedings of the IEEE International Conference on Robotics and Automation*, Volume 3, pp. 717-722, 1993

Dubowsky, S., Moore, C., and Sunada, C., "On the Design and Task Planning of Power-Efficient Field Robotic Systems," *Proceedings of the Sixth ANS Robotics and Remote Systems Conference*, 1995

Duff, I., Erisman, A., and Reid, J., *Direct Methods for Sparse Matrices*, Oxford University Press, New York, NY, 1986

Eckhardt, H., *Kinematic Design of Machines and Mechanisms*, McGraw-Hill, New York, NY, 1989

Farritor, S., Hacot, H., and Dubowsky, S., "Physics-Based Planning for Planetary Exploration," *Proceedings of the IEEE International Conference on Robotics and Automation*, pp. 278-83, 1998 (a)

Farritor, S., *On Modular Design and Planning for Field Robotic Systems*, Ph.D. Thesis, Massachusetts Institute of Technology, Cambridge, MA, 1998 (b)

Gifford, K., and Murphy, R., "Incorporating Terrain Uncertainties in Autonomous Vehicle Path Planning," *Proceedings of the International Conference on Intelligent Robots and Systems, IROS '96*, pp. 1134-1140, 1996

Golombek, M. P., "Mars Pathfinder Mission and Science Results," *Proceedings of the 29th Lunar and Planetary Science Conference*, 1998

Hacot, H., *Analysis and Traction Control of a Rocker-Bogie Planetary Rover*, M.S. Thesis, Massachusetts Institute of Technology, Cambridge, MA, 1998

Haddad, H., Khatib, M., Lacroix, S., and Chatila, R., "Reactive Navigation in Outdoor Environments using Potential Fields," *Proceedings of IEEE International Conference on Robotics and Automation*, pp. 1232-1236, 1998

Hait, A., and Simeon, T., "Motion Planning on Rough Terrain for an Articulated Vehicle in Presence of Uncertainties," *IEEE/RSJ International Symposium on Intelligent Robots and Systems*, pp. 1126-1133, 1996

Hayati, S., Volpe, R., Backes, P., Balaram, J., and Welch, W., "Microrover Research for Exploration of Mars," *AIAA Forum on Advanced Developments in Space Robotics*, 1996

Hebert, M., and Krotkov, E., "3D Measurements from Imaging Laser Radars," *Image and Vision Computing,* Volume 10, Number 3, pp. 170-178, 1992

Hung, M., Orin., D., and Waldron, K., "Force Distribution Equations for General Tree-Structured Robotic Mechanisms with a Mobile Base," *Proceedings of IEEE International Conference on Robotics and Automation,* pp. 2711-2716, 1999

Huntsberger, T, Baumgartner, E., Aghazarian, H., Cheng, Y., Schenker, P., Leger, P., Iagnemma, K., and Dubowsky, S., "Sensor Fused Autonomous Guidance of a Mobile Robot and Applications to Mars Sample Return Operations," *Proceedings of the SPIE Symposium on Sensor Fusion and Decentralized Control in Robotic Systems II*, Volume 3839, 1999

Iagnemma, K., Genot, F., and Dubowsky, S., "Rapid Physics-Based Rough-Terrain Rover Planning with Sensor and Control Uncertainty," *Proceedings of the 1999 IEEE International Conference on Robotics and Automation*, Detroit, 1999 (a)

Iagnemma, K., Burn, R., Wilhelm, E., and Dubowsky, S., "Experimental Validation of Physics-Based Planning and Control Algorithms for Planetary Robotic Rovers," *Proceedings of the Sixth International Symposium on Experimental Robotics, ISER '99,* 1999 (b)

Iagnemma, K., and Dubowsky, S., "Vehicle Wheel-Ground Contact Angle Estimation: with Application to Mobile Robot Traction Control," $7^{th}$ *International Symposium on Advances in Robot Kinematics, ARK '00,* 2000 (a)

Iagnemma, K., and Dubowsky, S., "Mobile Robot Rough-Terrain Control (RTC) for Planetary Exploration," *Proceedings of the 26th ASME Biennial Mechanisms and Robotics Conference, DETC 2000,* 2000 (b)

Iagnemma, K., Rzepniewski, A., Dubowsky, S., Huntsberger, T., Pirjanian, P., Schenker, P., "Mobile Robot Kinematic Reconfigurability for Rough-Terrain," *Proceedings of the SPIE Symposium on Sensor Fusion and Decentralized Control in Robotic Systems III,* 2000 (c)

Kelly, A., and Stentz, A., "Rough Terrain Autonomous Mobility—Part 2: An Active Vision, Predictive Control Approach," *Autonomous Robots,* Volume 5, pp. 163-198, 1998

Kumar, V., and Waldron, K., "Force Distribution in Closed Kinematic Chains," *IEEE Transactions on Robotics and Automation,* Volume 4, Number 6, pp. 657-644, 1988

Kumar, V., and Waldron, K., "Actively Coordinated Vehicle Systems," *ASME Journal of Mechanisms, Transmissions, and Automation in Design,* Volume 111, pp. 223-231, 1989

Kumar, V., and Gardner, J., "Kinematics of Redundantly Actuated Closed Chains," *IEEE Transactions on Robotics and Automation,* Volume 6, Number 2, pp. 269-274, 1990

Kumar, V., and Waldron, K., "Force Distribution in Walking Vehicles," *ASME Journal of Mechanical Design,* Volume 112, pp. 90-99, 1990

Latombe, J. C., *Robot Motion Planning,* Kluwer Academic Publishers, 1991

Laubach, S., Burdick, J., and Matthies, L., "An Autonomous Path Planner Implemented on the Rocky7 Prototype Microrover," *Proceedings of the IEEE International Conference on Robotics and Automation*, pp. 292-297, 1998

Laubach, S., and Burdick, J., "An Autonomous Sensor-Based Path Planner for Microrovers," *Proceedings of the IEEE International Conference on Robotics and Automation*, pp. 347-354, 1999

Le, A., Rye, D., and Durrant-Whyte, H., "Estimation of Track-Soil Interactions for Autonomous Tracked Vehicles," *Proceedings of the IEEE International Conference on Robotics and Automation*, pp. 1388-1393, 1997

Lee, H., and Tomizuka, M., "Adaptive Vehicle Traction Force Control for Intelligent Vehicle Highway Systems (IVHS)," *Proceedings of the ASME Conference on Dynamics, Systems, and Control*, pp. 17-24, 1996

Linderman, R., and Eisen H., "Mobility Analysis, Simulation, and Scale Model Testing for the Design of Wheeled Planetary Rovers," *Missions, Technologies, and Design of Planetary Mobile Vehicles*, pp. 531-537, 1992

Matijevic, J., Crisp, J., Bickler, D., Banes, R., Cooper, B., Eisen, H., Gensler, J., Haldemann, A., Hartman, F., Jewett, K., Matthies, L., Laubach, S., Mishkin, A., Morrison, J., Nguyen, T., Sirota, A., Stone, H., Stride, S., Sword, L., Tarsala, J., Thompson, A., Wallace, M., Welch, R., Wellman, E., Wilcox, B., "Characterization of Martian Surface Deposits by the Mars Pathfinder Rover, Sojourner," *Science*, Volume 278, Number 5, pp. 1765-1768, 1997 (a)

Matijevic, J., "Sojourner: The Mars Pathfinder Microrover Flight Experiment," *Space Technology*, Volume 17, Number 3/4, pp. 143-149, 1997 (b)

Matijevic, J., "'01 Surveyor Rover: Requirements, Constraints, and Challenges," NASA Internal Document, 1997 (c)

Matthies, L., and Grandjean, P., "Stochastic Performance Modeling and Evaluation of Obstacle Detectability with Imaging Range Sensors," *IEEE Transactions on Robotics & Automation*, Volume 10, Number 6, pp. 783-92, 1994

Mauer, G. "A Fuzzy Logic Controller for an ABS Braking System," *IEEE Transactions on Fuzzy Systems,* Volume 3, Number 4, pp. 381-387, 1995

Matthies, L., Gat, E., Harrison, R., Wilcox, B., Volpe, R., Litwin, T., "Mars Microrover Navigation: Performance Evaluation and Enhancement," *Autonomous Robots*, Volume 2, Number 4, 1995

Milesi-Bellier, C., Laugier, C., and Faverjon, B., "A Kinematic Simulator for Motion Planning of a Mobile Robot on a Terrain," *Proceedings of the International Conference on Intelligent Robots and Systems, IROS '93*, pp. 339-343, 1993

Mishkin, A., Morrison, J., Nguyen, T., Stone, H., Cooper, B., and Wilcox, B., "Experiences with Operations and Autonomy of the Mars Pathfinder Microrover," *Proceedings of the 1998 IEEE Aerospace Conference*, pp. 337-51, 1998

Mohan, S., and Williams, R., "A Survey of 4WD Traction Control Strategies," *Electronic Braking, Traction, and Stability Control,* SAE Paper Number 952644, 1997

NASA Technical Memorandum 100470, "Environment of Mars, 1988," Lyndon B. Johnson Space Center, 1988

Nilsson, N., *Principles of Artificial Intelligence*, Tioga Publishing Company, 1980

Nohse, Y., Hashuguchi, K., Ueno, M., Shikanai, T., Izumi, H., and Koyama, F., "A Measurement of Basic Mechanical Quantities of Off-The-Road Traveling Performance," *Journal of Terramechanics*, Volume 28, Number 4, pp. 359-371, 1991

Olin, K., and Tseng, D., "Autonomous Cross-Country Navigation," *IEEE Expert*, Volume 6, Number 4, pp. 16-30, 1991

Onafko, O., and Reece, A., "Soil Stresses and Deformation Beneath Rigid Wheels", *Journal of Terramechanics*, Volume 4, Number 1, pp. 59-80, 1967

Osborn, J.F., "Applications of Robotics in Hazardous Waste Management," *Proceedings of the SME 1989 World Conference on Robotics Research*, 1989

Page, L, and Sanderson, A., "Robot Motion Planning for Sensor-Based Control with Uncertainties," *Proceedings of the IEEE International Conference On Robotics and Automation*, pp. 1333-1340, 1996

Pai, D., and Reissel, L.-M., "Multiresolution Rough Terrain Motion Planning," *IEEE Transactions on Robotics and Automation*, Volume 14, Number 1, pp. 19-33, 1998

Papadopoulos, E. and Rey, D., "A New Measure of Tipover Stability Margin for Mobile Manipulators," *Proceedings of the IEEE International Conference On Robotics and Automation*, 1996

Pickover, C., "Generating Extraterrestrial Terrain," *IEEE Computer Graphics and Applications*, Volume 15, Number 2, 1995

Plackett, C., "A Review of Force Prediction Methods for Off-Road Wheels," *Journal of Agricultural Engineering Research*, Volume 31, pp. 1-29, 1985

Reister, D., Unseren, M., "Position and Constraint Force Control of a Vehicle with Two or More Steerable Drive Wheels," *IEEE Transactions on Robotics and Automation,* Volume 9, pp. 723-731, 1993

Schenker, P., Sword, L., Ganino, A., Bickler, D., Hickey, G., Brown, D., Baumgartner, E., Matthies, L., Wilcox, B., Balch, T., Aghazarian, H., and Garrett, M., "Lightweight Rovers for Mars Science Exploration and Sample Return," *Proceedings of SPIE XVI Intelligent Robots and Computer Vision Conference,* Volume 3208, pp. 24-36, 1997

Schenker, S. Trebi-Ollennu, A., Balaram, J., Pirjanian, P., Huntsberger, T., Baumgartner, E., Aghazarian, H., Kennedy, B., Dubowsky, S., Apostolopoulos, D., Leger, P., McKee, G., "Reconfigurable Robots for All-Terrain Exploration," *Proceedings of the SPIE Symposium on Sensor Fusion and Decentralized Control in Robotic Systems III,* 2000

Schiller, Z., and Chen, J., "Optimal Motion Planning of Autonomous Vehicles in 3-Dimensional Terrains," *IEEE International Conference on Robotics and Automation,* pp. 198-203, 1990

Seraji, H., "Traversability Index: A New Concept for Planetary Rovers, *IEEE International Conference on Robotics and Automation,* 1999

Shibly, H., Iagnemma., K, and Dubowsky, S., *Real-Time Soil Characterization by Planetary Vehicles,* Field and Space Robotics Laboratory Internal Report Number 8-00-1, Massachusetts Institute of Technology, 2000

Shmulevich, I., Ronai, D., and Wolf, D., "A New Field Single Wheel Tester," *Journal of Terramechanics,* Volume 33, Number 3, pp. 133-141, 1996

Siméon, T., and Dacre-Wright, B., "A Practical Motion Planner for All-terrain Mobile Robots," *IEEE International Conference on Intelligent Robots and Systems*, pp. 1357-1363, 1993

Sreenivasan, S., *Actively Coordinated Wheeled Vehicle Systems*, Ph.D. Thesis, The Ohio State University, Columbus, OH, 1994

Sreenivasan, S., and Wilcox, B., "Stability and Traction Control of an Actively Actuated Micro-Rover," *Journal of Robotic Systems*, Volume 11, Number 6, pp. 487-502, 1994

Sreenivasan, S., and Nanua, P, "Kinematic Geometry of Wheeled Vehicle Systems," *Proceedings of the ASME Design Engineering Technical Conferences*, 1996

Sreenivasan, S., and Waldron, K., "Displacement Analysis of an Actively Articulated Wheeled Vehicle Configuration with Extensions to Motion Planning on Uneven Terrain," *Transactions of the ASME Journal of Mechanical Design*, Volume 118, pp. 312-317, 1996

Stentz, A., "Optimal and Efficient Path Planning for Partially-Known Environments," *Proceedings of the IEEE International Conference on Robotics and Automation*, pp. 3310-3317, 1994

Tan, H., and Chin, Y., "Vehicle Traction Control: Variable-Structure Control Approach," *ASME Journal of Dynamic Systems, Measurement, and Control*, Volume 113, pp. 223-230, 1991

Tan, H., and Chin, Y., "Vehicle Antilock Braking and Traction Control: A Theoretical Study," *International Journal of Systems Science*, Volume 23, Number 3, pp. 351-365, 1992

Tarokh, M., McDermott, G., Hayati, S., and Hung, J., "Kinematic Modeling of a High Mobility Mars Rover," *IEEE International Conference on Robotics and Automation,* pp. 992-998, 1999

Van Zanten, A., Erhardt, R., and Pfaff, G., "VDC, The Vehicle Dynamics Control System of Bosch," *Electronic Braking, Traction, and Stability Control,* SAE Paper Number 950759, 1997

Van Zanten, A., Erhardt, R., Landesfiend, K., and Pfaff, G., "VDC Systems Development and Perspective," SAE Paper Number 980235, *Electronic Braking, Traction, and Stability Control,* 1998

Vincent, E. "Pressure Distribution on and Flow of Sand Past a Rigid Wheel, *Proceedings of the First International Conference on Terrain-Vehicle Systems,* pp. 859-877, 1961

Vlassis, N., and Tsanakas, P., "A Sensory Uncertainty Field Model for Unknown and Non-stationary Mobile Robot Environments," *Proceedings of the IEEE International Conference on Robotics and Automation,* pp. 363-368, 1998

Volpe, R., "Navigation Results from Desert Field Tests of the Rocky 7 Mars Rover Prototype," *International Journal of Robotics Research,* Volume 18, Number 7, 1999

Warren, C., "Fast Path Planning Using Modified $A^*$ Method," *Proceedings of the IEEE International Conference on Robotics and Automation,* pp. 662-667, 1993

Welch, G., and Bishop, G., "An Introduction to the Kalman Filter," Technical Report TR 95-041, Department of Computer Science, University of North Carolina at Chapel Hill, 1999

---

Wilhelm, E., *Design of a Wireless Control System for a Laboratory Planetary Rover*, B.S. Thesis, Massachusetts Institute of Technology, Cambridge, MA, 1998

Wong, J., and Reece, A, "Prediction of Performance of Driven Rigid Wheels, Part I," *Journal of Terramechanics,* Volume 4, Number 1, pp. 81-98, 1967

Wong, J., *Theory of Ground Vehicles*, John Wiley and Sons, 1993

Yahja, A., Stentz, A., Singh, S., and Brumitt, B., "Framed-Quadtree Path Planning for Mobile Robots Operating in Sparse Environments," *Proceedings of the 1998 IEEE International Conference on Robotics and Automation,* 1998

Zhang, H., Kumar, V., and Ostrowski, J., "Motion Planning With Uncertainty," *Proceedings of the IEEE International Conference on Robotics and Automation,* pp. 638-643, 1998

# Appendix A

# Rover Kinematic and Force Analyses

*Kinematic Analysis*

In this appendix a kinematic analysis of a six-wheeled rover with a rocker-bogie suspension is presented. Details of rocker-bogie suspension characteristics can be found in (Bickler, 1992). Kinematic modeling of articulated mobile robots has been studied by numerous researchers, as described in Section 1.3.1. This thesis does not attempt to make a fundamental contribution to kinematic modeling. However, this model will form a basis for further analysis and is included for completeness.

This analysis assumes that wheel-terrain contact occurs at a point. This is a reasonable assumption for rigid wheels travelling on firm terrain. For rigid wheels on soft terrain, the wheel-terrain contact "patch" can be resolved to an effective contact point for the purposes of kinematic analysis. Note that the vehicles considered in this thesis, such as planetary exploration rovers, generally possess rigid wheels.

To fully define the rover configuration, ten parameters are required:

- The position of the center of the body $\mathbf{p}_c = [p_x \ p_y \ p_z]^T$ expressed in an inertial frame *{XYZ}*.

- The orientation (i.e. the roll, pitch, and yaw) of the rover body *($\Theta$, $\Phi$, $\Psi$)* expressed in *{XYZ}*.

- The configuration parameters of the rocker-bogie mechanism *($\theta_{1r}$, $\theta_{2r}$, $\theta_{1l}$, $\theta_{2l}$)*.

The inverse kinematics problem for this rover can be stated as follows: *Given the shape of the terrain and the position of the center of the body* $p_c$ *expressed* {XYZ}, *compute the orientation* ($\Theta$, $\Phi$, $\Psi$) *of the rover body and the configuration* ($\theta_{1r}$, $\theta_{2r}$, $\theta_{1l}$, $\theta_{2l}$) *of the rover suspension.*
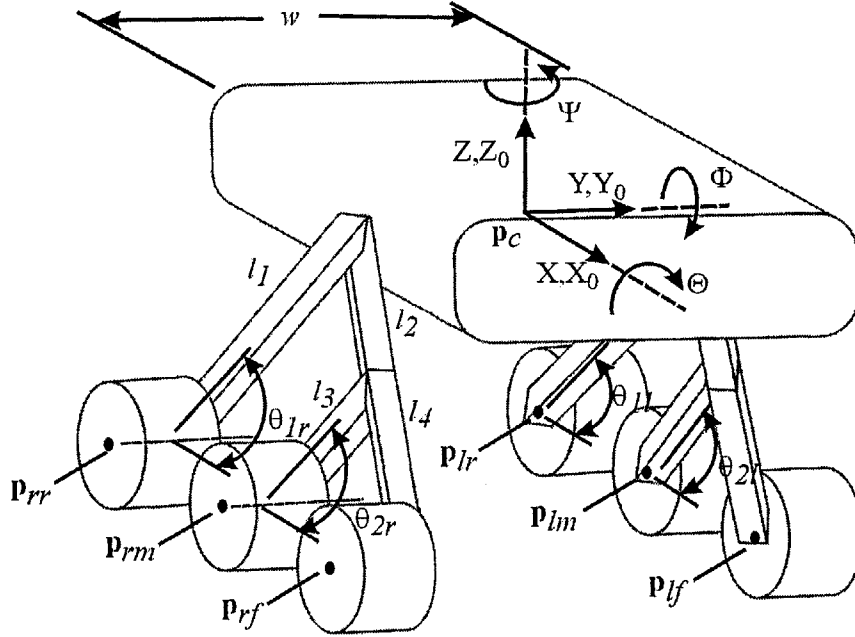


**Figure A.1**: Kinematic description of a six-wheeled rover

For a vehicle with $m$ unique wheel-terrain contact points, at least $m$-1 kinematic loop closure equations can be written (Eckhardt, 1989). For the rover shown in Figure A.1, these loop closure equations are:

$$z_{rr} = z_{lr} + l_1 \cos\Theta\left(\sin\theta_{1r} - \sin\theta_{1l}\right) + w\sin\Theta \qquad (A.1)$$

$$z_{rr} = z_{lm} + \cos\Theta\left(l_1 \sin\theta_{1r} - l_2 \cos\theta_{1l} - l_3 \sin\theta_{2l}\right) + w\sin\Theta \qquad (A.2)$$

$$z_{rr} = z_{lf} + \cos\Theta\left(l_1 \sin\theta_{1r} - l_2 \cos\theta_{1l} - l_4 \cos\theta_{2l}\right) + w\sin\Theta \qquad (A.3)$$

$$z_{rr} = z_{rm} + \cos\Theta\left(l_1 \sin\theta_{1r} - l_2 \cos\theta_{1r} - l_3 \sin\theta_{2r}\right) \qquad (A.4)$$

$$z_{rr} = z_{rf} + \cos\Theta\left(l_1 \sin\theta_{1r} - l_2 \cos\theta_{1r} - l_4 \cos\theta_{2r}\right) \qquad (A.5)$$

where $z_{ij}$, $i = \{r,l\}$, $j = \{r,m,f\}$ refers to the $z$ component of $\mathbf{p}_{ij}$, with index $i$ referring to the right or left side, and index $j$ referring to the rear, middle, or front wheel.

Due to the mechanical differential in this system, an additional equation can be written relating the pitch $\Phi$ to the angles $\theta_{lr}$ and $\theta_{ll}$:

$$\Phi = \frac{\theta_{lr} + \theta_{ll}}{2} + \theta'_{lr} \qquad (A.6)$$

where $\theta'_{lr}$ is the value of $\theta_{lr}$ when the rover is on flat terrain. Thus, six unique kinematic equations can be written for the rover in Figure 2.1.

Inputs to the problem are assumed to be a terrain elevation map, the position $\mathbf{p}_c$ of the rover center, and the rover heading $\Psi$. Position and heading are taken as inputs since the goal of kinematic analysis is predicting the traversability and stability at a given point in the terrain (i.e. the rover will be "placed" at a point in the terrain map, and kinematic analysis will be performed). These inputs reduce the number of unknown parameters to six, which can be determined by solving the system of nonlinear equations of Equations (A.1-A.6).

Numerical techniques such as Newton's method and steepest descent can be applied to this problem, although convergence is not guaranteed since the terrain elevation map is generally not represented by a continuously differentiable function (Hacot, 1998). An efficient solution method for rover inverse kinematics has been presented in (Hacot, 1998).

In this section a force analysis of a six-wheeled rover with a rocker-bogie suspension is presented. Force analyses of articulated mobile robots have been performed by numerous researchers, as described in Section 1.3.1. This thesis does not attempt to make a fundamental contribution to mobile robot force analysis. However, this model will form a basis for further analysis and is included for completeness.

In this analysis it is again assumed that wheel-terrain contact occurs at a single point. The validity of this assumption was discussed in Section 2.5. It is also assumed that no moments exist at the wheel-terrain contact points, a reasonable assumption for natural terrain (Bekker, 1969).

Figure A.2 is a diagram of a six-wheeled mobile robot on uneven terrain. The vectors $\mathbf{f}_i = [f_i^x\, f_i^y\, f_i^z]^T$, $i = \{1,...,6\}$, represent wheel-terrain interaction forces and are expressed in the inertial frame $\{XYZ\}$. The vectors $\mathbf{p}_i = [p_i^x\, p_i^y\, p_i^z]^T$, $i = \{1,...,6\}$, are directed from the wheel-terrain contact points to the rover center of mass and are also expressed in the inertial frame $\{XYZ\}$. The vector $\mathbf{f}_s = [F_s^x\, F_s^y\, F_s^z\, M_s^x\, M_s^y\, M_s^z]^T$ at the rover center of mass represents the summed effects of gravitational forces, inertial forces, forces due to manipulation, and forces due to interaction with the environment or other robots. Note that rover link, wheel and body masses are lumped at the center of mass. Note also that $\mathbf{f}_s$ possesses a user-specified component in the direction of desired motion. Thus, if a set of wheel-terrain interaction force vectors $\mathbf{f}_i$ can be found that balance the body force vector $\mathbf{f}_s$, the rover can move in the direction of desired motion.
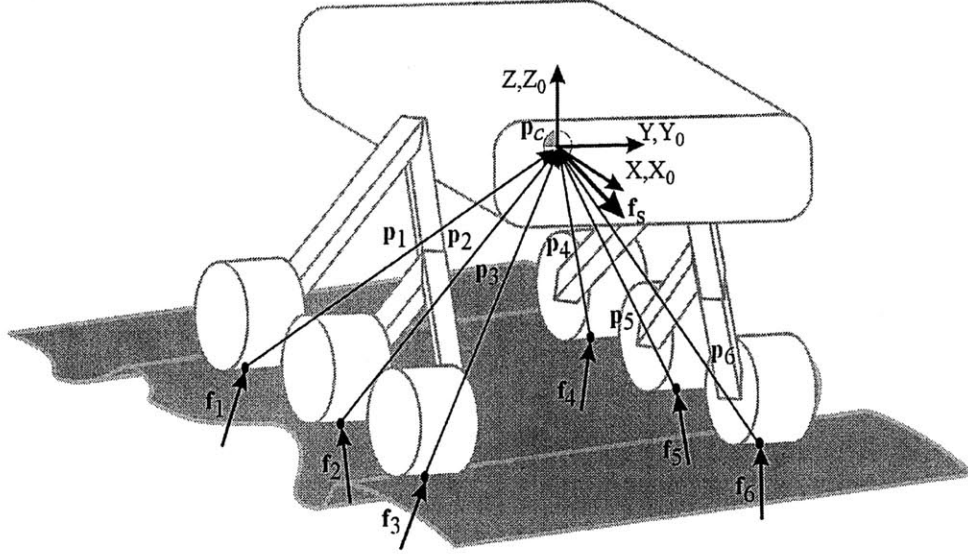
**Figure A.2**: Force analysis of a six-wheeled rover in rough terrain

A set of quasi-static force balance equations for the six-wheeled rover shown in Figure A.2 can be written as:

$$
\begin{bmatrix}
 & \mathbf{I} & & \vdots & \cdots & \vdots & & \mathbf{I} & \\
\hline
0 & p_1^z & p_1^y & & & & 0 & p_6^z & p_6^y \\
-p_1^z & 0 & -p_1^x & & \cdots & & -p_6^z & 0 & -p_6^x \\
-p_1^y & p_1^x & 0 & & & & -p_6^y & p_6^x & 0
\end{bmatrix}
\begin{bmatrix}
\mathbf{f}_1 \\
\vdots \\
\mathbf{f}_6
\end{bmatrix}
= \mathbf{f}_s
\qquad (A.7)
$$

where $\mathbf{I}$ represents a 3 x 3 identity matrix. This set of equations can be written in compact matrix form as:

$$
\mathbf{G}\mathbf{x} = \mathbf{f}_s \qquad (A.8)
$$

where $\mathbf{x} = [\mathbf{f}_1 \ \mathbf{f}_2 \ \mathbf{f}_3 \ \mathbf{f}_4 \ \mathbf{f}_5 \ \mathbf{f}_6]^T$.

Equation set (A.8) is generally referred to as the force distribution equations (Hung *et al.*, 1999). This set of equations represents 6 equations in 18 unknowns. Thus, the force analysis problem is underconstrained, and there exists an infinite set of wheel-terrain

contact force vectors $\mathbf{f}_i$ that balance the body vector $\mathbf{f}_s$. In general, a force analysis of an $m$-wheeled rover will yield six equations in $3m$ unknowns, and thus the force analysis problem will be underconstrained except for the trivial case of a two-wheeled vehicle.

Solutions of the force distribution equations must obey the system physical constraints. The first physical constraint requires that all wheels remain in contact with the terrain, or equivalently that the wheel-terrain interaction force vector components normal to the terrain remain positive:

$$N_i > 0, \quad \forall i, \ i = \{1,...,n\} \tag{A.9}$$

where $N_i$ refers to the component of $\mathbf{f}_i$ normal to the terrain at the wheel-terrain contact point (see Figure A.3).
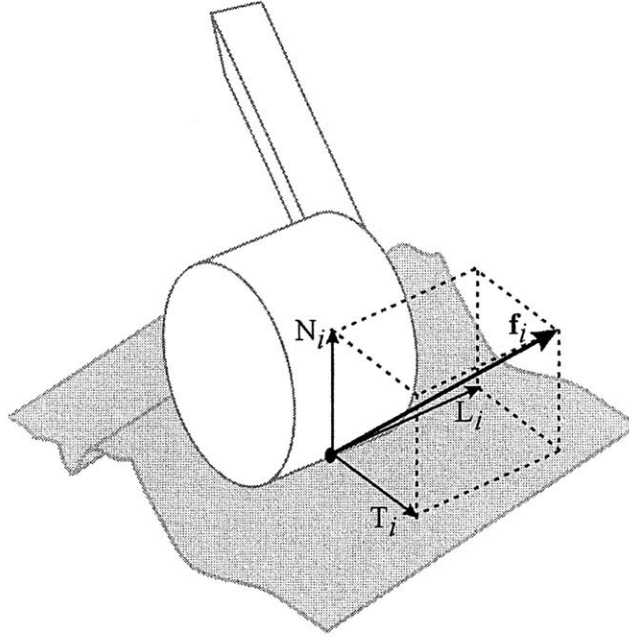


**Figure A.3**: Decomposition of wheel-terrain contact force vector

The second physical constraint requires that all joint torques remain within the saturation limits of the actuator, or:

$$\tau_i^{\min} \le (T_i \cdot r_i) \le \tau_i^{\max} \tag{A.10}$$

where $T_i$ refers to the component of $\mathbf{f}_i$ tangent to the wheel at the wheel-terrain contact point (i.e. the tractive force).

The third physical constraint requires that the tractive force exerted on the terrain not exceed the maximum shearing force the terrain can bear. If the applied shear force exceeds the allowable force, soil failure and excessive wheel slip will result. The maximum shearing force can be determined from Mohr-Coulomb theory and knowledge of soil parameters (see Chapter 2) as:

$$T^m = A(c + \sigma_m \tan\phi) \tag{A.11}$$

where $A$ is the wheel projected area and is a function of the wheel width and sinkage. Thus a constraint can be written as:

$$-T_i^m \leq T_i \leq T_i^m \tag{A.12}$$

The force analysis problem therefore involves determining if a set of wheel-terrain contact force vectors $\mathbf{f}_i$ exist that balance the body vector $\mathbf{f}_s$ subject to the above constraints. If no contact force vectors exist, the terrain is untraversable. The larger the solution space of wheel-terrain contact force vectors, the greater the probability that the terrain is traversable.

In this thesis, a brute-force analysis of the size of the solution space is performed due to its low dimension. If the solution space is larger than a pre-defined minimum value, the terrain is considered traversable.

Analysis of the size of the solution space has been performed for a rocker-bogie rover (Hacot, 1998). Figure A.3 shows an example solution space for a planar analysis of a rocker-bogie rover. In this figure the solution free variables are the wheel-terrain tractive force components $T_1$ and $T_2$. Sample constraints are shown, similar to Equations (A.9-

A.12). It can be seen that the solution space is finite and large. Thus, a set of solutions to the force distribution equations exists and the terrain region in question is traversable.
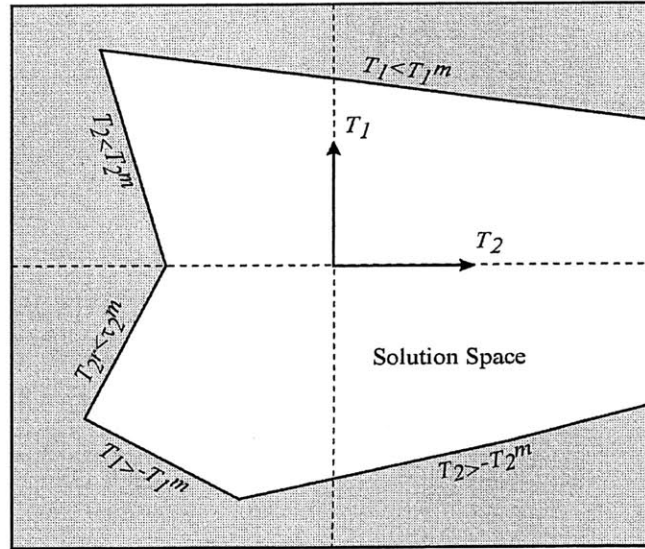


**Figure A.4**: Example solution space of force distribution equations

A final aspect of the force analysis that must be considered is the lateral stability of the vehicle. For a wheeled vehicle, only forces in the wheel plane (i.e. $T_i$ and $N_i$ (see Figure A.3)) can be controlled. The lateral forces $L_i$ are uncontrollable. These lateral forces are critical to vehicle stability in certain cases, such as traversal of an inclined surface where vehicle stability is threatened by transverse slippage. Thus it is important to be able to predict when lateral forces may compromise vehicle stability.

A method for computing $L_i$ by modeling lateral wheel-terrain interaction as compliant elements has been proposed (Hacot, 1998). Physically, this compliance can be related to the combined effects of wheel compliance and soil compaction. When the computed transverse force exceeds the maximum allowable force at the wheel-terrain interface, sliding will occur. Computation of the maximum allowable lateral force can again be

determined from Mohr-Coulomb theory and knowledge of soil parameters (see Chapter 2) as:

$$L^m = A(c + \sigma_m \tan\phi) \tag{A.13}$$

If a wheel lateral force $L_i$ exceeds the maximum lateral force $L^m$, slippage at that wheel will occur. If multiple wheels slip transversely the rover may slide uncontrollably.

# Appendix B

# Wheel-Terrain Characterization Equations

This appendix contains simplified forms of the equations for weight $W$, torque $T$, and drawbar pull $DP$ from Section 2.3.1.

The simplified exponential form of Equation (2.20) can be used to reformulate Equations (2.27-2.29), as:

$$
\begin{aligned}
\frac{W}{rb} = & \, c\left(1 - \frac{1}{g^2+1}\left(g^2\cos\theta_1 + g\sin\theta_1 + e^{-f}\right)\right) + \\
& \frac{\sigma_m}{\theta_m(\theta_1 - \theta_m)}\left(\theta_1\cos\theta_m - \theta_m\cos\theta_1 - \theta_1 + \theta_m\right) + \\
& \frac{\sigma_m\tan\phi}{\theta_m(\theta_1 - \theta_m)}\left(\theta_1\sin\theta_m - \theta_m\sin\theta_1\right) + \frac{\sigma_m\tan\phi}{\theta_m(\theta_1 - \theta_m)(g^2+1)^2} \\
& \left(\begin{array}{l} -\left(g^2-1\right)\left(\theta_m\sin\theta_1 - \theta_1\sin\theta_m e^{-f\left(1-\frac{\theta_m}{\theta_1}\right)}\right) + \\ 2g\left(\left(\theta_m\cos\theta_1 - \theta_1\cos\theta_m e^{-f\left(1-\frac{\theta_m}{\theta_1}\right)}\right) + e^{-f}(\theta_1 - \theta_m)\right) \end{array}\right)
\end{aligned} \qquad (B.1)
$$

---

$$\frac{H}{rb} = c\left(\frac{g}{g^2+1}\left(g\cos\theta_1 - \cos\theta_1 + e^{-f}\right)\right) +$$

$$\sigma_m \tan\phi \left(\begin{array}{c} \dfrac{1}{\theta_m(\theta_1-\theta_m)}\left(\theta_1\cos\theta_m - \theta_m\cos\theta_1 - \theta_1 + \theta_m\right) - \dfrac{1}{\theta_m(\theta_1-\theta_m)(g^2+1)^2} \\[4mm] \left(\begin{array}{c} \left(g^2-1\right)\left(\theta_m\cos\theta_1 - \theta_1\cos\theta_m e^{-f\left(1-\frac{\theta_m}{\theta_1}\right)}\right) \\[4mm] + 2g\left(\theta_m\sin\theta_1 - \theta_1\sin\theta_m e^{-f\left(1-\frac{\theta_m}{\theta_1}\right)}\right) + e^{-f}\left(g^2-1\right)(\theta_1-\theta_m) \end{array}\right) \end{array}\right) \qquad \text{(B.2)}$$

$$\frac{R}{rb} = \frac{\sigma_m}{\theta_m(\theta_1-\theta_m)}\left(\theta_1\sin\theta_m - \theta_m\sin\theta_1\right) \qquad \text{(B.3)}$$

$$\frac{T}{r^2b\theta_1} = c\left(1 - \frac{1-e^{-f}}{f}\right) + \sigma_m\tan\phi\left(\begin{array}{c}\left(\dfrac{1}{2} - \left(\dfrac{1}{f^2\theta_m(\theta_1-\theta_m)}\right)\right) \cdot \\[4mm] \left(\theta_m - \theta_1 e^{-f\left(1-\frac{\theta_m}{\theta_1}\right)} + e^{-f}(\theta_1-\theta_m)\right)\end{array}\right) \qquad \text{(B.4)}$$

where $g = f/\theta_1$.

These equations can be further simplified by expansion and factorization. Here the factor $E$ is defined as: $E = -1 - e^{-f}/f$ :

$$W = rb\left(\frac{1}{3}ch_0\theta_1^2 + h_1\sigma_m + \sigma_m\tan\phi\left(h_3 + h_2\theta_1^2\right)\right) \qquad \text{(B.5)}$$

$$DP = rb\left(ch_0\sin\theta_1 + \sigma_m\tan\phi\left(h_1 + h_4\sin\theta_1\right) - h_3\sigma_m\right) \qquad \text{(B.6)}$$

$$T = r^2b\theta_1\left(ch_0 + \sigma_m\tan\phi\left(\frac{1}{2} + h_4\right)\right) \qquad \text{(B.7)}$$

where:

$$h_0 = 1 + E$$

$$h_1 = \frac{\theta_1}{2} - \frac{\theta_1^3}{20}\left(1 + \frac{i}{2}\right)$$

$$h_2 = \frac{E}{6}\left(1 + \frac{i}{6}\right)^2$$

$$h_3 = \frac{\theta_1^2}{5}\left(1 - \frac{\theta_1^2}{20}\right)\left(1 + \frac{i}{4}\right)$$

$$h_4 = \frac{E}{2}\left(1 - \frac{i}{10}\right)$$

A number of additional parameter groups were defined for ease of understanding of Equation 2.23. These were:

$$h_5 = h_4 + \frac{1}{2}$$

$$h_6 = \frac{T}{r^2 b \theta_1}$$

$$h_7 = \frac{w}{rb}$$

$$h_8 = h_5 h_7 - h_6\left(h_3 + h_2 \theta_1^2\right)$$

$$h_9 = \frac{1}{3}\theta_1^2 h_0 h_5 - h_0\left(h_3 + h_2 \theta_1^2\right)$$

# Appendix C

# Field and Space Robotics Laboratory Experimental Rover System

This appendix contains a description of the Field and Space Robotics Laboratory experimental rover system, which is used to experimentally validate much of the work in this thesis. The FSRL rover was designed and built primarily by Rob Burn and Eric Wilhelm. A more detailed description of the rover can be found in (Burn, 1997; Wilhelm, 1998).

The FRSL experimental rover is a six-wheeled mobile robot with a rocker-bogie suspension similar to the Sojourner rover (Bickler, 1992) (see Figures C.1 and C.2). The six wheels are driven by geared DC motors with a peak torque of 100 oz-in and maximum angular velocity of 12 rpm. The resulting maximum velocity of the rover is approximately 8 cm/sec. The rover is steered with skid-steering. A mechanical differential in the rover frame allows the body to "split the difference" of the two rocker angles. The rover weighs 6.1 kg.

The rover has on-board NiCad batteries to power the six driven wheels and a PC/104 486MHz DX2–66 computer. Additional PC/104 modules support digital and analog IO, and sensor reading. A wireless modem is used for external communication.
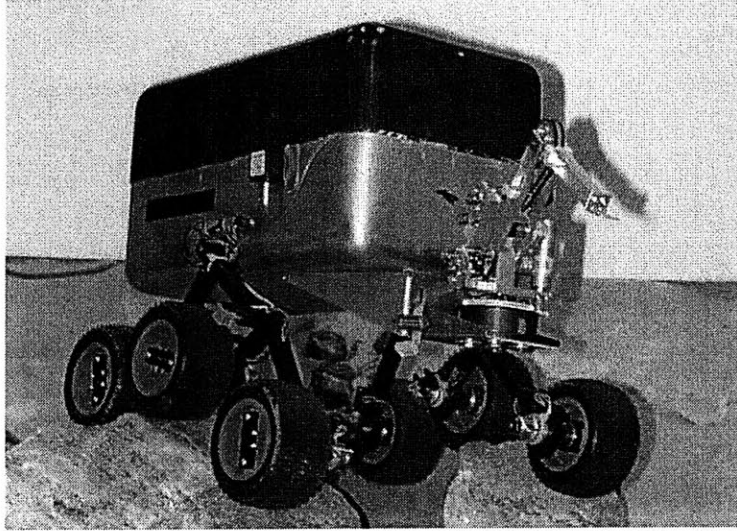
**Figure C.1**: FSRL Experimental rover testbed

The rover sensor suite is composed of tachometers to measure the wheel angular velocities, and a three-axis Crossbow CXL04M3 accelerometer mounted to the rover body to determine roll $\Theta$ and pitch $\Phi$ relative to an inertial frame. A JR3-67M25A six-axis force/torque sensor is mounted at the front of the rover, to measure forces exerted on the rover body by a three d.o.f. manipulator.
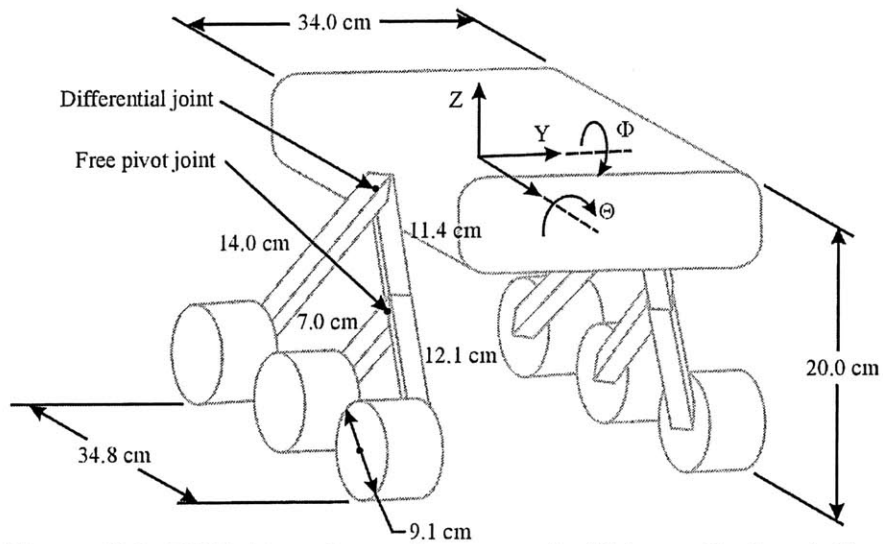


**Figure C.2**: FSRL Experimental rover testbed kinematic description

# Appendix D

# Extended Kalman Filter (EKF) Background

Here, background and equations relating to the extended Kalman filter are presented (Brown, 1997; Welch and Bishop, 1999). Consider a system with the following dynamic equations:

$$\dot{\mathbf{x}} = \mathbf{f}(\mathbf{x}, \mathbf{w}, \mathbf{v}, t) \tag{D.1}$$

where $\mathbf{w}$ and $\mathbf{v}$ represent measurement and process noise vectors. The system measurement vector $\mathbf{z}$ is defined as:

$$\mathbf{z} = \mathbf{h}(\mathbf{x}, \mathbf{v}) \tag{D.2}$$

with measurements acquired at each time step $k$.

A linearized continuous-time state transition matrix can be defined as:

$$\mathbf{F} = \frac{\partial \mathbf{f}}{\partial \mathbf{x}}(\hat{\mathbf{x}}) \tag{D.3}$$

where $\hat{\mathbf{x}}$ is an estimate of the current state.

Computation of the EKF involves the following steps:

1) Initialization of the state estimate $\hat{\mathbf{x}}$ and a covariance matrix, $\mathbf{P}$ with assumed initial values.

2) Propagation of the current state estimate $\hat{\mathbf{x}}$ (from a discrete-time representation of Equation (D.3)) and covariance matrix $\mathbf{P}$ at every time step. The state estimate is computed as:

$$\hat{\mathbf{x}}_{k+1} = \mathbf{f}(\hat{\mathbf{x}}_k, \mathbf{u}_k)$$ (D.4)

The matrix $\mathbf{P}$ is computed as:

$$\mathbf{P}_{k+1} = \mathbf{F}_k \mathbf{P}_k \mathbf{F}_k^T + \mathbf{Q}_k$$ (D.5)

where $\mathbf{Q}$ is the system process noise matrix and is assigned based on the physical model of the system.

3) Updating the state estimate and covariance matrix as:

$$\hat{\mathbf{x}}_k = \hat{\mathbf{x}}_k + \mathbf{K}_k(\mathbf{z}_k - \mathbf{h}(\hat{\mathbf{x}}_k))$$ (D.6)

and
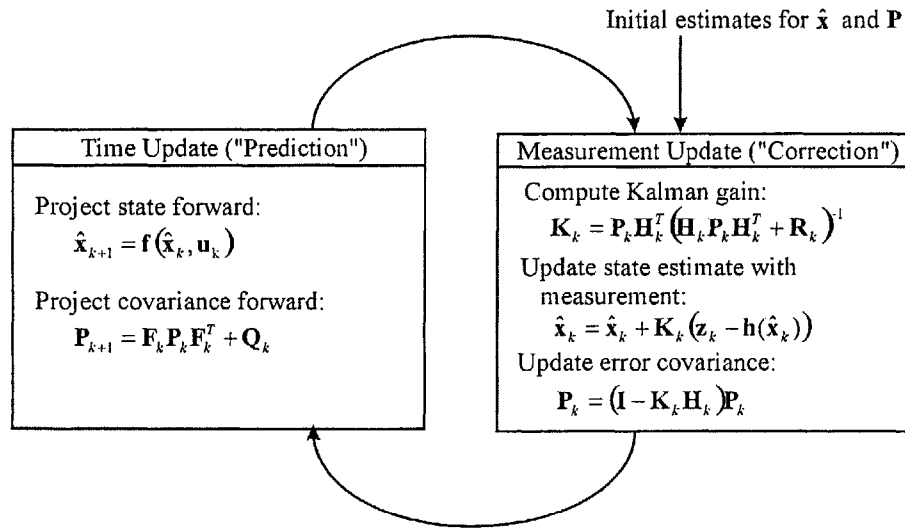
$$\mathbf{P}_k = (\mathbf{I} - \mathbf{K}_k \mathbf{H}_k)\mathbf{P}_k$$ (D.7)

where the Kalman gain matrix $\mathbf{K}$ is given by:

$$\mathbf{K}_k = \mathbf{P}_k \mathbf{H}_k^T (\mathbf{H}_k \mathbf{P}_k \mathbf{H}_k^T + \mathbf{R}_k)^{-1}$$ (D.8)

where $\mathbf{R}$ is the measurement error covariance matrix and $\mathbf{H}$ is a matrix relating the state $\mathbf{x}$ to the measurement $\mathbf{z}$.

See Figure D.1 for a pictorial diagram of the EKF estimation process.



Figure D.1: Diagram of EKF estimation process (from Welch and Bishop, 1999)